DETECTION OF BACTERIAL ENDOSPORES

BY MEANS OF

ULTRAFAST COHERENT RAMAN SPECTROSCOPY

A Dissertation

by

DMITRY SERGEYEVICH PESTOV

Submitted to the Office of Graduate Studies of
Texas A&M University
in partial fulfillment of the requirements for the degree of

DOCTOR OF PHILOSOPHY

May 2008

Major Subject: Physics

DETECTION OF BACTERIAL ENDOSPORES
BY MEANS OF
ULTRAFAST COHERENT RAMAN SPECTROSCOPY

A Dissertation

by

DMITRY SERGEYEVICH PESTOV

Submitted to the Office of Graduate Studies of
Texas A&M University
in partial fulfillment of the requirements for the degree of

DOCTOR OF PHILOSOPHY

Approved by:

Chair of Committee,	Alexei V. Sokolov
Committee Members,	Marlan O. Scully
	Yuri V. Rostovtsev
	Hong Liang
Head of Department,	Edward Fry

May 2008

Major Subject: Physics

ABSTRACT

Detection of Bacterial Endospores by Means of
Ultrafast Coherent Raman Spectroscopy. (May 2008)
Dmitry Sergeyevich Pestov,
B.S., Physics, Nizhniy Novgorod State University;
M.S., Physics, Nizhniy Novgorod State University
Chair of Advisory Committee: Dr. Alexei V. Sokolov

This work is devoted to formulation and development of a laser spectroscopic technique for rapid detection of biohazards, such as Bacillus anthracis spores. Coherent anti-Stokes Raman scattering (CARS) is used as an underlying process for active retrieval of species-specific characteristics of an analyte. Vibrational modes of constituent molecules are Raman-excited by a pair of ultrashort, femtosecond laser pulses, and then probed through inelastic scattering of a third, time-delayed laser field.

We first employ the already known time-resolved CARS technique. We apply it to the spectroscopy of easy-to-handle methanol-water mixtures, and then continue building our expertise on solutions of dipicolinic acid (DPA) and its salts, which happen to be marker molecules for bacterial spores. Various acquisition schemes are evaluated, and the preference is given to multi-channel frequency-resolved detection, when the whole CARS spectrum is recorded as a function of the probe pulse delay. We demonstrate a simple detection algorithm that manages to differentiate DPA solution from common interferents. We investigate experimentally the advantages and disadvantages of near-resonant probing of the excited molecular coherence, and finally observe the indicative backscattered CARS signal from DPA and NaDPA powders. The possibility of selective Raman excitation via pulse shaping of the preparation pulses is also demonstrated.

The analysis of time-resolved CARS experiments on powders and B. subtilis spores, a harmless surrogate for B. anthracis, facilitates the formulation of a new approach, where we take full advantage of the multi-channel frequency-resolved acquisition and spectrally discriminate the Raman-resonant CARS signal from the background due to other instantaneous four-wave mixing (FWM) processes. Using narrowband probing, we decrease the magnitude of the nonresonant FWM, which is further suppressed by the timing of the laser pulses. The devised technique, referred to as hybrid CARS, leads to a single-shot detection of as few as 10^4 bacterial spores, bringing CARS spectroscopy to the forefront of potential candidates for real-time biohazard detection. It also gives promise to many other applications of CARS, hindered so far by the presence of the overwhelming nonresonant FWM background, mentioned above.

DEDICATION

To my wife, daughter, and parents

ACKNOWLEDGEMENTS

There are a lot of people who I have been lucky to get acquainted with and would like to acknowledge for their direct or indirect contribution towards this work.

I am grateful to Drs. Vladimir and Vitaly Kocharovsky who advised me during my early years of graduate school and who assisted in my entering the graduate program in the Physics Department, Texas A&M University.

I am thankful to my committee chair, Dr. Alexei Sokolov, for his guidance, help, and continuous support through the years, as my friend and mentor. I appreciate the wisdom passed on to me by Dr. Marlan O. Scully, who has also been the inspirational leader of the project. His enthusiasm and strong belief in success are largely responsible for the progress we made.

I acknowledge my other committee members, Dr. Yuri Rostovtsev, Dr. Hong Liang, and Dr. Gerhard Paulus, for their support throughout the course of this research and their time spent reviewing the present work. Special thanks to Yuri for his always crystal-clear judgment and cheerful perspective on any problem, no matter how hopeless it seems to be. I admire his attitude! I am grateful to my TAMU co-workers, Miaochan Zhi, Robert Murawski, Xi Wang, Gombojav Ariunbold, Zoe Sariyanni, Nikolai Kalugin, George Welch, and Vladimir Sautenkov, for their valued contribution to the work and useful discussions; to the Princeton group, Arthur Dogariu and Yu Huang, Torsten Siebert from Wuerzburg University and Guy Beadie from NRL for the fruitful collaborations at different stages of the project.

I would like to acknowledge Dr. Hans Schuessler, Alexandre Kolomenki, Sergey Jerebtsov, as well as Dr. Paulus and his students for their help with the laser system and sacrifices they made in the early days; Dr. Jaan Laane’s group for their help with spontaneous Raman and transmission measurements; Dr. Hong Liang’s students for the beautiful spore images acquired at TAMU Microscopy and Imaging Center.

I also want to extend my gratitude to the staff members at the Institute for Quantum Studies and the Physics Department for making my time at Texas A&M University a pleasant experience.

Finally, I thank my parents for their patience, my wife for her encouragement and love, and my daughter for the spare time she is always willing to share with me.

NOMENCLATURE

CARS	coherent anti-Stokes Raman scattering
CSRS	coherent Stokes Raman scattering
FWM	four-wave mixing
NR	nonresonant (two-photon difference frequency is off-resonant with the Raman transition of interest)
FWHM	full-width-at-half-maximum
DPA	dipicolinic acid; chemical formula - $C_5H_3N(COOH)_2$
CaDPA	calcium dipicolinate; chemical formula - $C_5H_3N(COOCa)_2$
NaDPA	sodium dipicolinate; chemical formula - $C_5H_3N(COONa)_2$
PMT	photomultiplier tube
CCD	charge-coupled device
OPA	optical parametric amplifier
FFT	Fast-Fourier Transform

TABLE OF CONTENTS

Page

CHAPTER

CHAPTER Page

LIST OF FIGURES

FIGURE Page

FIGURE Page

FIGURE Page

FIGURE Page

FIGURE Page

LIST OF TABLES

TABLE Page

CHAPTER I
INTRODUCTION

1. Motivation and Research Objective

The anxiety caused by the distribution of anthrax spores through the United States Postal Service in September and October 2001, as well as by multiple false-alarm encounters with suspicious substances later, was further aggravated by the long time required for the identification of Bacillus anthracis spores. The need for detection techniques capable of real-time analysis, local and remote, was apparent. These facts triggered a large-scale search for alternatives to the established laboratory method of growing microorganisms in culture media. The primary objective of this work is to present such an alternative. The approach described here utilizes coherent Raman spectroscopy. The focus is made on the engineering of a robust, selective, and efficient technique for real-time interrogation of complex samples such as powders with the purpose of detection of harmful agents.

2. Background

The development of an efficient and reliable bioagent detection scheme is a work-in-progress, which has been approached from different fields of expertise, such as biology, chemistry, nano-engineering, and laser spectroscopy.

The most prominent biological methods are polymerase chain reaction (PCR) and immunoassays. PCR employs primers to separate organic-specific nucleic acid sequences and polymerases to amplify the segment until it is detectable. Its speed depends on the marker used, but generally the complete analysis can be performed in a few hours. For example, the reported detection limit for PCR based on bacterial pagA gene is ~10^3 spores in 2-3 hours [1]. Immunoassays, which rely on competitive binding

---

This dissertation follows the style of Journals of Optical Society of America.

of bioagents with their antibodies, can detect 10^5 spores in 15 minutes, but their false-positive rate is unacceptably high [2].

A number of other methods are being considered with a focus on the detection of calcium dipicolinate (CaDPA), a marker molecule of bacterial endospores accounting for up to 15% of their dry weight [3, 4]. Relatively fast methods have been developed to chemically extract CaDPA and then detect it by means of fluorescence or photoluminescence. In the later case, the formation of the terbium (Tb^{3+}) dipicolinate complex leads to the enhanced luminescence compared to terbium alone and has been found to detect 10^3 B. subtilis spores (a harmless analog for B. anthracis) per milliliter in 5-7 minutes [5].

Photoluminescence and fluorescence lack specificity. On the other hand, vibrational spectroscopy brings about highly specific chemical information content and is capable of uniquely identifying target analytes. For example, the spontaneous inelastic scattering of photons on molecular vibrations with a gain or loss of vibrational quanta (the process referred to as Raman effect; see Fig. 1.1(a)) provides an excellent fingerprint for species identification. In particular, Raman spectra of bacterial spores are dominated by vibrations of aforementioned CaDPA [6-8]. Even though the detection limit as low as 10^6 spores in 1 second has been reported (13 minutes for good quality spectra, see [9]), the efficacy of conventional spontaneous Raman spectroscopy is hampered by the low efficiency of the Raman scattering process. Two distinct approaches are known to correct this flaw.

Surface-enhanced Raman spectroscopy (SERS), utilizing localized surface plasmon resonance, boosts the efficiency of the Raman scattering process by several orders of magnitude [10]. A device based on SERS was demonstrated to detect 10^4 spores in 5 seconds [11]. SERS was also shown to discriminate between different bacteria [12]. The required contact of the analyte with a substrate seems to be the only limiting disadvantage of this method.

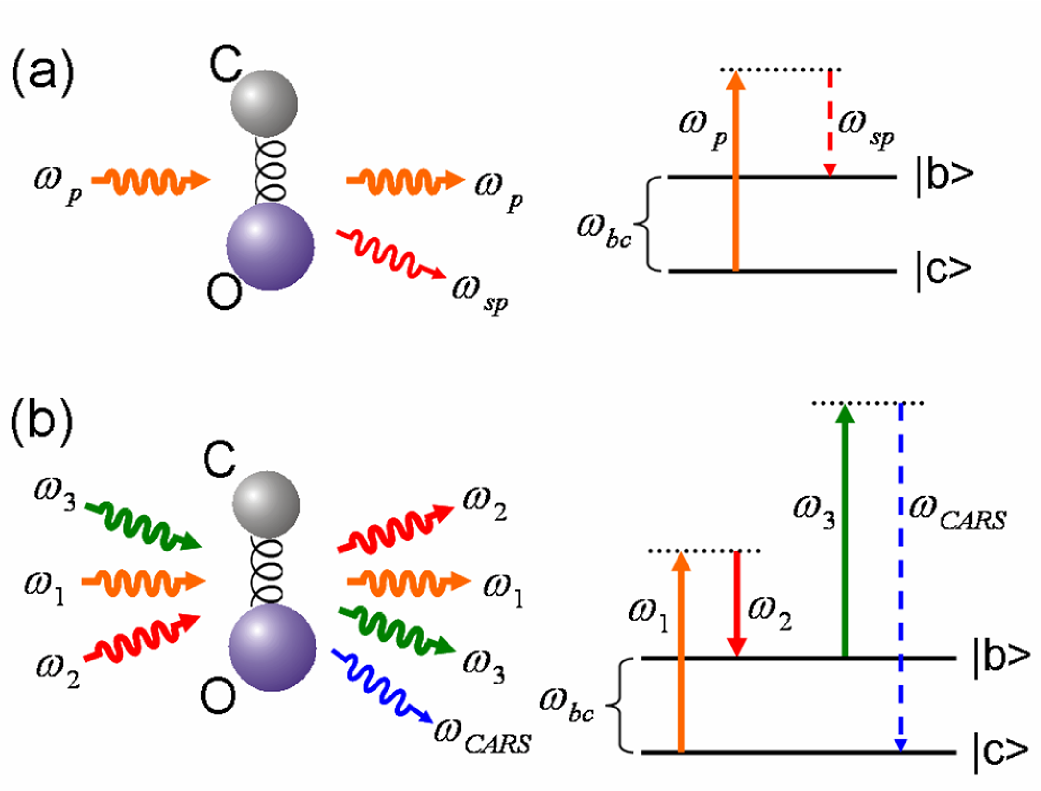

Fig. 1.1. Raman-effect assisted processes: (a) Schematic (left) and level diagram (right) of spontaneous Raman scattering. Light at the probe frequency ω_p passes by a molecule. Some of the light photons inelastically scatter off of the molecule. The shift in the frequency is equal to the characteristic frequency of molecular vibrations. Since most of the molecules are initially in the ground state, the generation of red-shifted photons at frequency $\omega_{sp} = \omega_p - \omega_{bc}$ is dominant; (b) Schematic (left) and level diagram (right) of coherent anti-Stokes Raman scattering. CARS signal is derived from the probe pulse (ω_3) scattering off of the CO molecular vibration, coherently prepared by the pump (ω_1) and Stokes (ω_2) pulses. Here |c> is the ground state of the CO molecule, |b> is the target vibrational state. CO molecule is taken as an example.

The Raman scattering efficiency can also be enhanced by the use of molecular coherence (Fig. 1.1(b)). In coherent anti-Stokes Raman scattering (CARS) spectroscopy [13, 14], employed in this work, the molecules are put into coherent oscillations by a pair of preparation pulses, pump (with the carrier frequency ω_1) and Stokes (ω_2). These macroscopic oscillations of the molecular polarization lead to the efficient scattering of the probe photons (ω_3). The generated beams of blue- and red-shifted photons, whose propagation directions are determined by the phase-matching conditions [15],

$$\vec{k}_{CARS,CSRS} = \vec{k}_3 \pm (\vec{k}_1 - \vec{k}_2), \qquad (1.1)$$

are referred to as CARS and CSRS, respectively (see Fig. 1.2). Phase-assisted buildup of the generated signal over the excitation volume is the key property that differentiates the coherent Raman scattering from spontaneous process. It results in the quadratic dependence of the scattering efficiency on the number of participating molecules. Between the two frequency-shifted components, the preference is usually given to CARS because it is spectrally resolved from the pump and Stokes pulses even for a degenerate scheme ($\omega_3 = \omega_1$). It is also offset from the fluorescence that might be produced by the probe pulse ($\omega_{CARS} > \omega_3 > \omega_{CSRS}$).

The shortcoming that often limits the utilization of CARS is the presence of the nonresonant (NR) four-wave mixing (FWM) signal from other molecules, or even the same molecules, due to the instantaneous electronic response and multiple off-resonant vibrational modes. A few examples of NR FWM schemes are given in Fig. 1.3. Their common feature is that they do not involve and therefore do not depend on the Raman transitions, carrying the signature of intramolecular structure. On the other hand, they take advantage of the same photons and satisfy the same phase-matching relation (1.1).

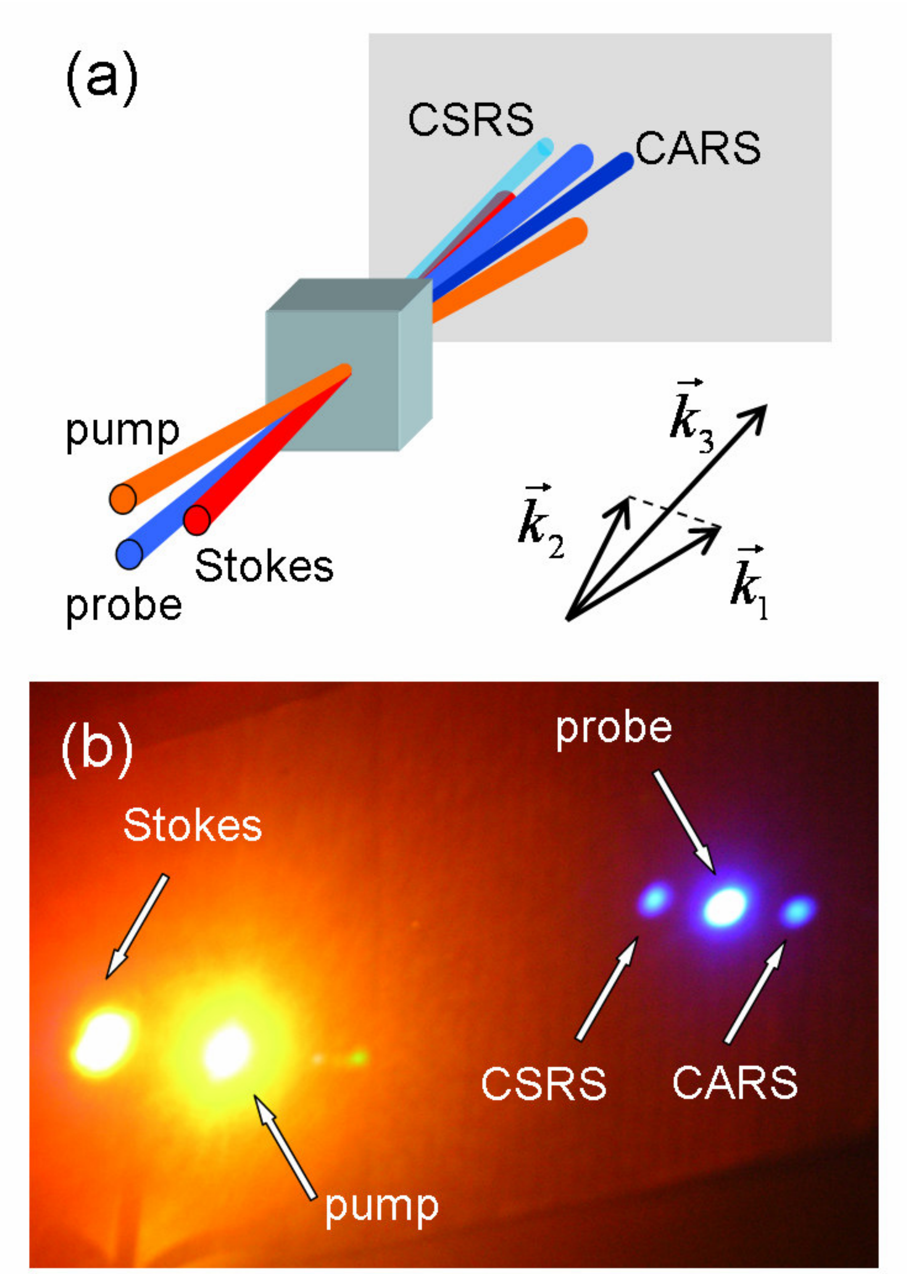

Fig. 1.2. Phase-matching for coherent Raman scattering: (a) BoxCARS geometry for CARS and CSRS generation; (b) an actual screen-shot taken with a cuvette of water as a sample. The pump, Stokes, and probe wavelengths are 585 nm, 640 nm, and 320 nm, respectively.

3. Why Ultrafast? The First Look at the Ultrafast Techniques

A proper choice of the laser pulse configuration is an essential part of this quest for a working detection scheme. Besides the obvious requirements, specificity and speed, the technique of choice for coherent Raman spectroscopy of potential interrogation samples, such as powders, should be able to handle the presence of NR FWM. The established methods, e.g. the polarization-sensitive technique [16], heterodyne [17, 18] and interferometric [19-22] schemes, which rely on preservation of phase and/or polarization, show little promise to accomplish this task because of multiple scattering inside a rough sample. Fortunately, the advert of femtosecond lasers brings about alternative solutions to the problem as well as additional benefits.

First, the short pulse duration (~100 femtoseconds), which is smaller than a typical dephasing time (~ 1 picosecond) of laser-induced molecular vibrations, allows for monitoring of the free-induction-decay dynamics of the excited molecules while effectively suppressing the NR FWM contribution, since the latter process is instantaneous. The second advantage is the large spectral bandwidth of the preparation pulses. This permits access to multiple Raman modes without tuning the laser frequencies. Such multiplicity is essential for specificity of the technique. The larger the

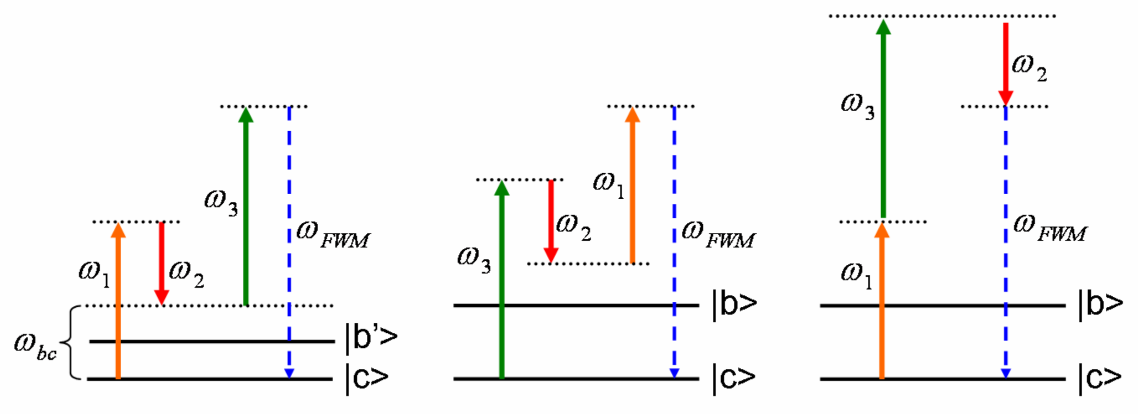

Fig. 1.3. Possible channels of NR FWM generation due to off-resonant vibrational modes and instantaneous electronic response. Here |c> is the ground state of the molecule, |b> is the target vibrational state, |b′> is an off-resonant vibrational state.

Raman frequency span covered, the more information is gained for the analysis from a single measurement. Finally, the spectral amplitude, phase, and timing of the laser pulses can be manipulated for further refinement of the output.

We will consider two ultrafast techniques relying on the use of femtosecond pulses. The first one is known as femtosecond CARS [23, 24]. It is also an indispensable part of Femtosecond Adaptive Spectroscopic Techniques for CARS (FAST CARS), introduced by Scully and co-workers for the very same purpose of bacterial spore detection [25]. The essence of this technique is the coherent excitation of a particular

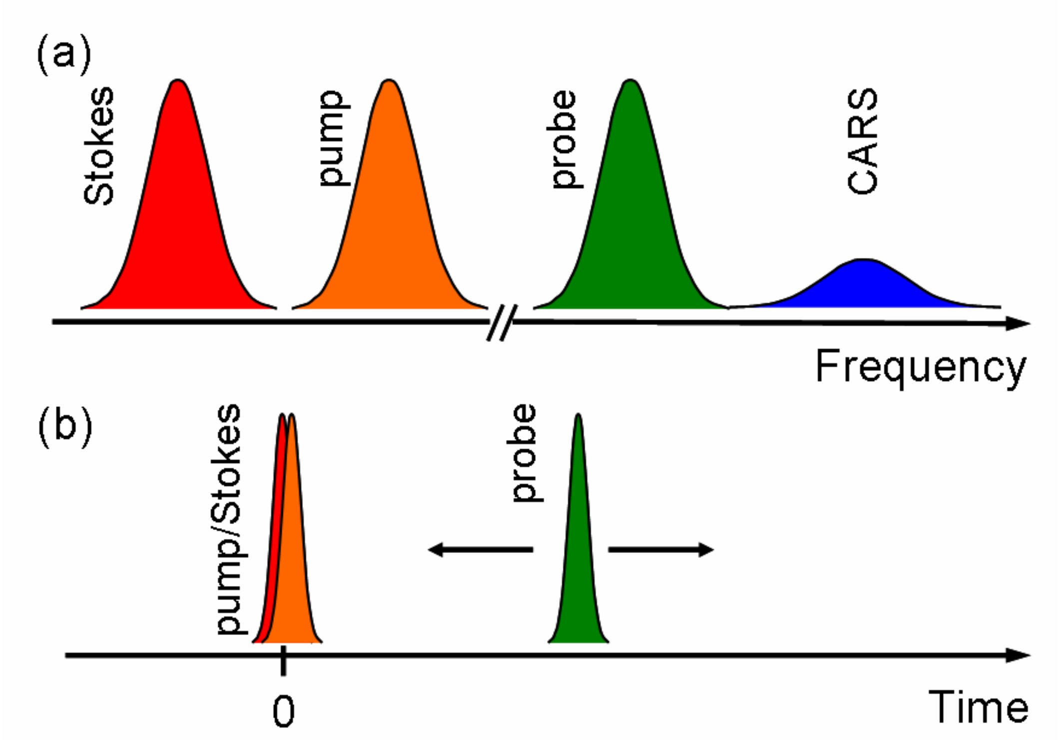

Fig. 1.4. Schematic layout of time-resolved CARS technique in the frequency (a) and time (b) domains. Femtosecond CARS spectroscopy utilizes ultrashort pulses for preparation and probing. The species-specific information is derived from CARS dependence on the probe pulse delay. If only one Raman transition is excited, one would directly measure its decoherence time by delaying the probe pulse. The outcome of the coherent preparation and probing of a few Raman lines within the probe bandwidth is the difference frequency beating between the modes. Delaying the probe pulse eliminates the NR contribution.

Raman transition (or a set of Raman transitions) by a pair of ultrashort laser pulses, pump and Stokes, and its subsequent probing by a third time-delayed ultrashort optical pulse (see Fig. 1.4). For better spectral selectivity, the wavelength of the probe pulse differs from pump and Stokes wavelengths.

While for a fixed probe pulse delay the spectral resolution of the femtosecond CARS scheme is limited by the bandwidth of the probe pulse, one still can gain specificity through the observation of so-called quantum beats [23]. The modulation of CARS signal as a function of the probe pulse delay at the frequency difference between two or more excited Raman modes can be used as a signature. The only requirement for the quantum beat to occur is that the frequency difference between the two excited Raman modes has to be on the order of or smaller than the bandwidth of the probe pulse. The decoherence time can also be used as a discriminating parameter. It is analogous to looking at the bandwidth of the Raman line in frequency-resolved measurements. At last, femtosecond CARS possesses an indispensable property of mitigating the NR FWM when the probe pulse is delayed [25]. As opposed to the slowly decaying Raman-resonant signal, NR contribution decreases as fast as the overlap between the three laser pulses.

The second approach that we have developed and referred to as hybrid CARS [26] is a mixture of the time- and frequency-resolved techniques (see Fig. 1.5; the same approach was introduced by another research group as fs/ps CARS [27]). In this scheme, we again utilize ultrashort transform-limited pulses for uniform broadband Raman excitation but use a tailored narrowband (~ 1 picosecond long) probe pulse, rather than a broadband one. As is illustrated in Chapter VIII, the transition from the time-resolved to hybrid CARS scheme can be obtained through a gradual narrowing of the probe pulse spectral bandwidth. We also use a multi-channel detector to record the anti-Stokes signal at all optical frequencies within the band of interest simultaneously. These modifications allow for spectral discrimination between the narrowband resonant contribution and broadband NR background and extraction of the CARS signal even at zero probe delay. Furthermore, combining the spectrally-resolved acquisition with the time-delayed

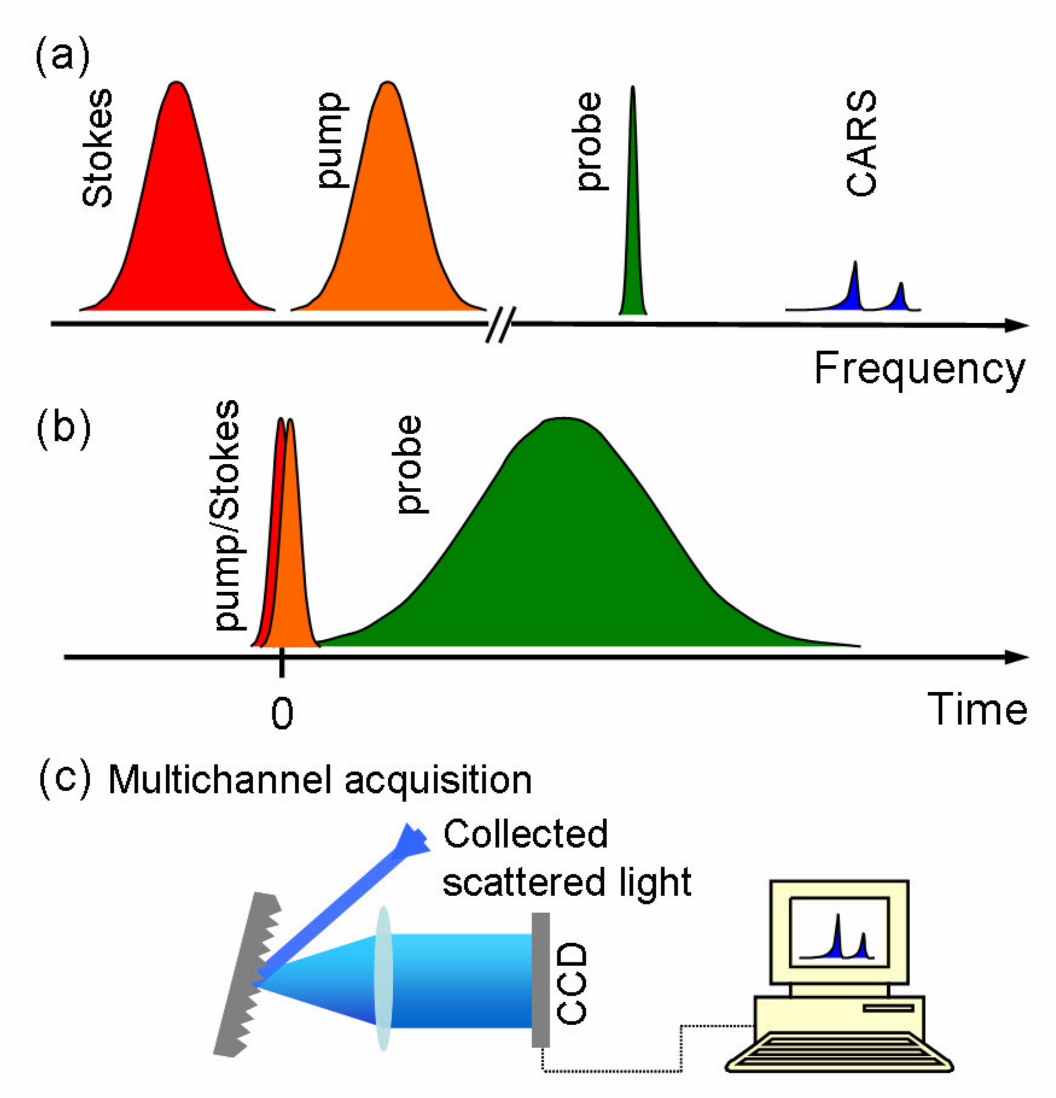

Fig. 1.5. Schematic layout of hybrid CARS technique in the frequency (a) and time (b) domains. Instantaneous coherent broadband excitation of several characteristic molecular vibrations (here we imply the excitation of two Raman modes) and subsequent probing of these vibrations by an optimally-shaped time-delayed narrowband laser pulse help suppress NR FWM and spectrally discriminate the broadband NR background from the vibrationally resonant CARS signal; (c) Multi-channel, spectrally-resolved detection of the generated signal allows for robust, fluctuation-insensitive acquisition of the CARS spectrum.

probing provides the means to suppress the interfering FWM and associated noise, i.e. offers further optimization of the scheme along the lines of time-resolved CARS.

The rest of the dissertation is organized as follows. In Chapter II, the laser system and general layout of the performed CARS experiments are described. We also list there spontaneous Raman spectra of the major samples, such as dipicolinic acid (DPA), sodium dipicolinate (NaDPA), and Bacillus subtilis spores, used in this study.

In Chapter III, time-resolved CARS measurements on methanol-water mixtures are presented. It is shown that relative Raman frequency shifts and coherence relaxation rates can be inferred from the interference between excited Raman modes. The decoherence rates are also found to be sensitive to molecular environment. The chapter is concluded with a proof-of-principle demonstration of CARS on DPA in a sodium-hydroxide-buffered solution.

Chapter IV is devoted to femtosecond CARS measurements on DPA salts and their interferents. Time-resolved CARS profiles are obtained and analyzed for buffered DPA solutions and neat solutions of common chemicals. Different acquisition schemes are considered, and a possible detection algorithm is discussed. Dependences of the acquired signal on the concentration of the target molecule and the wavelength of the UV-probe pulse, near-resonant to the one-photon transition from the ground to the excited electronic state, are investigated. At last, time-resolved CARS on solid powders of DPA and NaDPA is demonstrated. The attempts to use the same scheme for B. subtilis spores are described and evaluated.

In Chapter V, the simplest form of the pulse shaping, linear chirp, is utilized for mode-selective excitation of Raman transitions in the powder of NaDPA. The induced molecular vibrations are still probed by a time-delayed ultrashort pulse. The preparation pulses, however, are stretched in time so that the effective spectral bandwidth of the pump-Stokes excitation is reduced dramatically.

The principles of the devised hybrid technique for coherent Raman spectroscopy are discussed Chapters VI. The emphasis is made on discrimination between the NR FWM and Raman-resonant CARS, as well as suppression of the NR background.

Theoretical consideration and numerical simulations are followed by experimental implementation of the technique, covered in Chapter VII. A set of hybrid CARS measurements on NaDPA powder (as proof-of-principal) and B. subtilis spores is reported. The subsequent optimization of the setup parameters, tailored for spore detection, leads to the acquisition of descriptive single-shot CARS spectra from as few as 10^4 B. subtilis spores in the laser focus.

Finally, in Chapter VIII, a comparative experimental analysis of spontaneous and coherent Raman scattering on a neat solution of pyridine and NaDPA powder is presented. The increase in the Raman scattering efficiency due to the broadband pump-Stokes excitation is derived for both liquid and powder-like samples. The observed enhancement is expected to justify the increased complexity of the setup, as compared to the ordinary Raman measurements.

CHAPTER II

TECHNIQUE IMPLEMENTATION AND MATERIALS

The experimental results described in the following chapters were primarily obtained with two femtosecond laser systems based on Spitfire (Spectra-Physics) and Legend (Coherent). The details of the layout varied from one measurement to another. However, the experimental arrangements do share common features. The purpose of this chapter is to give a general idea of how the CARS measurements are performed.

1. Laser System

We employ a Ti:Sapphire-based regenerative amplifier system (800nm, 1 kHz rep. rate, ~1 mJ/pulse, 40-50 fs) with two evenly pumped optical parametric amplifiers (OPAs). Schematics of the table-top femtosecond laser setup as well as pictures of the installed system from Coherent, taken as a representative example, are shown in Fig. 2.1. The system includes two stand-along pump lasers (Verdi and Evolution), a femtosecond oscillator (Mira), and an amplifier (Legend).

Nd:YVO_4-based Verdi, pumped by a set of fiber-coupled diode lasers at 804 nm, gives out 5 Watt of CW radiation at 532.1 nm, which is a second harmonic of the laser cavity mode. The beam is sent through a water-cooled Ti:Sapphire rod of the oscillator, creating laser gain over a broadband span of wavelengths near 800 nm.

The oscillator operation is based on nonlinear optical Kerr effect, where a high energy light induces local change of index of refraction

$$n = n_0 + n_2 I(t)\,. \tag{2.1}$$

Here n_0 is a normal or linear index of refraction, n_2 is the nonlinear index of refraction (associated with the third-order susceptibility $\chi^{(3)}$), and $I(t)$ is the time-dependent intensity of the pulse envelope. Instantaneous retardation of the index of refraction leads to two important effects, self-phase modulation and self-focusing of the pulse. Self-

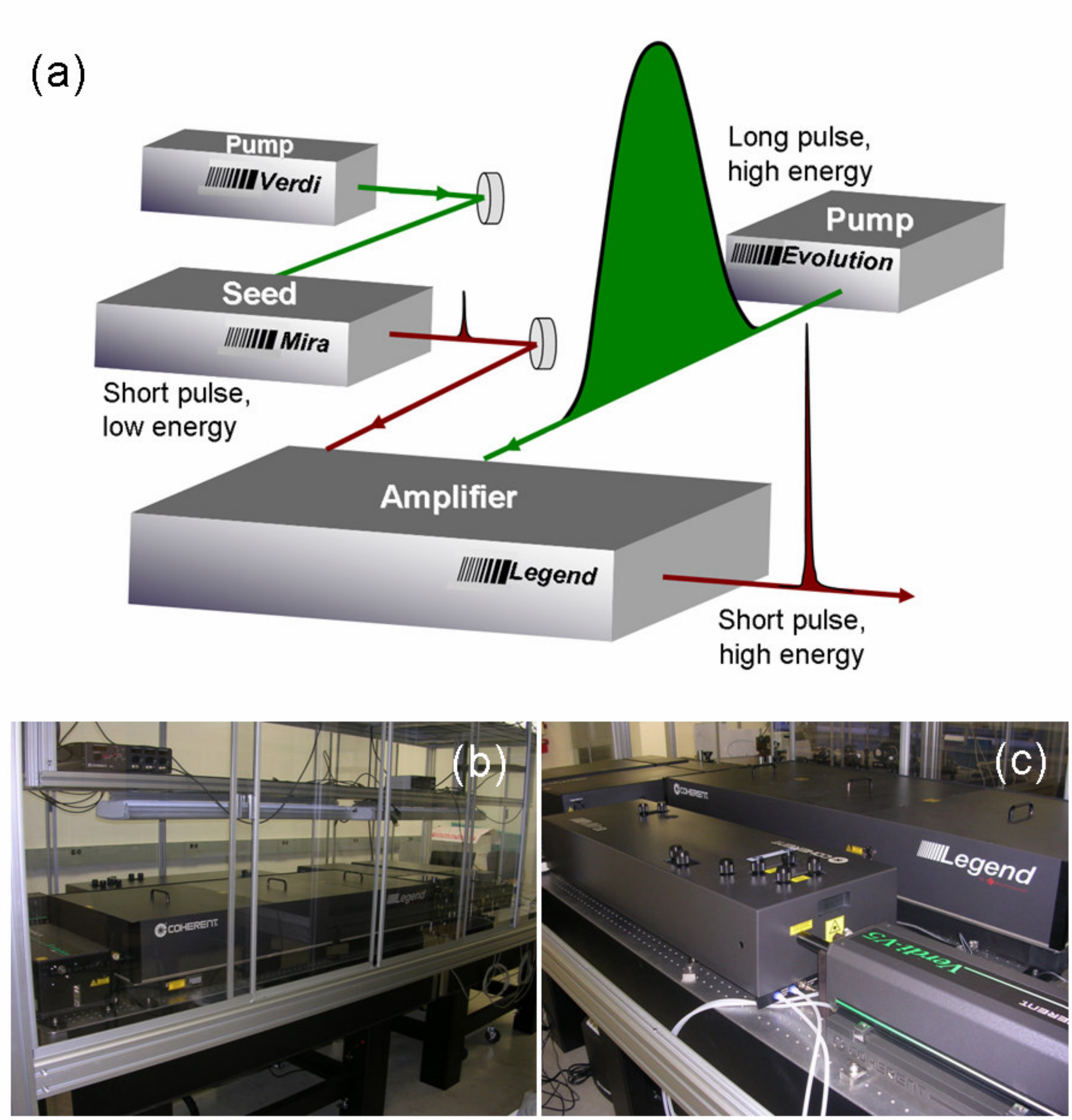

Fig. 2.1. Table-top femtosecond laser system: (a) optical layout of the system based on Legend (Coherent) regenerative amplifier; (b-c) pictures of the system installed.

phase modulation broadens the spectral bandwidth of the pulse and therefore, helps in the formation of the ultrashort pulses. Self-focusing tightens the mode-locked beam waist, while leaving the remaining low intensity CW beam unfocused (wider). Placing a mechanical slit that blocks the wider beam (CW components), the cavity is forced to laze in the mode-locked regime. As a result, Mira provides a stable train of femtosecond pulses with the average power about 0.5 W and rep. rate 76 MHz. The pulses are seeded into the regenerative amplifier.

For ultrashort pulse amplification, extra care has to be taken about the photodamage of active medium because of high peak electric fields. Therefore, the amplifier has three distinct stages. They are a stretcher, a regenerative cavity, and a compressor. The cavity is pumped by a Q-switched Nd:YLF-based laser, operated at 1 kHz rep rate. So, only once in a millisecond a single stretched IR pulse is seeded into the cavity, amplified and then, after about 12 roundtrips, recompressed into a short pulse.

Finally, the output beam of the amplifier is evenly split between two OPAs, OPerA-VIS/UV and OPerA-SFG/UV (see Fig. 2.2(a)). Each OPA incorporates a whitelight-seeded pre-amplifier followed by a power amplifier of Signal and Idler beams. Their frequencies are determined by the conservation of energy and momentum,

$$\omega_f = \omega_{Signal} + \omega_{Idler} \text{ and } k_f = k_{Signal} + k_{Idler}, \tag{2.2}$$

where ω_f and k_f are the frequency and wavevector magnitude of the fundamental (pump) beam. The add-on frequency up-conversion stages of the OPAs, listed in Fig. 2.2(b), provide high flexibility in the choice of wavelengths, ranging from near-infrared (Signal, Idler, or fundamental) to ultraviolet (a fourth-harmonic of Signal or Idler; a second harmonic of the sum-frequency generation).

2. Optical Layout

A generic but comprehensive experimental layout is given in Fig. 2.3. The femtosecond system outputs three linearly polarized laser beams at pre-selected wavelengths that are utilized as pump, Stokes, and probe. In hybrid CARS scheme, the probe pulse is guided through a home-built pulse shaper with an adjustable slit in the Fourier plane of

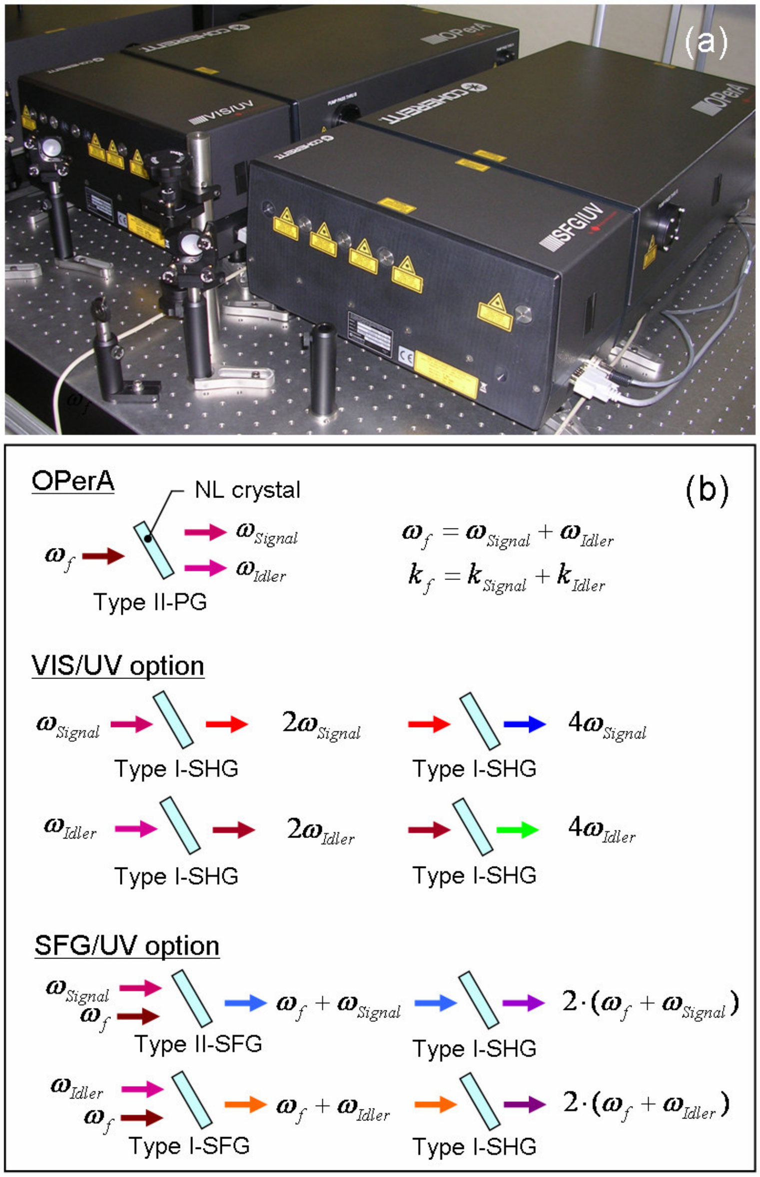

Fig. 2.2. Optical parametric amplifiers: (a) Picture of the installed OPerA-VIS/UV and OPerA-SFG/UV (Coherent); (b) Parametric processes used to produce femtosecond pulses in the infrared-to-ultraviolet range. Abbreviations: PG, parametric generation; SHG, second-harmonic generation; SFG, sum-frequency generation; NL, nonlinear.

spectrally-dispersed beam. Alternatively, the probe pulse is sent directly through a designated delay line, along with one of the preparation pulses, and then all the three beams are focused on the sample. The delay stages are motorized and operated with 1-μm precision through a motion controller (Newport) connected to a PC.

Depending on the experiment, the generated CARS or CSRS signal is collected on the front (backward geometry) or on the back (forward geometry) of the sample and refocused onto the entrance slit of a diffraction-grating spectrometer (Chromex-250is, Bruker Optics or MicroHR, Jobin Yvon) with a thermoelectrically-cooled photomultiplier tube (PMT, Jobin Yvon) or a LN2-cooled charge-coupled device (CCD; Spec-10, Princeton Instruments). The CCD has six decades of dynamic range and images the whole spectral region of interest in a single shot.

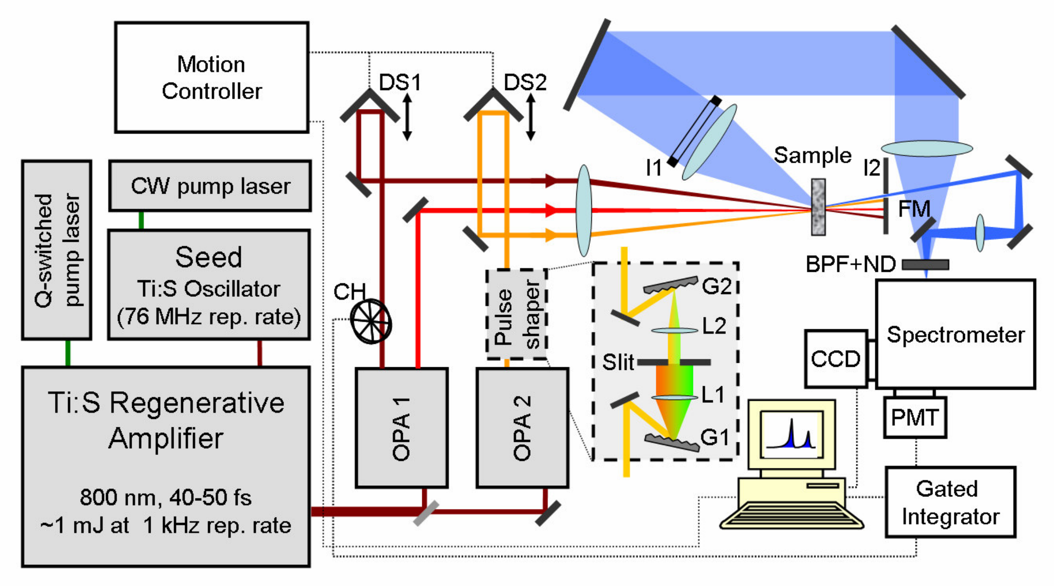

Fig. 2.3. Schematics of the experimental setup. OPA1,2, optical parametric amplifiers; DS1,2, computer-controlled delay stages; I1,2, irises; FM, flip mirror; BPF+ND, bandpass and neutral-density filters; CCD, charge coupled device; PMT, photomultiplier tube; CH, chopper. Inset: home-made pulse shaper. G1,2, ruled gratings (600 grooves/mm, Edmund Optics); L1,2, bi-convex lenses (f=20cm).

When the PMT is used, its response is gated and averaged by a Boxcar Integrator (Stanford Research). We implement active baseline subtraction by chopping one of the preparation beams at half the repetition rate and electronically inverting the sign of every other integrated shot before averaging. This method helps to eliminate the background coming from the spectrally-close probe beam as well as the contribution from high-order nonlinear frequency-mixing of the unchopped beams. The integrated signal is digitized and recorded by the PC. A large dynamic range, which is required in our measurements, is achieved by variable attenuation of the collected light. As we vary the probe pulse delay, we adjust the signal attenuation to avoid PMT saturation.

3. Materials

The fact that calcium dipicolinate (CaDPA) is a marker component of bacterial spores motivates our study of dipicolinic acid (DPA) and its various salts. In particular, most of the experiments are done with an easy-to-make substitute for CaDPA, sodium dipicolinate (NaDPA, see Fig. 2.4). Standard chemicals, such as methanol, ethanol, pyridine, cyclohexane, are used for proof-of-principle and discrimination experiments, where chemical-selectivity of the technique is investigated. In the later case, the chemicals are referred to as interferents.

The spontaneous Raman spectra of NaDPA in a solution and powder form are given in Figs. 2.5 and 2.6. The results of spontaneous Raman measurements on crystalline DPA are summarized in Fig. 2.7. Remarkably, the Raman spectrum of NaDPA in 1300-1700 cm^{-1} domain is well distinct from DPA spectrum and is similar to CaDPA contribution found in spore spectra (see Fig. 2.8). In DPA powder, the set of strong lines at 1395, 1442, and 1572 cm^{-1}, found in NaDPA spectrum, is substituted with a triplet of 1442 (with some structure), 1577, 1644 cm^{-1} lines. The assignment of Raman frequencies to particular vibrational modes of CaDPA and DPA can be found in [6, 28].

The NaDPA solution (with pH=12, to avoid crystallization) is produced by mixing DPA and NaOH in water. To obtain NaDPA powder, a jar with the saturated solution of DPA in H_2O/NaOH is left open for a few days letting water to evaporate. The

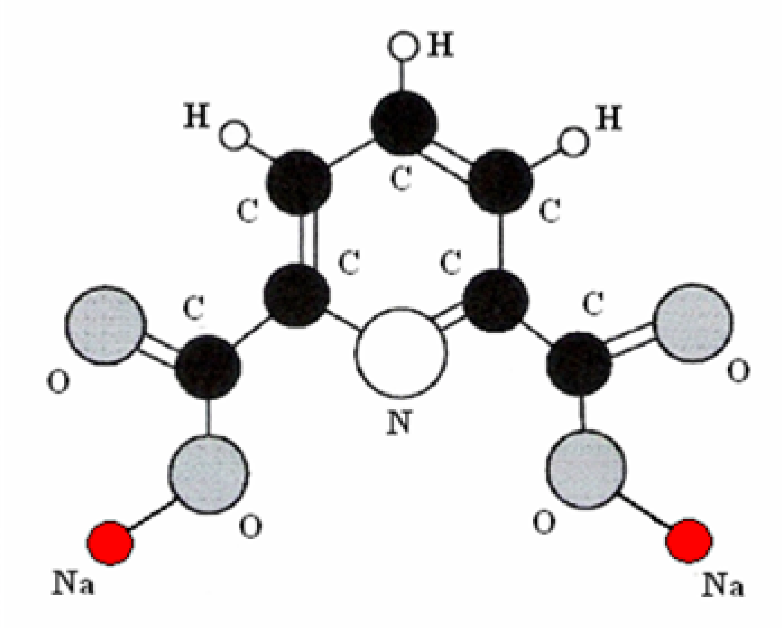

Fig. 2.4. Structure of sodium dipicolinic (NaDPA) molecule. For dipicolinic acid (DPA), sodium atoms are substituted with hydrogen.

needle- and flake-like structures of NaDPA, formed at the walls of the container (similar to those from pure DPA in water; see Fig. 2.9), are then crashed into a fine microcrystalline powder.

Finally, Bacillus subtilis spores, whose images are shown in Fig. 2.10, are used as a harmless surrogate for Bacillus anthracis. Their spontaneous Raman signature can be found in Fig. 2.8.

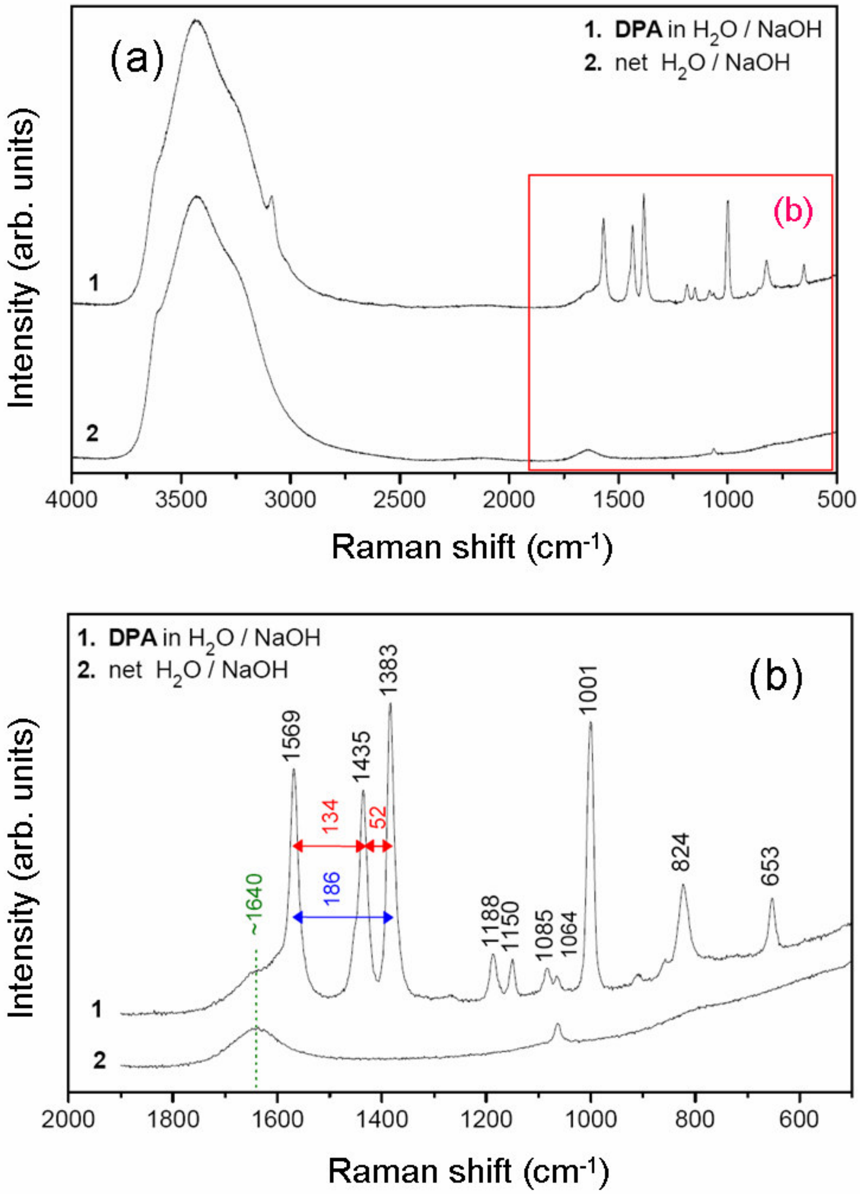

Fig. 2.5. Spontaneous Raman measurements on NaDPA solution: (a) Raman spectrum of 250 mM DPA in H_2O/NaOH at pH=12 (curve 1) and the net solvent (curve 2) acquired with the 180° backscattering geometry of micro-Raman setup using the 514.5 nm line of an Ar+ laser with 40 mW on the sample; (b) The same spectrum in the Raman fingerprint region. The differences in Raman shift for the bands at 1383, 1435 and 1569 cm^{-1} are emphasized with red and blue labels. (courtesy of T. Siebert; see also [45])

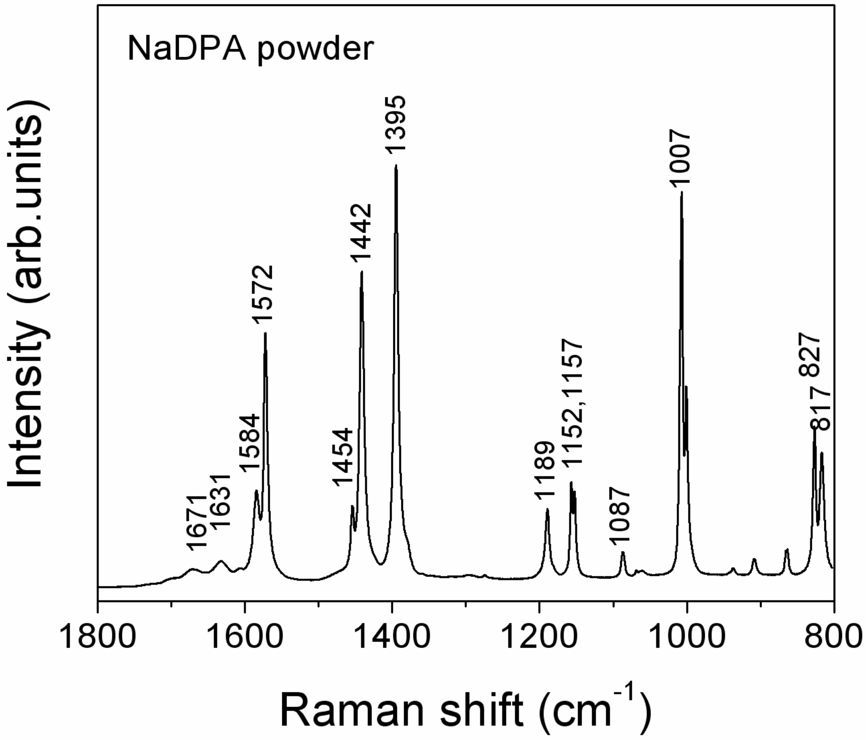

Fig. 2.6. Raman spectrum of NaDPA powder excited by 532-nm light. The signal is acquired with the 90° backscattering geometry.

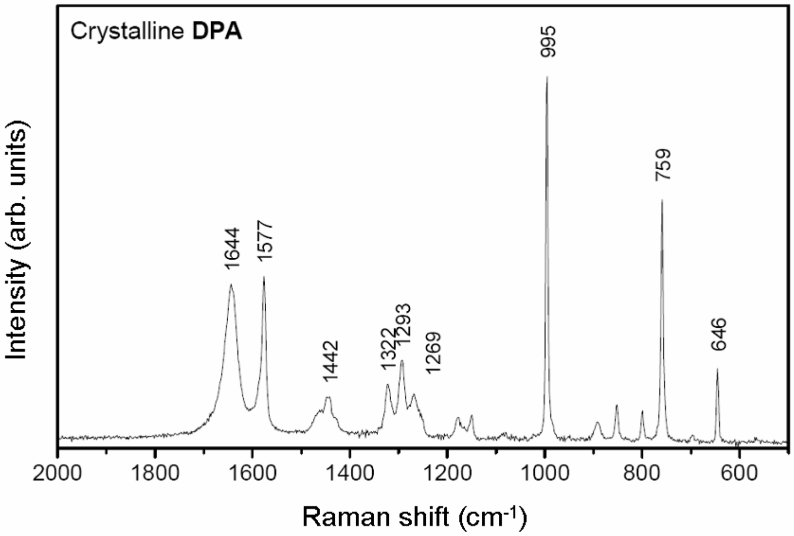

Fig. 2.7. Raman spectrum of crystalline DPA acquired with the 180° backscattering geometry of micro-Raman setup using the 514.5 nm line of an Ar+ laser with 20 mW on the sample. (courtesy of T. Siebert)

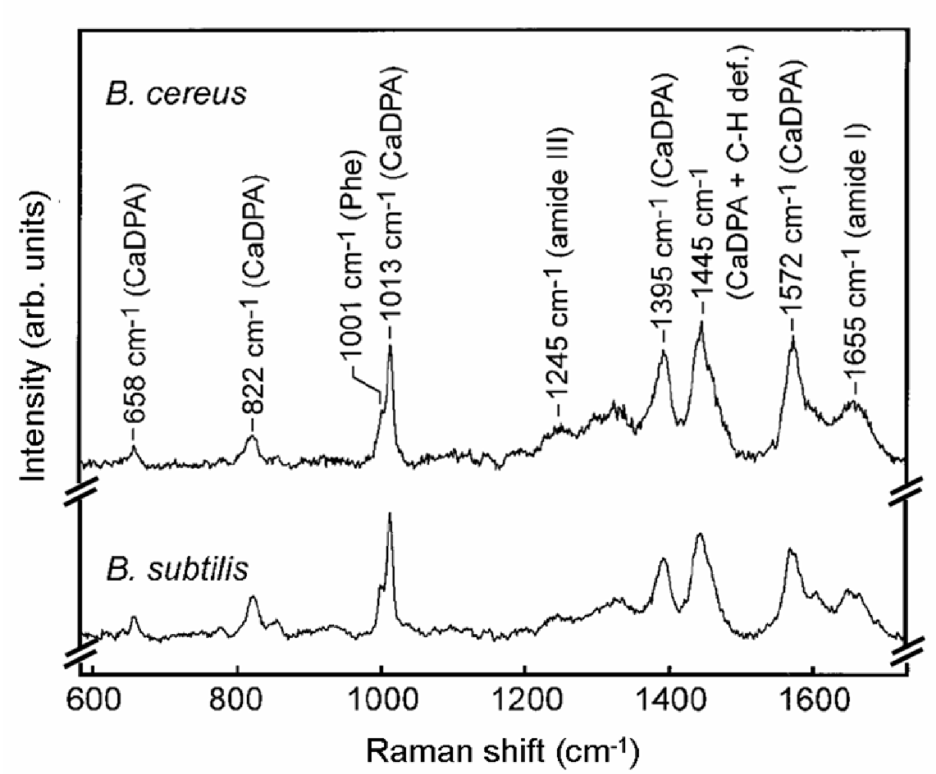

Fig. 2.8. Raman spectra of individual Bacillus spores obtained with 488 nm excitation. The species of each spore is given in the figure. Transitions attributable to CaDPA and protein are observed and identified. Intensity at 1445 cm^{-1} may be due to scattering from both CaDPA and the protein C–H deformation. [7]

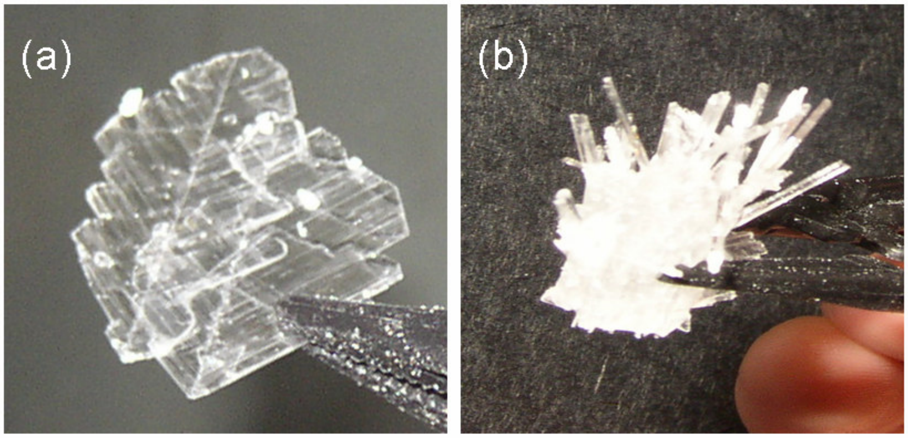

Fig. 2.9. The crystal structures formed after evaporation of water from a saturated solution of DPA in water: (a) flakes, (b) needles.

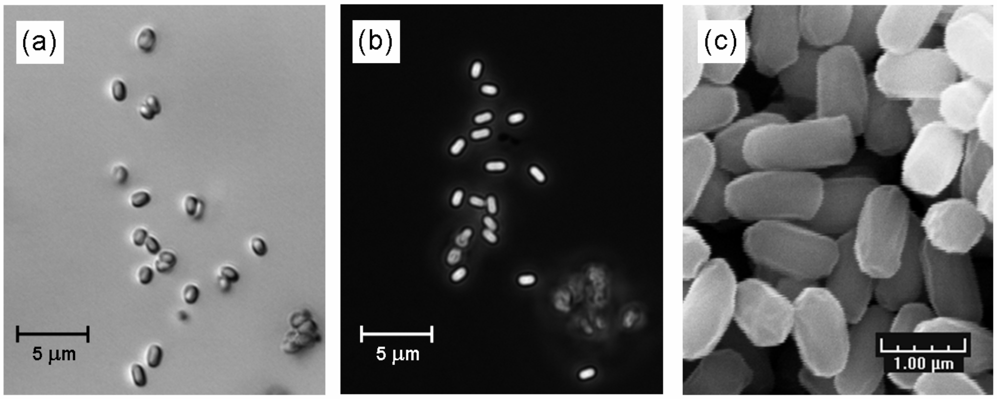

Fig. 2.10. Images of Bacillus subtilis spores obtained via: (a) regular microscopy; (b) phase-contrast microscopy; (c) scanning electron microscopy (using JEOL JSM 6400 SEM). The images are acquired by Xi Wang at the Microscopy and Imaging Center, Texas A&M University.

CHAPTER III

FEMTOSECOND CARS OF METHANOL-WATER MIXTURES[*]

Time-resolved technique is applied to CARS spectroscopy of one of the simplest organic molecules, methyl alcohol. It is demonstrated that relative Raman frequency shifts can be restored from the interference between excited Raman modes. Coherence relaxation rates are shown to be sensitive to molecular environment. The chapter is concluded with a proof-of-principle CARS experiment on DPA in H_2O/NaOH. The C-H stretching mode, common to organic compounds, is employed.

1. Introduction

Methanol (CH_3OH) is one of the simplest organic compounds and yet important because of its use as a solvent. It is well known that methanol and other alcohols, when mixed with water, exhibit anomalous behavior of their viscosity, thermodynamic and transport properties as a function of their concentration in alcohol-water mixtures. One may wonder how it is projected on the molecular dynamics.

In this chapter, time-resolved CARS spectroscopy is utilized for monitoring of vibrational dynamics in methanol-water solutions [29]. Coherence decay rates of 2835 cm^{-1} (symmetric) and 2944 cm^{-1} (asymmetric) C-H stretch modes of methanol [30] are measured for various methanol-water mixtures. We observe qualitatively different, intricate dependences of coherence relaxation for the two lines on the concentration of methanol in its water solution. We speculate that this behavior may be linked to the formation of supramolecular structures, discussed recently in [31].

Note that time-resolved CARS is widely accepted as a powerful spectroscopic tool (for reviews, see [32, 33]). One may find reports on the technique being used to study multiple compounds, such as acetone [34, 35], β-carotene [36], benzene [37],

---

[*] Part of the data reported in this chapter is reprinted with permission from “Femtosecond CARS on methanol-water mixtures” by D. Pestov *et al.*, 2006. *J. Raman Specroscopy*, 37, 392-396. Copyright 2006 by John Wiley & Sons, Ltd.

iodine [24], hydrogen [38]. Previous CARS experiments on methanol were performed with sub-picosecond resolution [39].

2. Methanol-water Mixtures: Experimental Results

The femtosecond system based on Spectra-Physics Spitfire was used for these measurements. Briefly, the output beam of the amplifier (~810 nm, 1 kHz rep. rate, 0.9 mJ/pulse) was split into three parts. Two of them, accounting for 96% of the total optical power, pumped OPAs (Spectra-Physics OPA-800C), producing linearly-polarized pulses with central wavelengths of 660 nm (pump) and 575 nm (probe). The third part of the amplifier beam (Stokes) was sent directly at the sample, a 10-mm path quartz cell filled with methanol or methanol-water mixture. The average powers of the laser beams on the sample were 0.13 mW, 0.39 mW, and 0.18 mW for the pump, Stokes, and probe, respectively. The spatially filtered CARS beam was attenuated and refocused on the entrance slit of a diffraction-grating monochromator, which had a TE-cooled PMT attached to the exit slit. The wavelength selected by the monochromator was set to be 495 nm, an expected wavelength for CARS. The response from the PMT was gated and averaged by a boxcar integrator (Stanford Research Systems).

Figure 3.1 shows the time dependence of the CARS signal on the delays of the Stokes and probe pulses with respect to the pump pulse. The first bright spot at zero time delay, when all three pulses are overlapped in space and time, is attributed mainly to NR FWM. The beating tail to the right, along the positive probe pulse delay, is the signature of the CARS signal coming from the scattering of the probe pulse off the excited molecular vibrations.

The quantum beat can be fit with a function of the form

$$I_{CARS} \sim \left|A\exp(-t/T_2') + B\exp(i\Delta\omega t - t/T_2'' + i\varphi)\right|^2, \qquad (3.1)$$

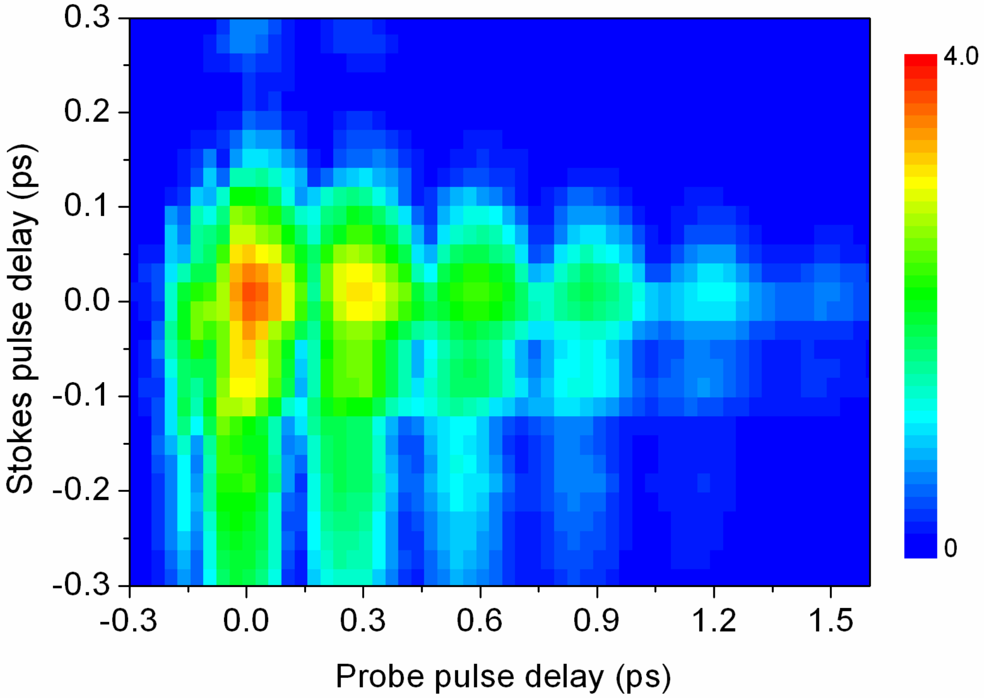

Fig. 3.1. Time-resolved CARS on pure methanol: dependence of the signal on the Stokes and probe pulse delay with respect to the pump pulse. [29]

where $\Delta\omega$ is the difference frequency between the two Raman transitions, T_2' and T_2'' are the coherence relaxation times, φ is the phase shift between the oscillations at $t = 0$, and A and B are the constants defined by the strengths of the transitions and other parameters of the experiment.

For the case of pure methanol, the fit gives the beat frequency of 111 ± 2 cm^{-1}, which is in good agreement with absolute Raman shifts from [30], having the difference 109 cm^{-1}. The values of the coherence relaxation times, T_2' and T_2'', were found to be 589 ± 3 fs and 389 ± 23 fs. Our results are comparable to those reported in [39], 200 ± 200 fs. They are also consistent with the estimates of the Raman line widths from methanol spontaneous Raman spectrum in [40], 600 and 400 fs.

Finally, we perform the same measurements for a set of different concentrations of the methanol-water mixture. Figure 3.2 shows the CARS signal as a function of the probe pulse delay for methanol volume fractions of 25% and 50%, in addition to pure methanol. It is apparent that the transformation of this dependence from the top curve (100% concentration) to the bottom curve (25% concentration) is not monotonic. In order to quantify this nontrivial behavior, we extract the molecular constants from fits to the experimental data for several methanol-water mixtures.

The retrieved values are summarized in Table 3.1. The decoherence times are also plotted in Fig. 3.3. While there is no detectable shift in the beat frequency, $\Delta\omega$, the relaxation rates exhibit anomalous behavior. One of them peaks for the methanol-water ratio 55:45, giving T_2'' equal to 460 fs. The other changes monotonously. Interestingly, the decoherence rates merge in the limit of low methanol fractions.

3. Methanol-water Mixtures: Interpretation and Summary

Recent studies on methanol-water solution at various mole-fractions have revealed interesting phenomenon. Namely, Dougan *et al.* [31] showed that mixtures of methanol and water form extended structures despite the components being fully miscible in all proportions. In particular, in the methanol mole fraction region between 0.27 and 0.54 (which correspond to 45% and 73% fractions by volume), both methanol and water appear to form separate percolating networks. Authors of [31] reported that methanol and water form clusters of methanol-rich and water-rich regions. The characteristic time scale of forming and breaking is on the order of 1-3 ps. According to [31], the extended structures in the methanol-water system are very dynamic, with rapid shedding and reforming of cluster members.

The formation of such clusters can lead to the interesting dependence of Raman line broadening on methanol-to-water ratio. A simple explanation of the observed relaxation rate behavior is the following. The relaxation of vibrational coherence occurs due to collisions with surrounding molecules. The formation of complex supramolecular structures can actually speed up relaxation because the bigger structure experiences a larger number of collisions. The increase of the relaxation rate depends on the coupling between the methanol vibrational modes in the complex. If the coupling is strong, the relaxation rate is enhanced. Otherwise, it does not change significantly. Thus we can see that the decrease of relaxation time (increase of relaxation rate) for the molecular vibrations can be explained as a manifestation of the formation of clusters. One would expect that the symmetric and asymmetric modes would be affected by such a mechanism differently.

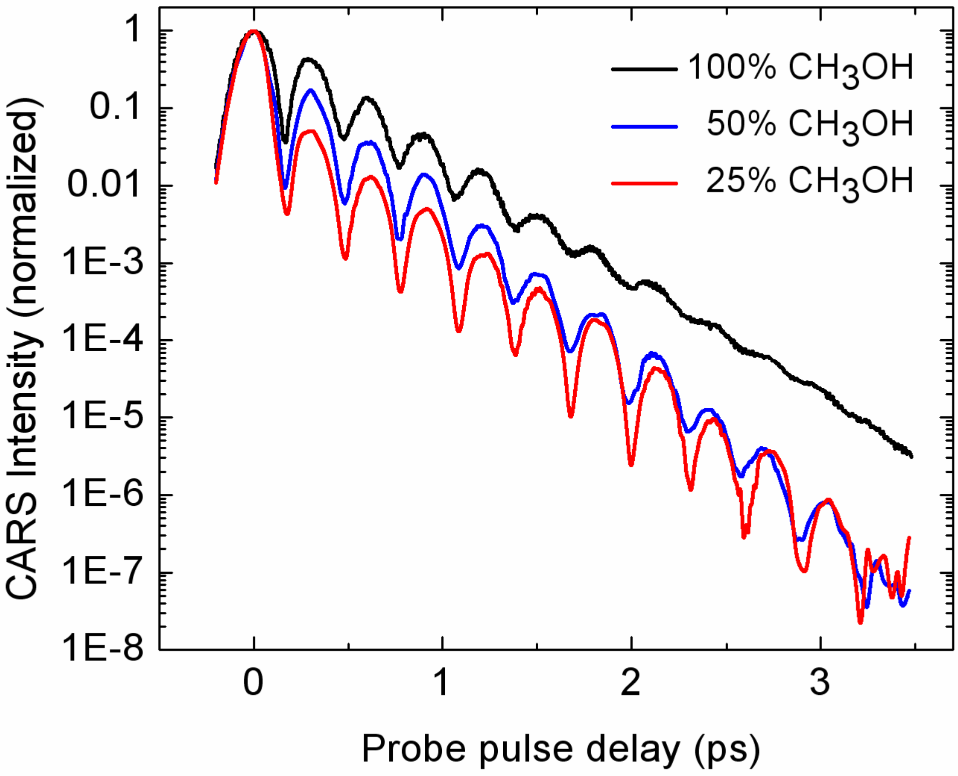

Fig. 3.2. Dependence of CARS signal on the probe pulse delay for different fractions of methanol in water (100, 50, and 25% by volume). [29]

Table 3.1. Difference frequency, $\Delta\omega$, and coherence relaxation constants, T_2' and T_2'', obtained from fitting the experimental date with the function in Eq. (3.1). [29]

%	**100**	**75**	**50**	**33**	**25**
$\Delta\nu = \Delta\omega / 2\pi c\,(\mathrm{cm}^{-1})$	111±2	111±2	111±1	110±2	109±2
T_2' (fs)	589±3	495±12	457±10	513±13	510±13
T_2'' (fs)	389±23	408±17	418±26	498±12	510±13

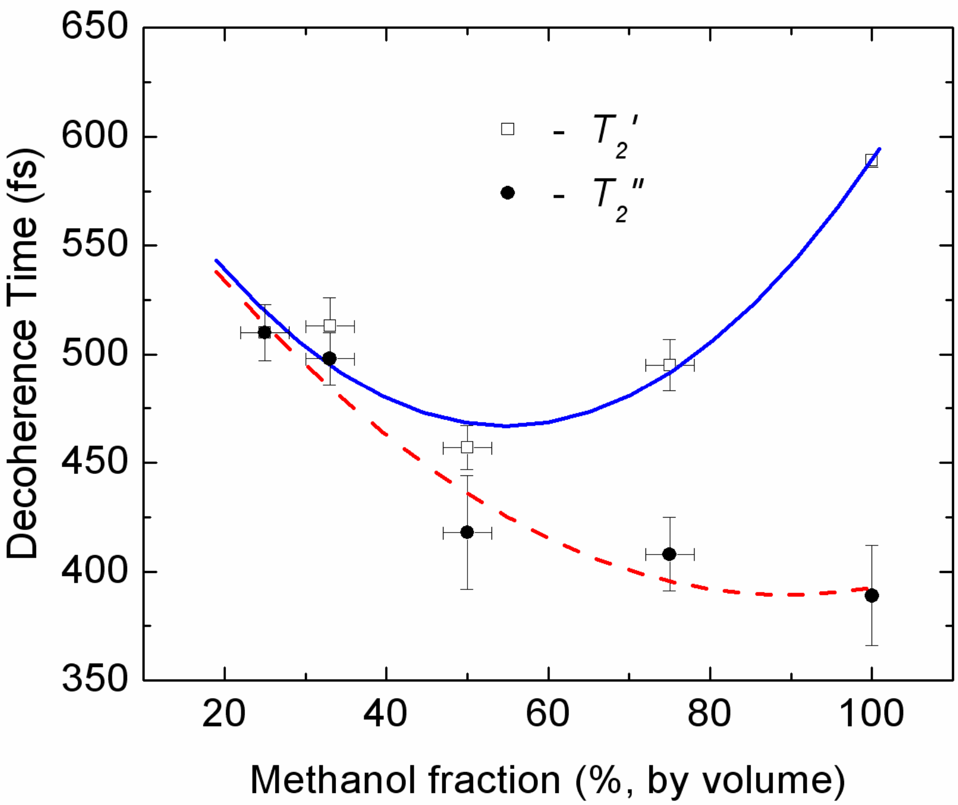

Fig. 3.3. Dependence of the coherence relaxation constants, T_2' and T_2'', on methanol fraction in methanol-water mixtures. The tabulated values are fitted with a quadratic polynomial. [29]

To summarize, the coherence relaxation constants for symmetric and asymmetric C-H stretch modes in methanol-water solutions exhibit a nontrivial dependence on methanol concentration. This intriguing behavior may have its roots in the formation of extended supramolecular structures. We speculate that these extended structures affect the intermolecular interactions between the methanol and water molecules and modify vibrational decoherence rates.

4. Proof-of-principle Measurements on C-H Stretching Mode of NaDPA in Solution

It is not surprising that C-H stretching modes at wavenumbers near 3000 cm^{-1} are commonly found in Raman spectra of organic molecules. The number of these vibrational modes and the exact values for their frequencies slightly depend upon the structure of the molecules but because of their high congestion, the modes are not usually referred to as molecular fingerprints. The preference is given to lower-frequency vibrations of characteristic multi-atomic subgroups.

Nevertheless, spontaneous Raman spectrum of DPA in H_2O/NaOH (see Fig. 2.5) exhibits a fairly strong line at 3083 cm^{-1}. With the same experimental setup, we acquired CARS traces for NaDPA solution (DPA concentration was not carefully measured but is estimated to be close to 100 mM) and pure H_2O/NaOH. The recorded time-resolved profiles, shown in Fig. 3.4, have a clear indication of a Raman line excited in NaDPA solution but not in the solvent. Its exponential decay rate is $\gamma \equiv 2/T_2 \approx 5.2$ ps^{-1}, which corresponds to the coherence relaxation time $T_2 = 0.38$ ps.

Although the obtained signature is not very selective (dephasing time T_2 is the only parameter that can be used for discrimination), the result demonstrates the feasibly of time-resolved CARS spectroscopy on complex molecules, such as DPA. Another important effect in favor of the time-resolved technique is the mitigation of the broadband contribution from the solvent, present in the spontaneous Raman spectrum.

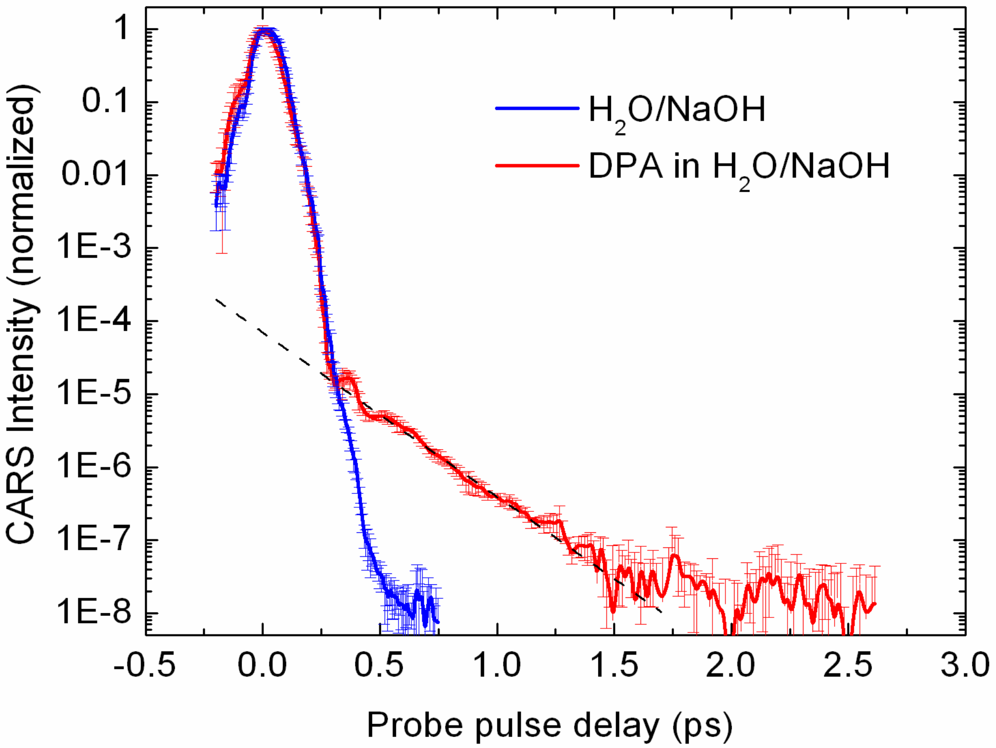

Fig. 3.4. Time-resolved CARS on NaDPA solution. The C-H stretching mode of DPA in H_2O/NaOH (~3083 cm^{-1}) is excited by the overlapped pump (650 nm) and Stokes (810 nm) pulses. Dependence of the collected CARS signal on the probe pulse (585 nm) delay is recorded for the solution and pure solvent.

CHAPTER IV
FEMTOSECOND CARS ON DPA SALTS AND INTERFERENTS[*]

Time-resolved technique is applied to CARS/CSRS spectroscopy of DPA salts, as a marker for bacterial spores, as well as some interferents. Different acquisition schemes are demonstrated, and possible detection algorithm is discussed. Dependences of the acquired signal on the concentration of the target molecule and the wavelength of the UV-probe are investigated. At last, time-resolved CARS on solid powders of DPA and NaDPA is demonstrated.

1. Introduction

CARS or CSRS signal measured as a function of the probe pulse delay is an excellent tool for monitoring vibration relaxation dynamics. If a single vibrational mode is excited, the signal exhibits an exponential decay. However, if more than one mode is excited and contributes into the signal, the recorded trace bears the signature of the beating between these modes. By taking its Fourier transform, one can obtain the beat frequency spectrum and in principal, use it for species detection. Another attractive property of the time-resolved scheme is the above mentioned suppression of NR background by the timing of the probe pulse with respect to the temporally overlapped pump and Stokes fields. Due to its instantaneous nature, the NR FWM processes cease when the probe delay is larger than the pulse width.

In this chapter, we report on measurements of the beat frequencies from the vibrational modes of DPA, and a series of other molecules [41]. We show that the spectral information obtained can be used for molecule identification. Explicitly, the normalized spectral component at the molecule's characteristic beat frequency is a good

---

[*] Part of the data reported in this chapter is reprinted with permission from "Discrimination of dipicolinic acid and its interferents by femtosecond coherent Raman spectroscopy" by Y. Huang *et al.*, 2006. *J. Appl. Physics*, 100, 124912. Copyright 2006 by American Institute of Physics; from "Concentration dependence of femtosecond coherent anti-Stokes Raman scattering in the presence of strong absorption" by M. Zhi *et al.*, 2007. *J. Opt. Soc. Am. B*, 24, 1181-1186. Copyright 2007 by Optical Society of America.

indicator for differentiation of the molecule from its interferents. The entire spectrum of the generated signal, imaged in spectrograms, provides even more comprehensive information and explains the variety of qualitatively different traces that can be obtained for the same molecule. At last, we use the time-resolved technique to study the dependence of coherent Raman scattering intensity on the concentration of target molecules in a solvent [42] as well as on the wavelength of UV-probe laser pulse, near-resonant to the excited electronic state of NaDPA molecule.

2. DPA Salts and Interferents

A. Experimental Layouts and Acquisition Schemes

We utilize two laser systems (with different pulse wavelengths, spectral widths) and three different signal acquisition methods. Their principal schematics are given in Fig. 4.1. In the first set of experiments, a regeneratively amplified Ti:Sapphire laser system (Spectra-Physics, Spitfire) provides pulses at 808 nm with a duration of 100 fs, a repetition rate of 1 kHz, and a single-pulse energy of about 0.8 mJ. As shown in Fig. 4.1(a), the amplified pulses are split into three beams, which are used to pump an optical parametric amplifier (OPA, 0.55 mJ), a second harmonic generator (SHG, 0.10 mJ), and a noncollinear OPA (NOPA, 0.15 mJ). The wavelengths of the pump, Stokes, and probe pulses are 382, 404, and 660 nm and their single-pulse energies at the sample are 0.8, 1.0, and 1.3 μJ, respectively. The 382 and 404 nm pulses excite the vibrational modes near 1400 cm^{-1}, where two strong Raman modes of DPA in a potassium-hydroxide-buffered water solution (H_2O/KOH), 1395 and 1446 cm^{-1}, give a characteristic coherence beat signal at a frequency of 51 cm^{-1}. These two modes have been previously identified as *A*1 symmetric O–C–O stretch and the *A*1(*R*5) ring mode [8]. The spectral widths of the pulses are about 150 cm^{-1}, which are broad enough to excite both modes. The pump and Stokes pulses overlap temporally, and the probe pulse delay is controlled by a motorized delay stage. The three beams are collimated and focused by a lens with a focal length of 20 cm to a beam size of 100 μm, and spatially overlapped onto the sample using a folded-BoxCARS geometry to optimize the phase matching condition

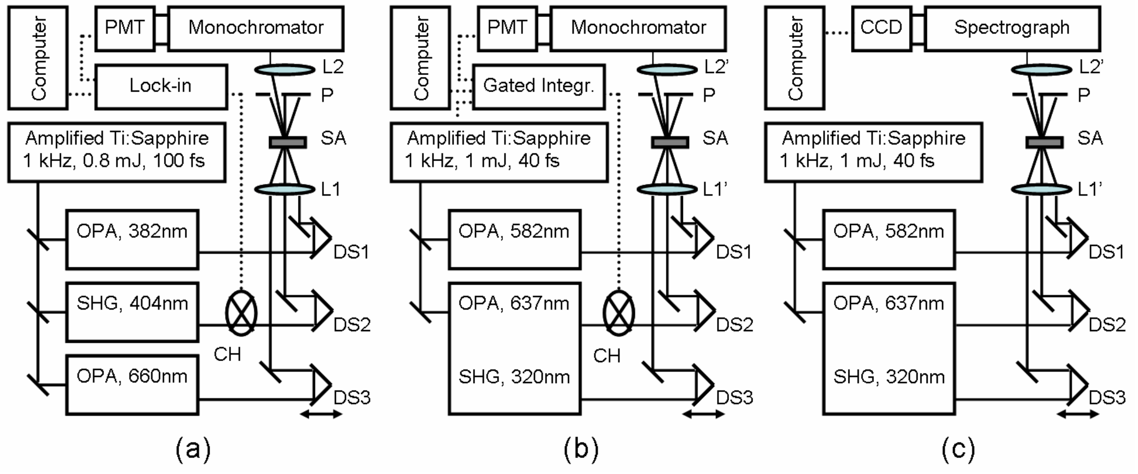

Fig. 4.1. Experimental setup layouts: (a) Time-resolved CARS experiment. A combination of PMT and Lock-in is used for single-channel acquisition; (b) Time-resolved CSRS experiment. The signal acquisition is done by a combination of PMT and Gated Integrator; (c) Time-resolved CSRS experiment. Multi-channel acquisition by means of CCD is employed. CSRS spectrograms are recorded. PMT: photomultiplier tube; CCD: charge-coupled device; NOPA: noncollinear OPA; OPA: optical parametric amplifier; SHG: second-harmonic generator; CH: chopper; DS1-3: delay stages; L1,2,1′, 2′: lenses; SA: sample; P: pinhole.

[43]. The generated CARS signal at 603 nm is spatially selected with a pinhole and focused onto a monochromator, which spectrally separates CARS from any scattered input beams. The signal detected by a photomultiplier tube (PMT) is measured using a lock-in amplifier and an optical chopper placed in the Stokes beam. This phase-sensitive detection scheme provides a dynamic range of five decades. DPA in H_2O/KOH with a concentration of 300 mM is used. All the interferents are pure liquid solutions. The solutions are placed in a quartz cuvette with a path length of 1 mm. Given the focusing geometry, we estimate an interaction length of about 500 μm.

In the second experiment (see Fig. 4.1(b)), a regeneratively amplified Ti:Sapphire laser system (Coherent, Legend, 1 mJ, 1 kHz repetion rate), with 40 fs pulses on the output, pumps two OPAs (Coherent, OperA), which provide laser beams at 582, 638, and 319 nm. The 582 and 638 nm pulses are the pump and Stokes pulses, respectively. They excite the same vibrational modes near 1400 cm^{-1} but their spectral widths are about two times larger than the first experiment. The 319 nm laser pulse is used as a probe. Again, all three beams are arranged in a folded BoxCARS geometry and focused with 40–50 cm focal length lenses on a quartz cuvette filled with a solution sample. The cuvette has a 2 mm optical path length. In this experiment, we choose CSRS (at 335 nm) rather than CARS (at 305 nm) to avoid the strong UV absorption by DPA in a sodium-hydroxide-buffered water solution (H_2O/NaOH). The generated CSRS signal is spatially selected with a pinhole and focused onto the entrance slit of a monochromator (Jobin Yvon, MicroHR). The photons are detected with a PMT (Jobin Yvon), and the signal is retrieved by a Gated Integrator (Stanford Research). The active baseline subtraction scheme, described in Chapter II, is implemented.

Finally, in the third experiment (see Fig. 4.1(c)) multi-channel acquisition of the scattered radiation via a charge-coupled device (CCD; Princeton Instruments, LN2-cooled Spec-10) attached to a spectrograph (Jobin Yvon, MicroHR; CCD output port) is used. The whole CSRS spectrum is recorded as a function of the probe delay. Such CSRS spectrograms are obtained for DPA in H_2O/NaOH (230 mM solution) as well as several representative interferents.

B. Results and Discussion

In the first experiment we record the time-resolved CARS traces on 15 different molecules. Figs. 4.2(a-c) show representative measurement results of DPA in H_2O/KOH, nitromethane, and cyclohexane, respectively. All of them exhibit strong temporal modulations, indicating the excitations of two or more vibrational modes near 1400 cm^{-1} within the line width of the laser pulses. The signal from DPA molecules in KOH-buffered solution exhibits a modulation period of 650 fs, corresponding to a vibrational level spacing of 51 cm^{-1}, which matches very well with our Raman measurements and

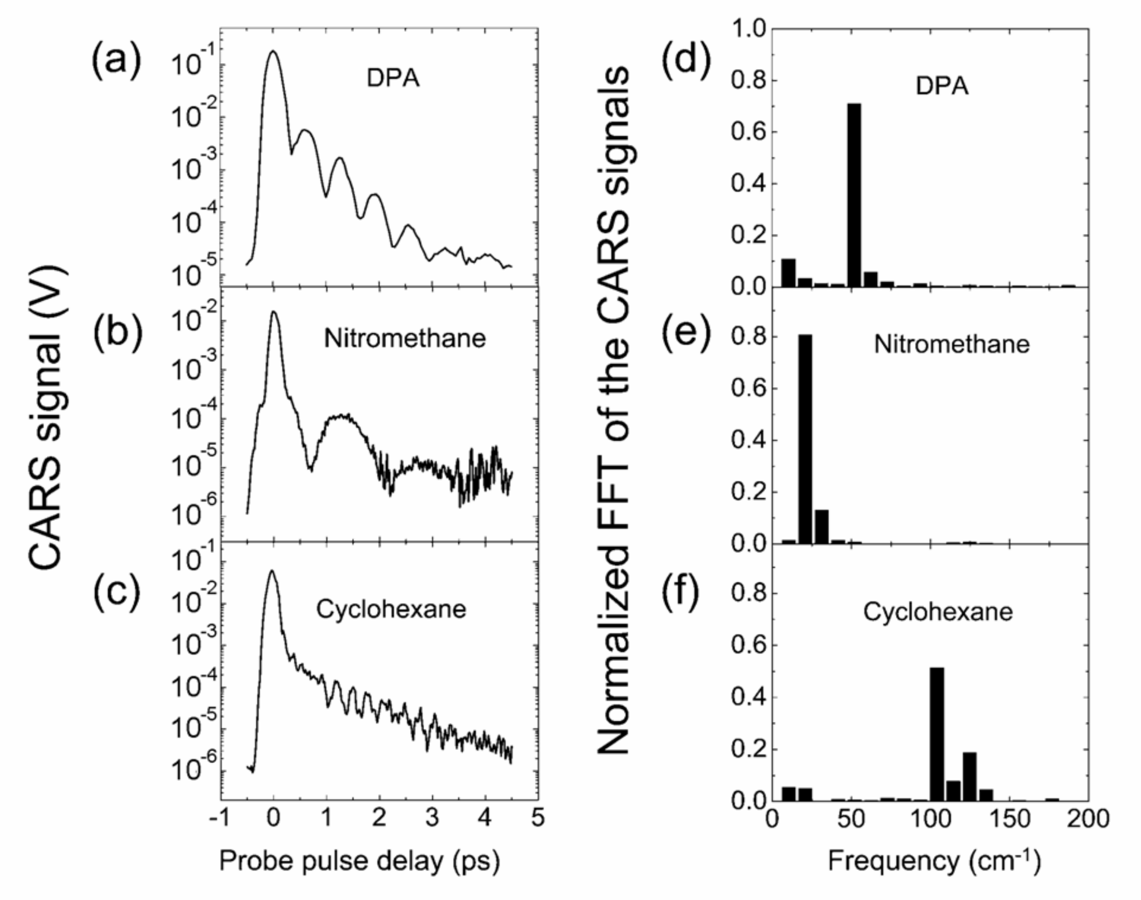

Fig. 4.2. Time-resolved CARS measurements on (a) KOH-buffered solution of DPA, (b) nitromethane, and (c) cyclohexane. (d-f) Corresponding normalized FFTs of the CARS data. The central wavelength of the pump, Stokes, and probe pulses are 382, 404, and 660 nm, respectively. Each plot is normalized to the total area of the FFT after removing the DC component. Characteristic beat frequencies of the molecules are revealed. [41]

the literature [8]. The nitromethane and cyclohexane molecules show their characteristic mode beatings as well.

The beat frequencies between contributing Raman modes, are obtained by performing Fast-Fourier Transform (FFT) on the CARS traces. The NR FWM signal, near zero probe pulse delay, is eliminated by considering probe delays larger than 0.25 ps. Figs. 4.2(d-f) show the FFT spectra corresponding to the three molecules mentioned above. We normalize the temporal curves by multiplying them with the function $\exp(t/\tau)$ to compensate for the exponential decay of vibrational coherences. Here τ is an average lifetime of the coherence relaxation of each molecule obtained by fitting the temporal data with an exponential decay. Each FFT spectrum is normalized to the total area of the FFT after removing the DC component (frequency components below 5 cm^{-1}). Table 4.1 compares our measurements (the fourth column) with those found in literature. The second column lists the Raman lines near 1400 cm^{-1} found in literature [8, 30] and online NIST database [44], and the third column extracts the beat frequencies from those lines. The beat frequencies from the measurements match very well with those from literature for the first four listed molecules, where at least two vibrational modes are excited. Acetonitrile, gasoline, and some alcohols (see Table 4.1) have only one vibrational mode near 1400 cm^{-1}, so we observe an exponential decay as expected. The last row lists the molecules that have no Raman lines near 1400 cm^{-1}, with no signal observed in our CARS measurements. It is worth noting that the spectral resolution is about 10 cm^{-1}, determined by the time duration during which the resonant signals relax to below the noise level, whereas the spectral width of the laser pulses are much larger.

CSRS traces, recorded in the second experiment, are expected to be similar to those obtained from CARS measurements (assuming there is no one-photon resonance with excited electronic states). However, in the second arrangement the laser pulses have twice the bandwidth of those used in the first experiment. This implies that the band of Raman transitions spanned by the convolution of the pump and Stokes pulses is wider and explains somewhat richer dynamics imprinted on CSRS traces of NaDPA (DPA in

H_2O/NaOH solution) and a neat solution of cyclohexane (see Figs. 4.3 and 4.4). CSRS traces for two other representative and very common chemicals, ethanol and acetone, are given respectively in Figs. 4.5 and 4.6.

Besides the properties of the laser pulses used in different experiments, an additional free parameter that has been left out of the discussion so far is the wavelength at which CARS or CSRS signals are acquired. To emphasize the similarity of CARS and CSRS, on one hand, and the dependence of the recorded traces on the acquisition wavelength, on the other, we have performed a series of CARS and CSRS measurement with the same sample and laser setup but various set wavelengths of the monochromator. The results are summarized in Figs. 4.7 and 4.8. As one can see, the spectrograms for CARS and CSRS on NaDPA solution are indeed similar, with the expected mirror-like symmetry with respect to the probe wavelength. However, they do exhibit a non-trivial dependence on the acquisition wavelength. In particular, the cross-sections of the obtained spectrograms at 306.5 nm (CARS, Fig. 4.7(b)) and 335.5 nm (CSRS, Fig. 4.8(b)) are well-fitted with an interference pattern of two decaying Raman modes with difference frequency corresponding to about 50 cm^{-1}. The cross-sections at 305.5 nm (CARS, Fig. 4.7(c)) and 307 nm (CSRS, Fig. 4.8(c)), however, have more complex profiles indicating the presence of a third excited Raman mode.

Table 4.1. Comparison of beat frequencies between CARS measurements and literature. [41]

Molecule	Raman lines near 1400 cm^{-1}	Extracted beat frequencies	Measured beat frequencies (this work)
DPA	1395, 1446, 1579	51, 133	(51, 133) ±10
Nitromethane	1378, 1402	24	20±10
Cyclohexane	1157, 1266, 1347, 1443, 1465	22, 96, 118, 177, 308	(15, 102, 122, 180, 305) ±10
Acetone	1221, 1356, 1430	74, 209	(64, 194) ±10
Acetonitrile, gasoline	Single line	No beating	Exponential decay
Alcohols[a]	~1460	No beating	Exponential decay
Others[b]	No lines	No beating	No signal

[a] Butanol, ethanol, methanol, and propanol.
[b] Includes chloroform, diesel fuel, pyridine, and water.

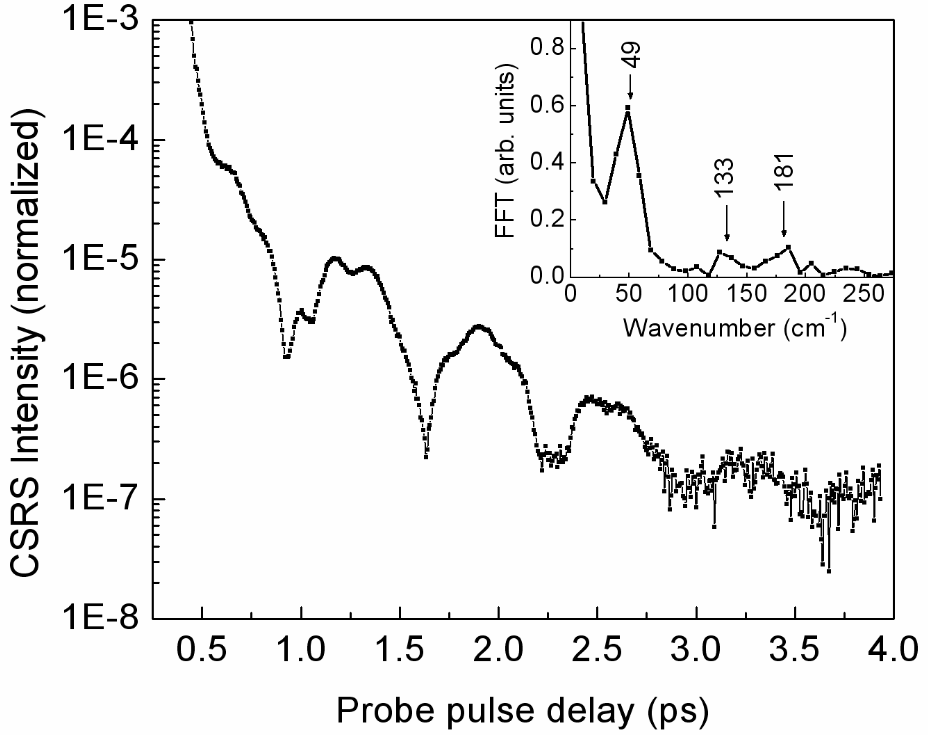

Fig. 4.3. Time-resolved CSRS measurements on NaDPA solution: Normalized intensity as a function of the probe pulse delay obtained for 115 mM solution of DPA in H_2O/NaOH (pH = 12). The sample is put into a quartz cuvette with 2-mm optical path. Pulse parameters: pump - λ_1 = 636 nm, 1.9 μJ/pulse; Stokes - λ_2 = 583 nm, 6.3 μJ/pulse; probe - λ_3 = 320 nm, 0.29 μJ/pulse. The monochromator is set at 335 nm. Inset: FFT of the recorded modulation, corrected for the exponential decay.

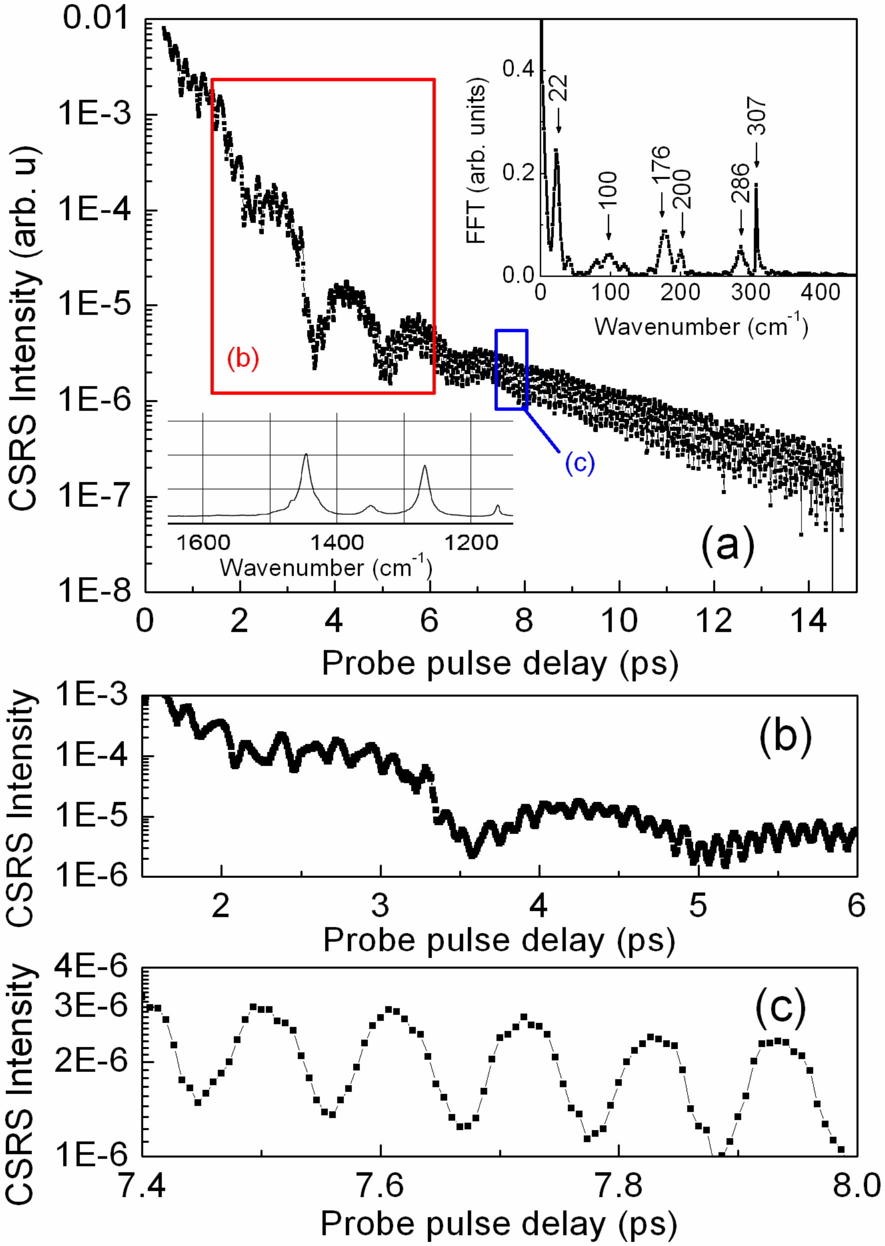

Fig. 4.4. CSRS on a neat solution of cyclohexane (molecular formula - C_6H_{12}): (a) Normalized intensity as a function of the probe pulse delay. Pulse parameters and sampling are the same as in Fig. 4.3. Inset: (top-right) FFT of the recorded modulation, corrected for the exponential decay; (bottom-left) FT-IR Raman spectrum of cyclohexane (courtesy of www.sigmaaldrich.com); (b) Zoom-in on the time interval between 1.5 and 6 ps, showing a transition between different groups of interfering vibrational modes; (c) Zoom-in on the time interval between 7.4 and 8 ps, showing a high-frequency beat ($\Delta\nu \approx 307$ cm^{-1}) between two long-living Raman modes.

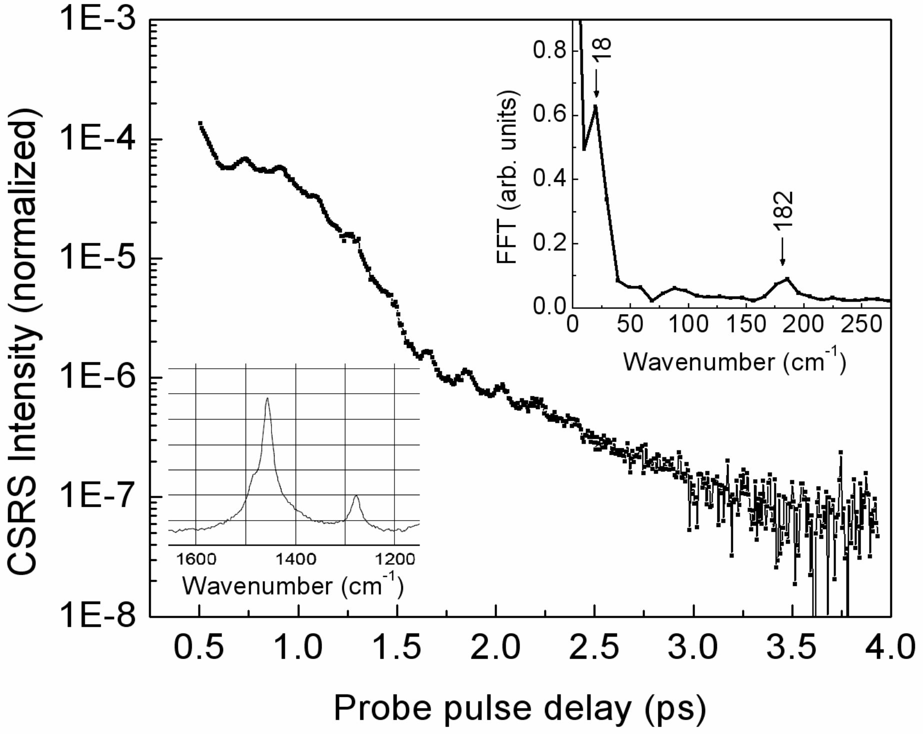

Fig. 4.5. CSRS on a neat solution of ethyl alcohol (molecular formula - C_2H_5OH): Normalized intensity as a function of the probe pulse delay. Pulse parameters and sampling are the same as in Fig. 4.3. Inset: (top-right) FFT of the recorded modulation, corrected for the exponential decay; (bottom-left) FT-IR Raman spectrum of ethyl alcohol (courtesy of www.sigmaaldrich.com).

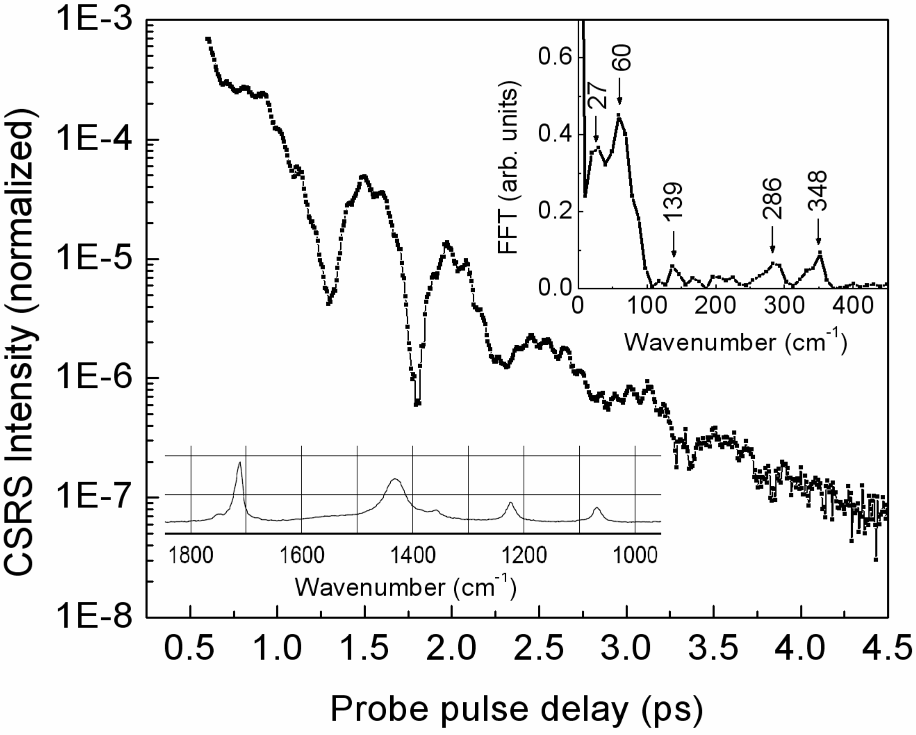

Fig. 4.6. CSRS on a neat solution of acetone (molecular formula - CH_3COCH_3): Normalized intensity as a function of the probe pulse delay. Pulse parameters and sampling are the same as in Fig. 4.3. Inset: (top-right) FFT of the recorded modulation, corrected for the exponential decay; (bottom-left) FT-IR Raman spectrum of acetone (courtesy of www.sigmaaldrich.com).

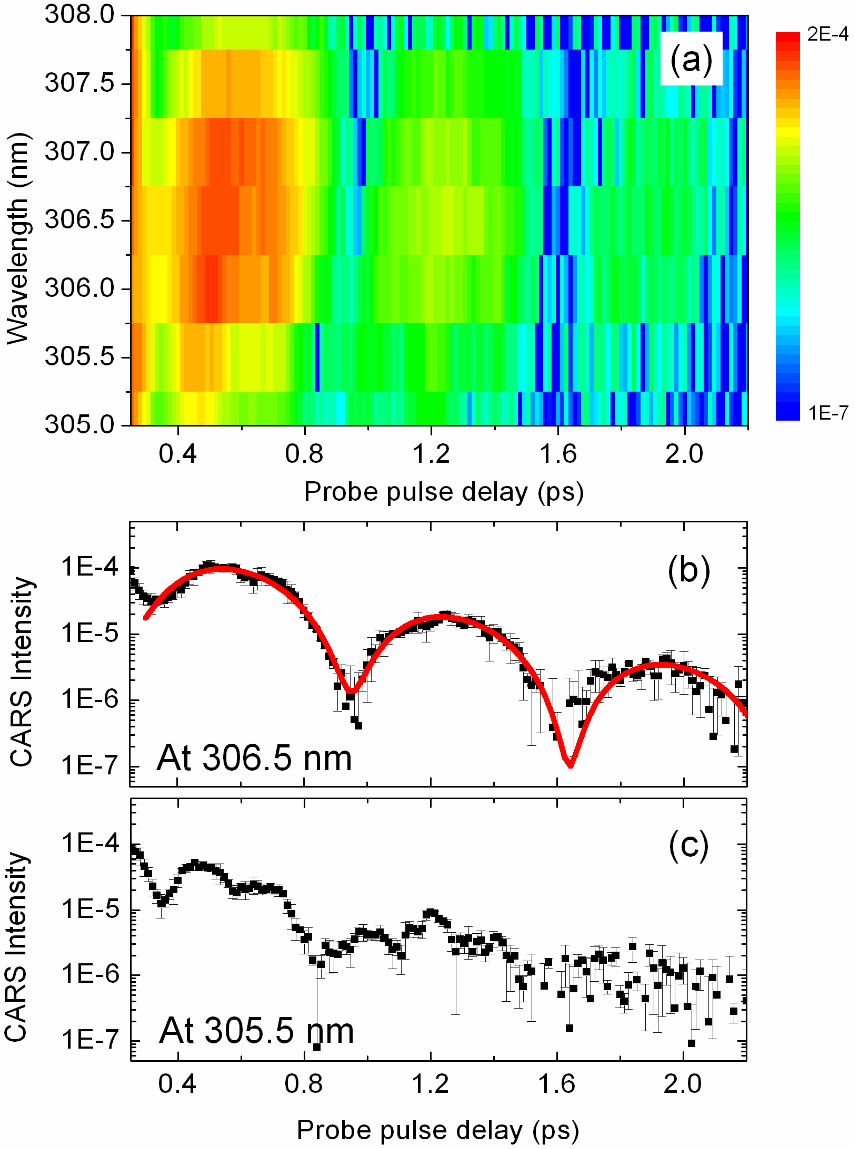

Fig. 4.7. CARS spectrogram for a solution of DPA in H_2O/NaOH: (a) CARS spectrum as a function of the probe pulse delay. The 2D plot is a combination of several CARS traces recorded for different set wavelengths of a monochromator with PMT. The pump, Stokes, and probe wavelengths are 585 nm, 640 nm, and 320 nm, respectively; (b) Cross-section of the spectrogram at $\lambda = 306.5$ nm. The red curve is a fit of the recorded beating. The retrieved values for the beat frequency and dephasing constants are: $\Delta\nu = 48\pm2$ cm^{-1}, $T_2' = 0.92\pm0.13$ ps, $T_2'' = 0.78\pm0.09$ ps; (c) Cross-section of the spectrogram at $\lambda = 305.5$ nm. The higher frequency beat indicates the presence of the third excited Raman mode.

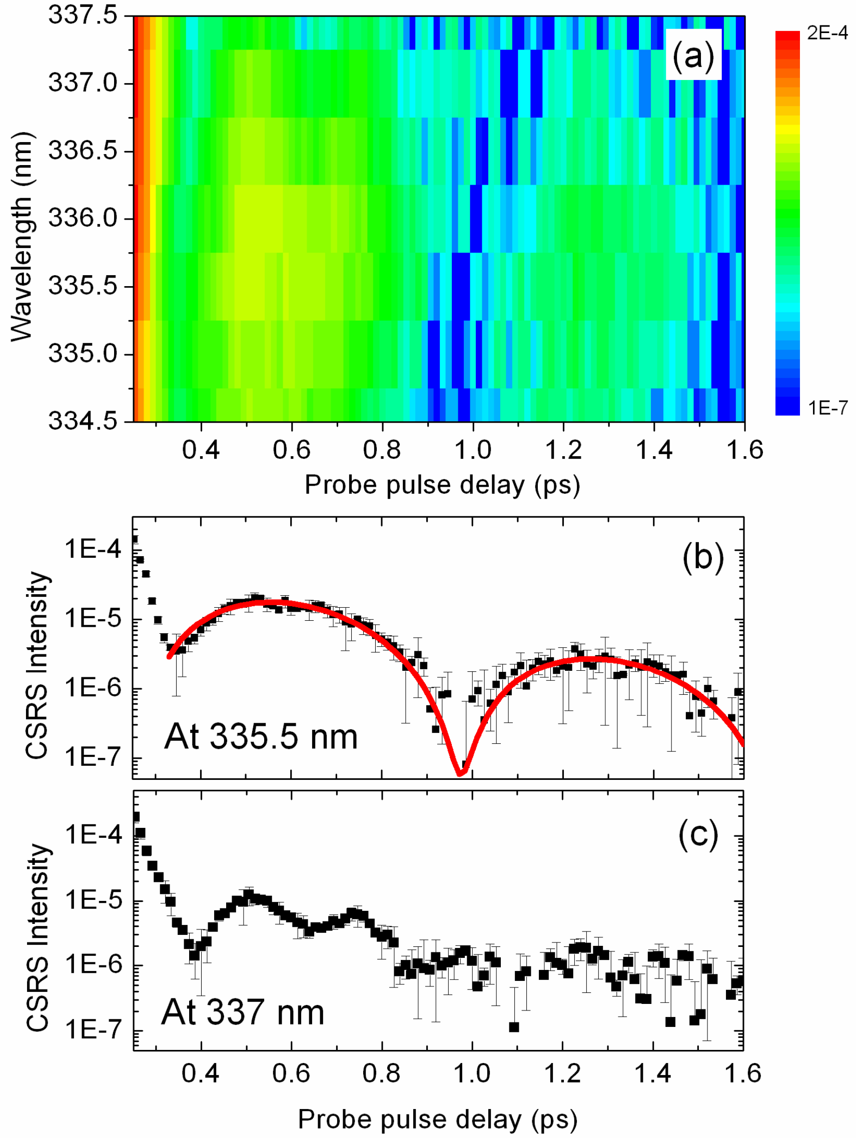

Fig. 4.8. CSRS spectrogram for a solution of DPA in H_2O/NaOH: (a) CSRS spectrum as a function of the probe pulse delay. The 2D plot is a combination of several CSRS traces recorded for different set wavelengths of a monochromator with PMT. The excitation and probe wavelengths as well as the sample are the same; (b) Cross-section of the spectrogram at λ = 335.5 nm. The red curve is a fit of the recorded beating. The retrieved values for the beat frequency and dephasing constants are: $\Delta\nu$ = 45±3 cm^{-1}, T_2' = 0.76±0.09 ps, T_2'' = 0.75±0.08 ps; (c) Cross-section of the spectrogram at λ = 337 nm. The higher frequency beat indicates the presence of the third excited Raman mode.

The implementation of multi-channel acquisition of coherent Raman photons by means of the CCD attached to a spectrograph (Fig. 4.1(c)) allows obtaining the described above spectrograms in a single scan along the probe pulse delay. Shown in Fig. 4.9(a) is a typical CSRS trace for NaDPA solution with the excitation of Raman transitions near 1400 cm^{-1}. The calibration accuracy of the wavelengths in the vertical axis is about 5 nm. The prominent modulation at 50±10 cm^{-1} (see Fig. 4.9(b)), corresponding to the difference frequency between the Raman lines 1383 cm^{-1} and 1435 cm^{-1}, is accompanied by the beating at 133±10 cm^{-1}, between 1435 cm^{-1} and 1569 cm^{-1} vibrational modes (see Fig. 4.9(c)). This high-frequency modulation is not obvious in the first cross-section.

Spectrograms for two representative interferents, acetone and cyclohexane, are given in Figs. 4.10 and 4.11. They were recorded for a similar set of the pulses, probing the same frequency domain of their Raman spectra as for NaDPA above. Two cross-sections of the spectrogram for acetone, shown in Fig. 4.10(b,c), exhibit qualitatively different dependence of the signal on the probe pulse delay. While the first cross-section shows a simple exponential decay of a strong vibrational mode (1430 cm^{-1}), the second one brings up modulation at the frequency of 64±10 cm^{-1}, corresponding to the beat frequency of 74 cm^{-1} between the 1356 cm^{-1} and 1430 cm^{-1} Raman lines. We also observe the beating at 194±10 cm^{-1} between the 1221 cm^{-1} and 1430 cm^{-1} Raman lines.

The spectrogram for cyclohexane is a superposition of multiple excited vibrational modes, and FFT analysis is necessary to retrieve all beat frequencies from the shown time-resolved data. The beating at 22±10 cm^{-1} between the 1443 cm^{-1} and 1465 cm^{-1} modes is most obvious (Fig. 4.11(b), compare to Fig. 4.4). The noticeable change in the decay is a result of interplay between two Raman modes: a strong mode with a short relaxation time and a weak one with a long relaxation time. The second trace (see Fig. 4.11(c), compare to Fig. 4.4) has a well-defined high frequency modulation. At large probe pulse delays its frequency is 305±10 cm^{-1}, which is believed to be the beating between the 1157 cm^{-1} and 1465 cm^{-1} vibrational modes. The beating between the 1266 cm^{-1} and 1443 cm^{-1} lines is also observed. The measured beat frequencies of these molecules are also listed in Table 4.1.

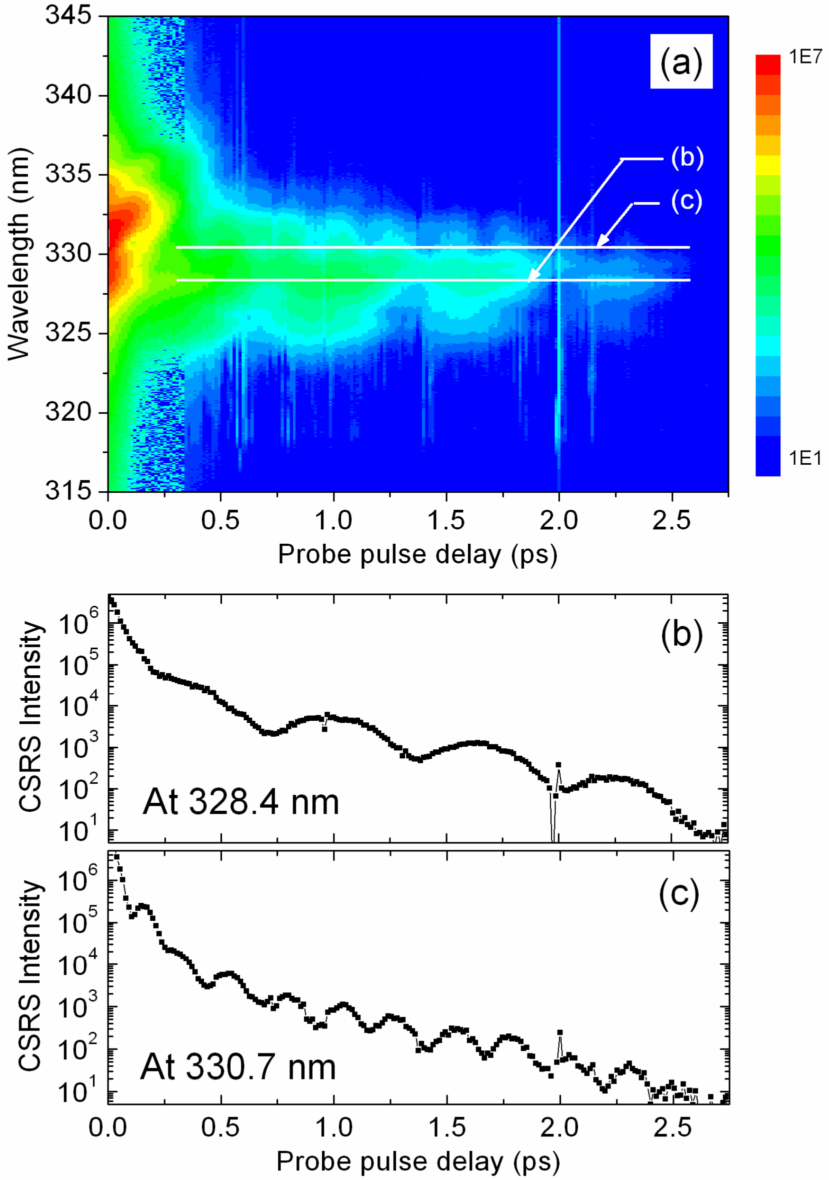

Fig. 4.9. CSRS spectrogram on 230 mM solution of DPA in H_2O/NaOH: (a) Spectrogram acquired with a spectrograph and CCD as a detector; (b,c) cross-sections along the probe delay. Pulse parameters: pump - λ_1 = 582 nm, 2.8 µJ/pulse; Stokes - λ_2 = 636 nm, 2.6 µJ/pulse; probe - λ_3 = 320 nm, 0.31 µJ/pulse. The three beams are arranged in a folded-BoxCARS geometry and focused with 40-50 cm focal length lenses on a quartz cuvette filled with a solution sample. The cuvette has a 2 mm optical path length. The acquisition time is 100 ms per step. The systematic shift of the recorded CSRS spectrum, as compared to the one in Fig. 4.6, is most-probably due to mis-calibration of the spectrometer.

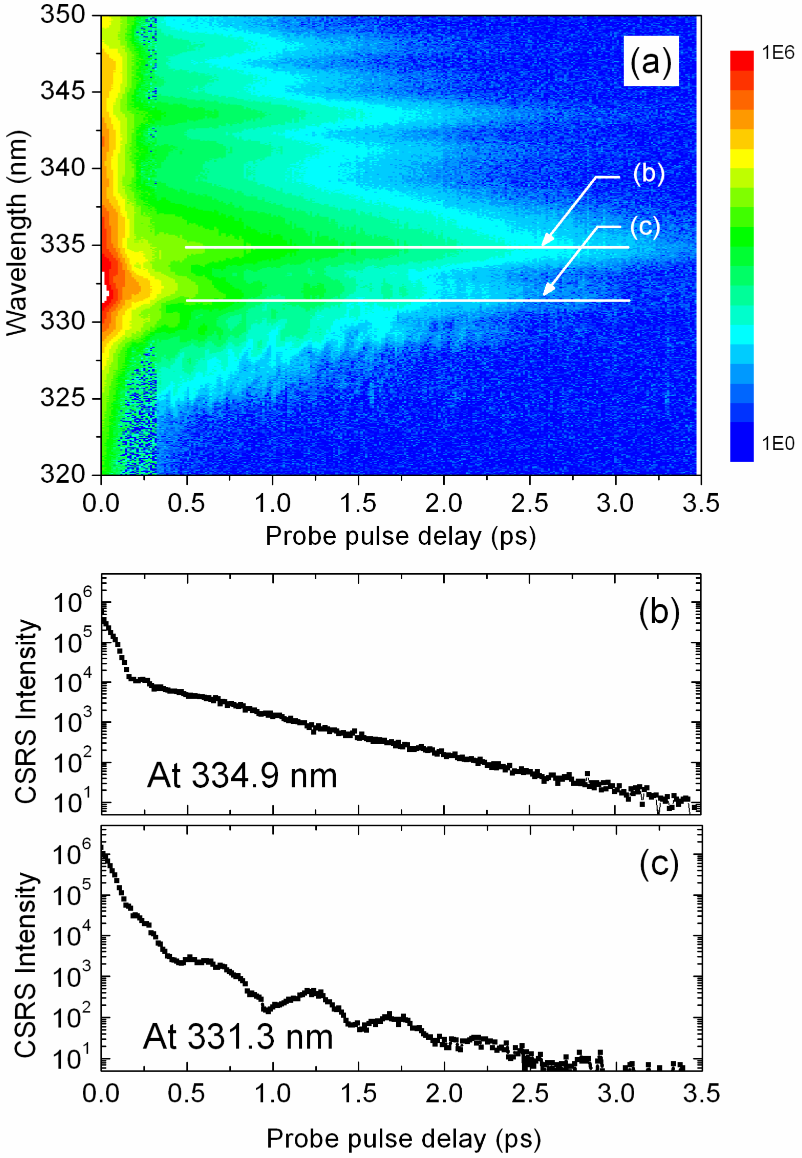

Fig. 4.10. CSRS spectrogram on a neat solution of acetone: (a) Spectrogram acquired with a spectrograph and CCD as a detector; (b,c) cross-sections along the probe delay. Pulse parameters: pump - λ_1 = 583 nm, 2.8 μJ/pulse; Stokes - λ_2 = 636 nm, 6.0 μJ/pulse; probe - λ_3 = 320 nm, 0.16 μJ/pulse. Other parameters are the same as in Fig. 4.9.

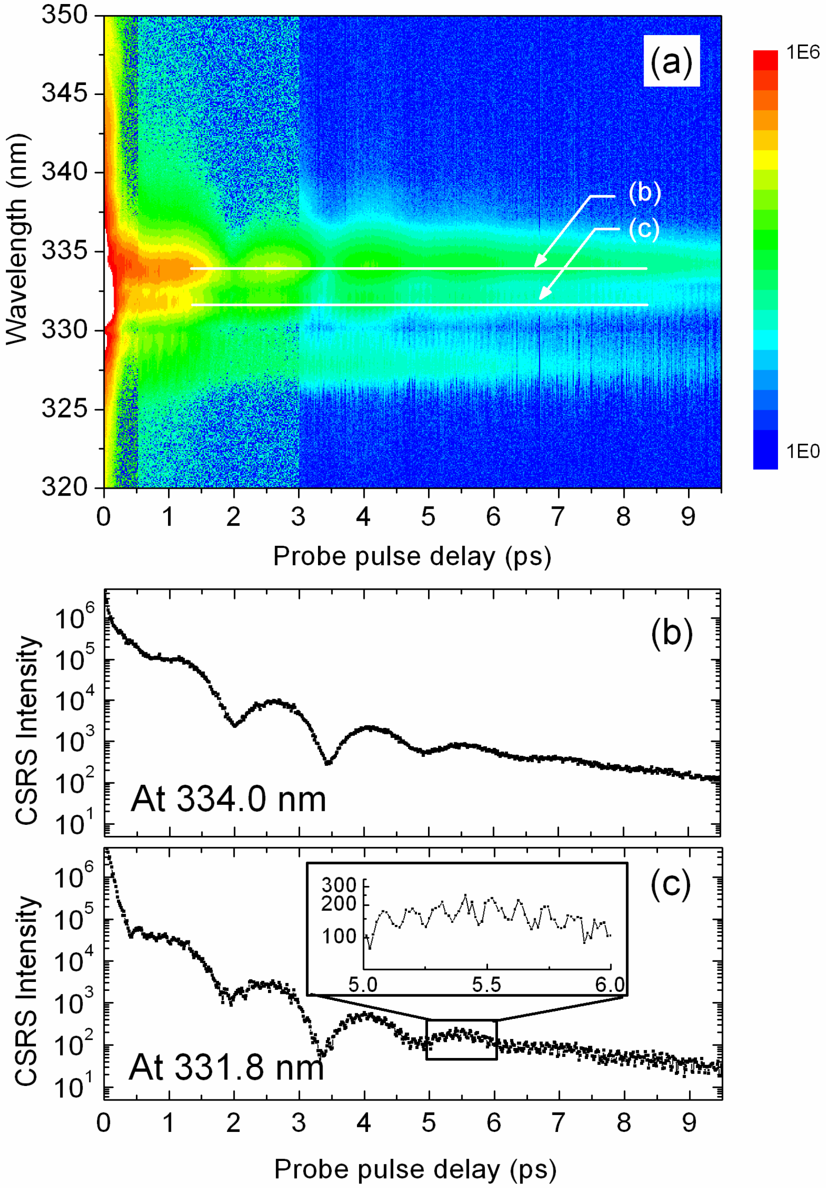

Fig. 4.11. CSRS spectrogram on a neat solution of cyclohexane: (a) Spectrogram acquired with a spectrograph and CCD as a detector; (b,c) cross-sections along the probe delay. Experimental parameters are the same as in Fig. 4.10.

As one can see, spectrograms bring more clarity into the picture of multiple-mode interference and might be indispensable in order to fully decipher molecular signatures, which are generally blended in with the signal from other molecules. The complexity of the interference pattern (defined through the number of frequency shifts in the signal FFT spectrum) scales as $1/2\times N(N-1) \sim N^2$ with the number of contributing Raman modes, N, and leads to highly-congested FFT spectra. The extra dimension added to the field of the control parameters, spectrally-resolved acquisition, has the potential to overcome this difficulty.

3. An Example of Detection Algorithm

As it was mentioned above, the FFT spectra can be used for molecule identification. Here we limit ourselves to the single-channel CARS data, obtained in the first experiment for a fixed acquisition wavelength corresponding to the maximal-contrast beating between the two excited Raman modes of DPA in H_2O/KOH. We are interested in the differentiation of DPA from other interferential molecules based on the beat at 51 cm^{-1}. Therefore, we define a specificity parameter

$$\eta = F(n_b \nu_0) / \sum_{n=n_L}^{n_H} F(n\nu_0) \tag{4.1}$$

as the normalized frequency component at 51 cm^{-1}, which is DPA's characteristic beat frequency. Here $F(n\nu_0)$ is the FFT spectrum, ν_0 is the frequency discretization size of the FFT, n is an integer, $n_b\nu_0$ equals to the mode beat frequency (in this case 51 cm^{-1}); $n_L\nu_0$ is the low cutoff frequency to eliminate the DC component, and $n_H\nu_0$ is the high cutoff frequency determined by the spectral width of the pulses. In our case, ν_0 = 10.2 cm^{-1}, n_b = 5, n_L = 1, and n_H = 19. A larger value of the specificity parameter indicates a higher probability for the target to be DPA. To enhance the discrimination contrast, the temporal traces of all interferents are multiplied by $\exp(t/\tau_0)$, where the average decay time of the DPA vibrational modes near 1400 cm^{-1}, τ_0 = 0.5 ps, is used instead of their own mode decay times. Figure 4.12 shows calculated η-values for the fifteen molecules

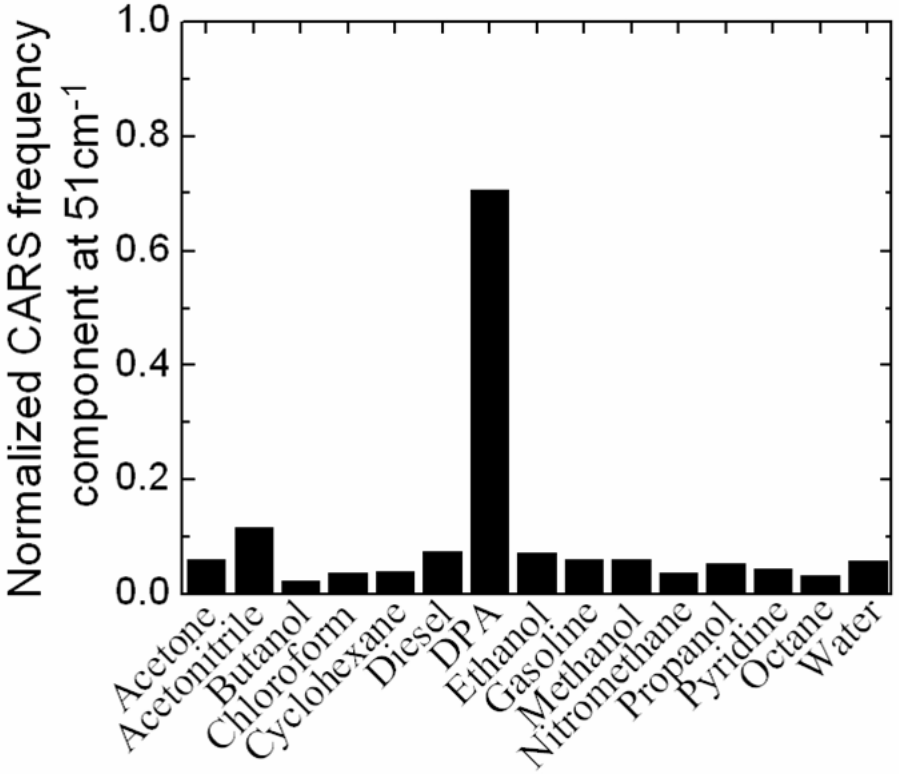

Fig. 4.12. Normalized FFT component at 51 cm^{-1} of DPA and its interferents. [41]

tried in the experiment. The DPA interferents are common chemical species. The contrast between the DPA and the interferents shows good identification specificity.

4. Concentration Dependence

It is known that DPA molecules exhibit a large absorption cross-section at about 272 nm, which corresponds to a one-photon transition from the ground molecular state into the closest excited electronic state (see Appendix A). Obviously, the presence of the electronic resonance should affect Raman cross-sections of molecular vibrations. In particular, theory based on a simplified three-level model suggests that the use of electronically resonant optical fields leads to the enhanced efficiency of coherent Raman scattering processes [25, 45]. The model, however, does not include laser pulse propagation effects, dependent upon absorption and dispersion of the medium. It also does not account for the laser-induced damage of the sample, which could be a strong limiting factor for successful experimental implementation of this idea.

In this section, we report on the concentration dependence study with near-resonant UV probe and off-resonant preparation laser pulses. The setup shown in Fig. 4.1(b) is used. Keeping the wavelengths and therefore, the Raman cross-sections fixed, we change the concentration of DPA molecules in H_2O/NaOH solution and monitor the intensity of CARS and CSRS at the first peak of the oscillation arising from the interference between Raman modes at 1383 and 1435 cm^{-1} (which usually occurs between 0.3 and 0.6 ps probe delay).

The typical data set, recorded for CARS, is shown in Fig. 4.13. The extracted concentration dependences for CARS and CSRS are summarized in Fig. 4.14. The concentration curves show similar features with minor deviations. In particular, the CARS pulse energy has a maximum at about 152 mM, while CSRS peaks at 252 mM. This can be explained by the fact that the CARS signal has relatively higher absorption cross-section since the absorption peak of NaDPA solution is near 272 nm (Appendix A). The theoretical curves obtained from our model, which will be discussed next, are shown together with the experimental data. The theoretical results are normalized in the same way as the experimental data.

Intuitively, the concentration dependence can be well understood from the two limits. On one hand, when there is no DPA in the solution, there should be no signal, and adding DPA will result in the growth of the signal. The power law dependence of the signal on concentration in this limit is well known. On the other hand, if there is too much DPA in the solution, both the signal and the probe pulse will get absorbed. As a result, the signal rolls over as the concentration increases after the peak value.

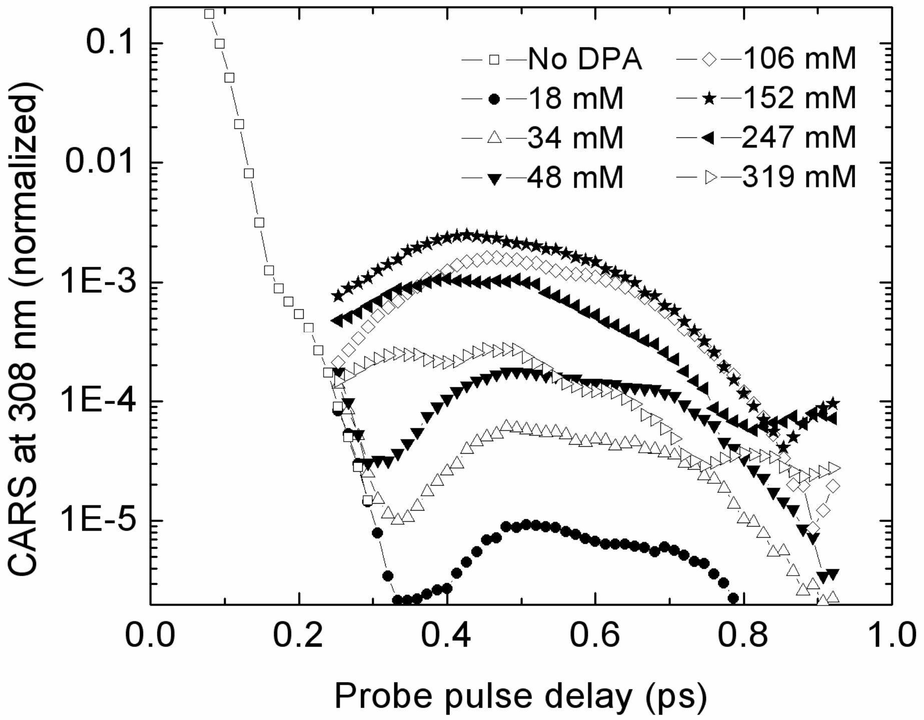

Fig. 4.13. CARS pulse energy as a function of the probe pulse delay at different concentrations of DPA in H_2O/NaOH solution. Sample: NaDPA solution in a quartz cell with 2 mm optical path. The pH value of the solution is 13-14. The wavelengths of the pump, Stokes, and probe pulses are 585 nm, 640 nm, and 320 nm, respectively. The signal is normalized on the FWM peak, at zero probe delay, for pure NaOH solution (no DPA). [42]

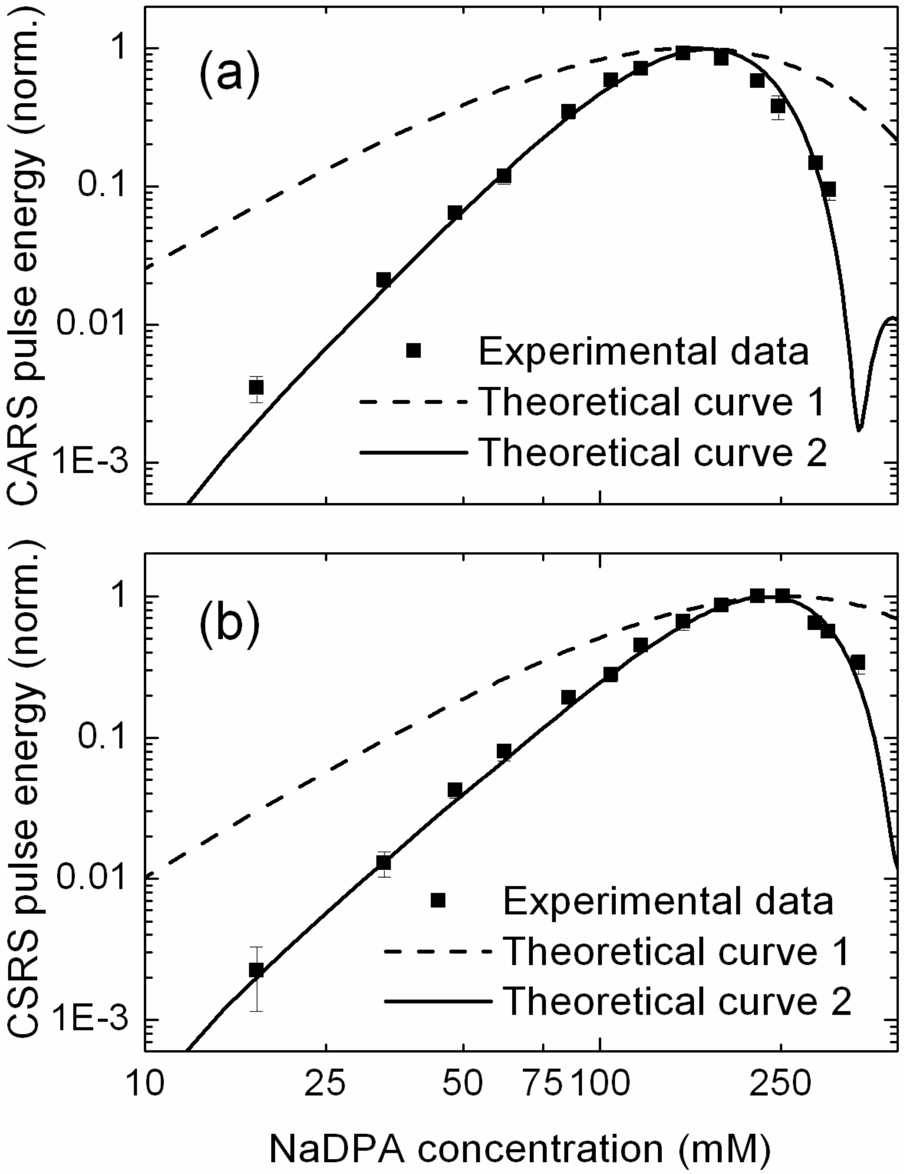

Fig. 4.14. Log-log plot of CARS (a) and CSRS (b) pulse energy at the peak of the oscillation as a function of NaDPA concentration. Sample: NaDPA solution in a quartz cell with 2 mm optical path. The dashed curve is the result of theoretical calculations under assumption that phase-matching condition is fulfilled for all concentrations ($\Delta k_s \equiv 0$). At low NaDPA concentration, this curve has a slope of 2. The solid curve is the theoretical fit obtained with the concentration-dependent phase mismatch included ($\Delta k_s \neq 0$). [42]

A simple model that explicitly includes absorption for the probe and generated fields, but not for the driving fields, is developed here to back up this intuitive consideration. Within our 1D model, the field amplitudes are governed by the following equations:

$$E_3(z) = E_3(0) \times \exp(-\alpha_3 z N/2), \tag{4.2}$$

$$\frac{d}{dz} E_s(z) = -\frac{1}{2} N \cdot \left[\alpha_s E_s(z) - \kappa \rho_{bc} E_3(z) \times \exp(i \Delta k_s z)\right]. \tag{4.3}$$

Here κ is a coupling constant, N is the NaDPA molecule concentration, α_3 and α_s are the absorption cross-sections of probe and the generated signal pulse respectively, $\Delta k_s \equiv k_s - [k_3 \pm (k_1 - k_2)]$ is the phase mismatch for CARS (plus sign) or CSRS (minus sign), k is the wavevector, and ρ_{bc} is the coherence created by the two visible pump and Stokes pulses [45]. Please to note that the parameter κ has a resonant dependence on the frequency of the probe field and accounts for the resonance enhancement of the

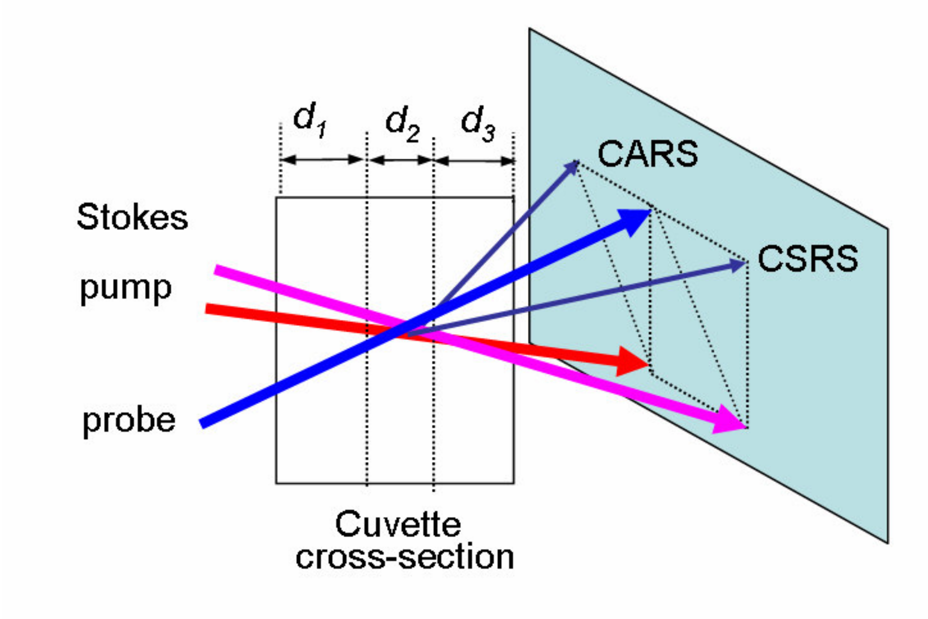

Fig. 4.15. CARS and CSRS generation in a folded-BoxCARS geometry and sectioning of the cuvette for the simplified 1D theoretical model.

signal, mentioned above. We consider three regions of the sample: before interaction (of thickness d_1), interaction region (d_2), and after interaction (d_3), as shown in Fig. 4.15. In our calculations d_1 is set to be equal to d_3 so that less parameters are used to fit the experimental data. $E_3(z)$ is the probe field amplitude and $E_s(z)$ is the signal field, CARS or CSRS.

The implicit assumptions are: (1) there is no absorption or depletion of the two visible pump and Stokes pulses, such that the coherence excitation is independent of concentration; (2) the absorption of the probe and signal fields is linear, i.e. follows the Beer's law. By substituting Eq. (4.2) into Eq. (4.3) and integrating through the three regions, one can derive an analytic expression for $E_s(z)$. The relevant experimental quantity, however, is the signal (CARS or CSRS) intensity $I_s^{out} \equiv |E_s(d_1 + d_2 + d_3)|^2$ after the cuvette, which is given explicitly as

$$\begin{aligned} I_s^{out} &= |\kappa\rho_{bc}|^2 I_3^{in} \times \exp(-N(\alpha_3 d_1 + \alpha_s d_3)) \times \\ &\times \left(N^2 \frac{\exp(-N\alpha_3 d_2) + \exp(-N\alpha_s d_2) - 2 \cdot \exp[-N(\alpha_3 + \alpha_s) d_2 / 2] \cdot \cos(\Delta k_s d_2)}{N^2 (\alpha_3 - \alpha_s)^2 / 4 + \Delta k_s^2} \right), \end{aligned} \tag{4.4}$$

where I_3^{in} is the incident probe-field intensity. Note that the term accounting for the overlap region 2 reduces to $(Nd_2)^2$ for small N and $\Delta k_s \equiv 0$, which gives the square-law dependence on concentration. On the other hand, when there is no absorption, i.e. $\alpha_3 = \alpha_s = 0$, the solution has the form of $|\kappa\rho_{bc}|^2 I_3^{in} (Nd_2)^2 \times \mathrm{sinc}^2(\Delta k_s d_2 / 2)$, with a typical dependence on Δk_s and the interaction length d_2.

We first apply Eq. (4.4) under the assumption of perfect phase matching, $\Delta k_s \equiv 0$. The calculated curves for the CARS and CSRS dependence on the NaDPA concentration are in a qualitative agreement with our experimental results (theoretical curve 1, Figs. 4.14(a) and 4.14(b)). The peak values of CARS and CSRS are about the same as in our measurement. They are 160 mM and 258 mM for CARS and CSRS, respectively. The absorption cross sections used in the calculations are α_3 = 0.042

mM^{-1}·cm^{-1}, α_{CARS} = 0.083 mM^{-1}·cm^{-1}, and α_{CSRS} = 0.036 mM^{-1}·cm^{-1}. They are measured experimentally, as shown in Appendix A. The fitting parameters are $d_1 = d_3 = 0.725$ mm and $d_2 = 0.55$ mm. The interaction length d_2 is close to the estimated one from the beam geometry and dispersion. The other two parameters, d_1 and d_3, are taken equal since we have always tried to center the overlap region in the cuvette.

The theoretical curves exhibit square-law dependence for small concentration of DPA molecules in H_2O/NaOH solution. However, the experimental results show a steeper increase of the signal (the slope is 2.7 on the log-log scale), which can be explained as follows. In our experiment, the geometry of the laser beams is optimized for one particular concentration. The CARS/CSRS signal is measured in the same configuration for different concentrations of NaDPA. However, the calculations show that the absorption of the probe field is substantial because the frequency of the probe beam is close to the resonant electronic transition. Similarly, the resonant dispersion of DPA molecules can contribute and lead to the appearance of phase mismatching for signal generation. The pulse energy has steeper dependence on the concentration of DPA molecules due to the changing refractive index of the NaDPA solution.

To support this explanation we have measured the index of refraction of the NaDPA solution for two concentrations, 50 and 100 mM. The results are summarized in Appendix B. The refractive index of our solution increases noticeably with increasing concentration of DPA molecules. So, we speculate that the phase-matching cannot be satisfied at all concentrations. We perform calculations taking into account the resonant dispersion and reproduce the experimentally observed slope for the signal dependence on the NaDPA concentration. We assume a linear dependence of Δk_s on concentration N, i.e. write $\Delta k_s = a \cdot (N - N_0)$, where N_0 is the point where the phase-matching is satisfied. We use N_0 and a as fitting parameters, and keep the rest of the parameters fixed as given above. The calculated dependences are shown as solid curves in Figs. 4.14(a) and 4.14(b). The parameter values used are N_0 = 170 mM, a_{CARS} = 0.585 mM^{-1}·cm^{-1}, and a_{CSRS} = -0.44 mM^{-1}·cm^{-1}. Note that a_{CARS} has a larger magnitude than

a_{CSRS}, which is as expected since the CARS signal is closer to the absorption peak. We observe a good agreement between our experimental and theoretical results.

To reinforce the arguments above, the same model is applied to CARS data obtained with different laser wavelengths but more importantly, 20 times thinner cuvette (100 μm optical path). In this case, the phase-matching constraint is relaxed and the interaction length is limited by the thickness of the quartz cell ($d_1 = d_3 = 0$; $d_2 = 100$ μm). The data shown in Fig. 4.16 are obtained for the pump, Stokes, and probe wavelengths equal to 726 nm, 806 nm, and 295 nm, respectively. The pump and Stokes beams have several milliwatts of average power on the sample. The UV probe power is ~0.5 mW (0.5 μJ per pulse at 1 kHz). The estimated CARS wavelength is 283 nm. Again, the two Raman modes, 1383 and 1435 cm^{-1}, are excited but the second oscillation peak of the CARS signal (~1.6 ps away from the FWM zero delay) is used to plot the concentration dependence. The experimental data in Fig. 4.16 agree well with the analytical solution for $\Delta k_s \equiv 0$. The parameters $\alpha_3 = 0.508$ mM^{-1}·cm^{-1} and $\alpha_{CARS} = 5.28$ mM^{-1}·cm^{-1} are obtained from the absorption measurements (Appendix A), and therefore no free parameters are used. As expected, the dependence exhibits the slope of 2 (on the log-log scale) at low concentration of DPA molecules in H_2O/NaOH.

We have observed an unambiguous and distinctive signal from as low as 10 mM of DPA in H_2O/NaOH solution put into a 100-μm thick cell. The interaction volume is estimated to be 100 μm×100 μm×100 μm = 10^{-6} cm^3. This corresponds to 6×10^{12} NaDPA molecules contributing to the coherent Raman scattering. The number of DPA molecules (mainly, in the form of CaDPA salt) in a single bacterial spore is about 2×10^9. Assuming that the scattering from different spores adds up coherently in the forward direction, our current setup should be able to detect 3×10^3 spores, which is within the limits of a lethal dosage [46].

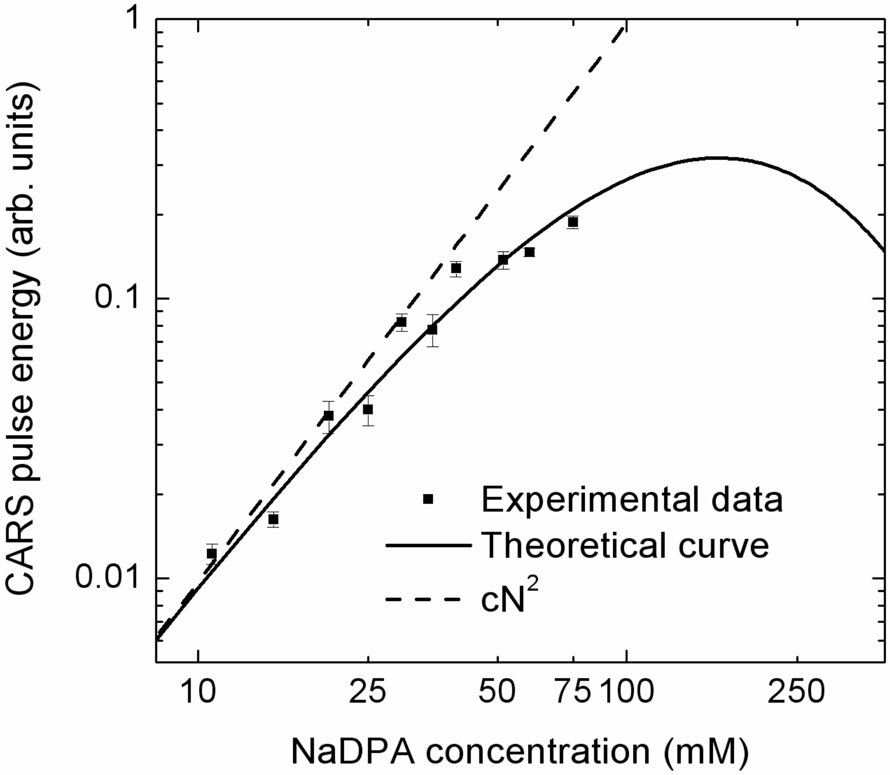

Fig. 4.16. Log-log plot of CARS pulse energy at the second peak of the oscillation as a function of NaDPA concentration. Sample: NaDPA solution in a quartz cell with 100 μm optical path. The solid curve is the result of theoretical calculations under assumption that phase-matching condition is fulfilled for all concentrations ($\Delta k_s \equiv 0$; α_3 = 0.508 $mM^{-1} \cdot cm^{-1}$; α_{CARS} = 5.28 $mM^{-1} \cdot cm^{-1}$). The dashed curve would correspond to the case of negligible absorption. On the vertical scale, 1 arb. unit roughly corresponds to 0.2 fJ/pulse. [42]

5. UV-probe Wavelength Dependence

We have experimentally studied the dependence of the coherent Raman scattering efficiency on the wavelength of the UV probe pulse, near-resonant to the one-photon transition at ~272 nm (see Appendix A) from the ground state of DPA molecule into the lowest excited electronic state. The three-level model (see Fig. 4.17 and Appendix C for notations) gives the following conversion efficiencies of the probe photons into CARS

$$\frac{n_{CARS}}{n_3} \approx \left(\frac{\pi N L |\tilde{\rho}_{bc}|}{2\hbar \varepsilon_0} \right)^2 \frac{|\wp_{ab}|^2 |\wp_{ac}|^2}{\lambda_3 \lambda_{CARS}} \frac{1}{\Delta^2_{CARS} + \gamma^2_{ac}}, \tag{4.5}$$

and CSRS photons

$$\frac{n_{CSRS}}{n_3} \approx \left(\frac{\pi N L |\tilde{\rho}_{bc}|}{2\hbar \varepsilon_0} \right)^2 \frac{|\wp_{ab}|^2 |\wp_{ac}|^2}{\lambda_3 \lambda_{CSRS}} \frac{1}{\Delta^2_{CSRS} + \gamma^2_{ab}}, \tag{4.6}$$

i.e. predicts the enhancement of the scattering efficiency when the probe pulse is tuned on resonance (for clarity, we keep the preparation pulses far-detuned). The model, however, does not account for pulse propagation effects (due to absorption and dispersion of the medium) and the laser-induced damage of the sample, as is mentioned above. It is also based on fairly restrictive assumption that the ro-vibrational structure of the excited electronic state can be replaced with a single energy level |a>. The detuning frequencies and relaxation constants are introduced phenomenologically, making the connection to the real system non-straightforward.

To address this problem experimentally, we have modified the Legend-based setup, described at the beginning of this chapter (see Fig. 4.1(c)) and in Chapter II, to have the coherence excited by the laser pulses from OperA-VIS/UV (λ_1 = 726 nm) and a small fraction of the fundamental beam (λ_2 = 806 nm). More importantly, it is probed now by UV laser pulses from OperA-SFG/UV, whose wavelength can be independently tuned in a wide range of wavelengths, from 237 to 305 nm (two OPA options are used - $2 \cdot (\omega_f + \omega_{Signal})$ and $2 \cdot (\omega_f + \omega_{Idler})$, see Fig. 2.2). A thin cell (100 μm optical path) filled with the solution of DPA in H_2O/NaOH, 25 or 50 mM, is used as a sample. The laser pulse energies vary from one experiment to another but usually are about 1.3 μJ for the pump and Stokes beams, and only 40 nJ for the probe one. The probe pulse energy is kept low (and constant almost over the whole tuning range) to avoid appreciable degradation of the sample during the measurement.

The obtained experimental results are summarized in Fig. 4.18(a). CARS and CSRS data are plotted as a function of detuning (Δ_{CARS} or Δ_{CSRS}, see Fig. 4.17) from the peak of NaDPA absorption, taken to be 272 nm. The gap between -2000 and 0 cm^{-1} is not covered by the OPA options (it is right in-between the two available tuning ranges). The curves are normalized on the pulse energies and acquisition times. Most of the collected data are for 25 mM solution of NaDPA, although in the first three experiments, 50 mM NaDPA solution is used. As one can see, the amplitude of the signal (at the peak of the first interference beat along the probe pulse delay) varies from one measurement

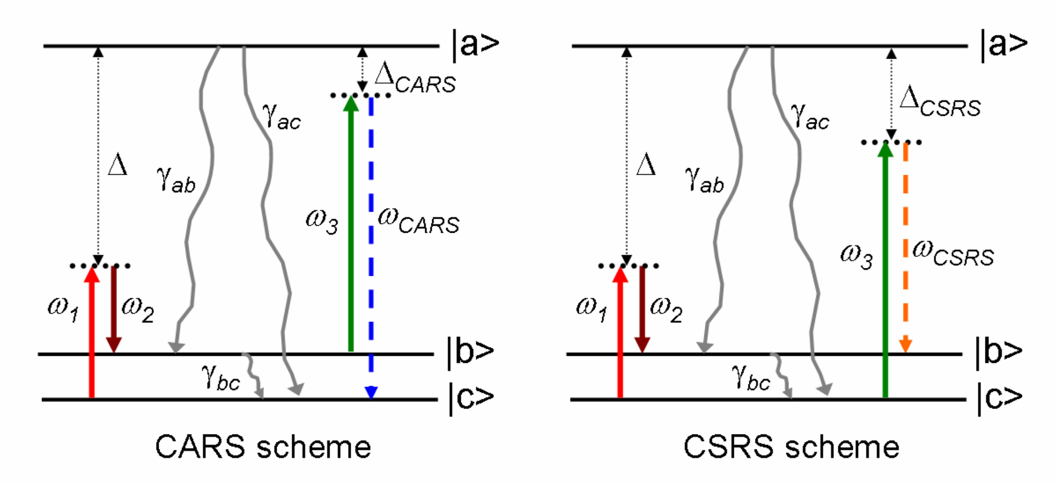

Fig. 4.17. Energy level diagram for CARS (left) and CSRS (right) processes. The probe pulse is near-resonant to the one-photon transition from the ground to the excited electronic state (state |a>). The off-resonant pump (ω_1) and Stokes (ω_2) pulses create the superposition of quantum states |b> and |c> (in the ground electronic state). The third, time-delayed laser pulse (ω_3) scatters off the induced molecular vibrations and gives rise to blue-shifted (ω_{CARS}) and red-shifted (ω_{CSRS}) radiation; γ_{ac}, γ_{ab}, and γ_{bc} are the coherence decay rates between the corresponding quantum states; Δ, Δ_{CARS}, Δ_{CSRS} are detuning frequencies.

to another by a factor a few, which is probably due to different alignment of the beams. However, the qualitative behavior is well reproduced. The signal increases when the probe wavelength is tuned closer to the resonance (from left or right) but ceases near the resonance. We speculate that it is primarily due to the absorption of the probe and scattered photons in the sample that becomes dominant at small detuning.

We account for the absorption and replot the data in Fig. 4.18(b), where every data points is normalized on the so-called transmission factor

$$TF = \left(\frac{\exp(-N\alpha_3 d/2) - \exp(-N\alpha_s d/2)}{N\alpha_3 d/2 - N\alpha_s d/2} \right)^2 . \tag{4.7}$$

This normalization naturally follows from the model outlined in the previous section if $\Delta k_s \equiv 0$ (d = 100 μm is the interaction length), i.e. phase mismatch is not essential. The last assumption might become inadequate in the close vicinity of the absorption peak, where the transmission factor is as low as 0.2. We speculate that it could be the reason for the corrected curves in Fig. 4.18(b) to still dip down near $\Delta = 0$. Another possible reason is the interplay between multiple resonant transitions within the broad absorption peak that our simplified three-level model does not account for. Finally, the near-resonant data points also correspond to the operational limits of the OPA, where up-conversion efficiency is low. The measured probe pulse energies could be partially due to the residual photos from low-frequency harmonics. The quantum beat pattern could also be affected by the pulse shape distortion, expected at the ends of the OPA tuning range.

Overall, in the limit of negligible absorption the observed enhancement of the scattering efficiency (within 237-305 nm range) is about an order of magnitude, which somewhat agrees with the value of $\gamma_{ac}^{-1} \approx 3$ fs [45] estimated from the width of the UV absorption band at 272 nm (the calculated n_{CARS}/n_3 enhancements factor for λ_3 changing from 305 nm to 283 nm is 3.6). From interpolation using Eq. (4.5) or (4.6), one would expect another order (or two) of magnitude difference if compared to the scattering efficiency for the probe photons at visible wavelengths.

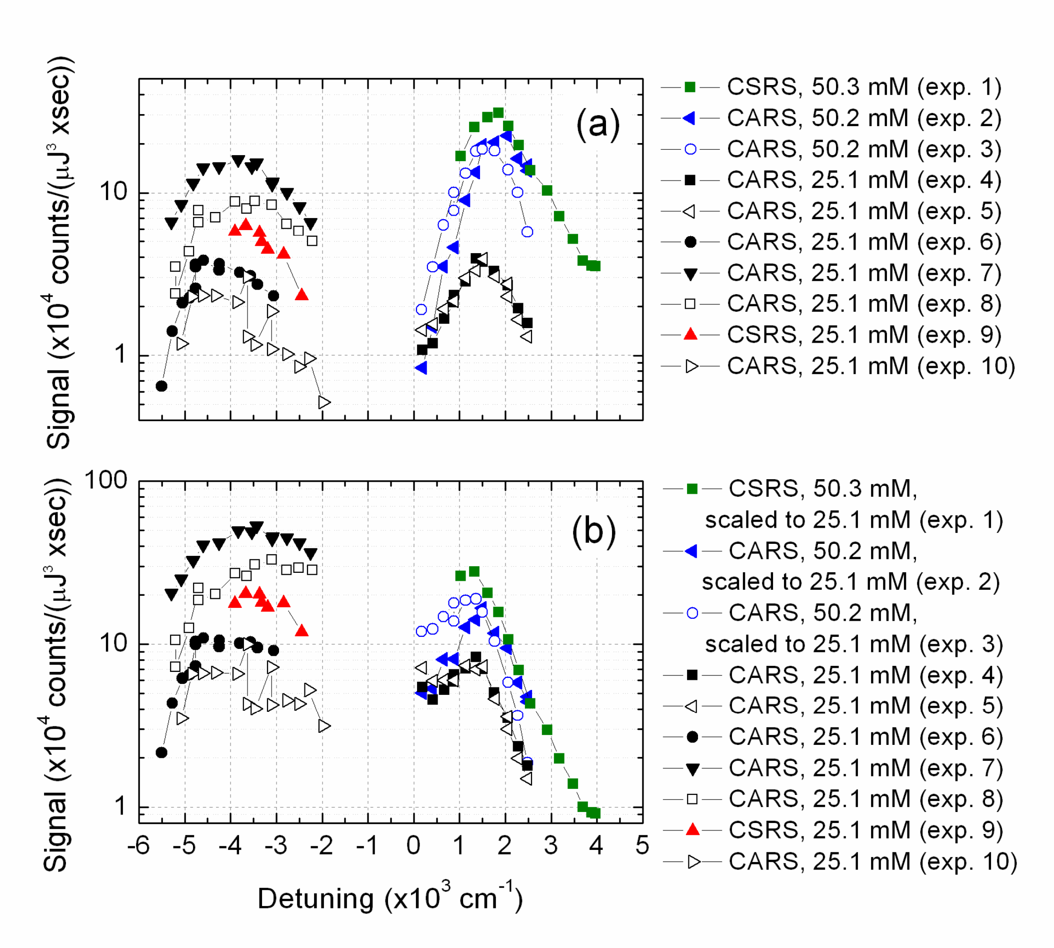

Fig. 4.18. (a) Coherent Raman scattering efficiency as a function of detuning from the electronic transition at 272 nm. The pump and Stokes pulse parameters are fixed. The wavelength of the probe pulse is tuned within 237-305 nm range. The signal (CARS or CSRS) is normalized on the pulse energies and the acquisition time. Sample: 100-μm quartz cell filled with 25 mM or 50 mM solution of DPA in H_2O/NaOH. (b) The data from (a) normalized on the transmission factor defined by Eq. 4.7 and scaled to a single DPA concentration of 25 mM.

In practice, however, this seemingly favorable trend towards UV is overturned by the laser-induced damage of the sample. UV pulse energies on the order of 0.1 μJ (focused into a ~100 μm spot) lead to the gradual degradation of liquid samples and instantaneous damage of solid targets. For photons at, e.g., 578 nm, similar damage occurs at energies of several micro-Joules. In near-IR domain, it scales up to 10 μJ. Another factor in favor of visible and near-IR frequency domains is the availability of sensitive detectors and optical filters. They are not as well developed for UV range.

6. Time-resolved CARS on DPA Powders and Spores

We conclude this chapter with a demonstration of time-resolved CARS on crystalline powders of DPA and NaDPA. A distinct feature that sets these experiments apart from the discussed so far is the sample optical properties. Powders are inherently disordered media. The presence of multiple interfaces results in strong scattering of light, which affects field polarization and phase properties. The coherent Raman scattering signal does not come out of the sample as a well-shaped beam but rather gets re-scattered in all directions. The coherent buildup of the generated field is also limited by the multiple scattering inside the medium. The effective interaction length is obviously correlated with an average grain-size of the powder, although the dependence might be nontrivial.

Based on the insight of the previous studies, we have rearranged the experimental setup to have all laser wavelengths in the visible/near-IR spectral domain. We use 710-730 nm (λ_1, tunable) and ~805 nm (λ_2) photons to trigger coherent molecular vibrations, and then probe those with a 578-nm light (λ_3). As before, the BoxCARS geometry is used for the input beams, but the acquisition part differs. CARS photons are now collected in the backward direction, under about 30° to the normal (to the sample surface) axis. The collected light is partially filtered off of the incoming laser photons and coupled into the spectrograph with a CCD.

CARS spectrogram for DPA powder is shown in Fig. 4.19(a). The expected beating between the Raman modes at 1577 and 1644 cm^{-1} (the frequency difference between the pump and Stokes pulses is tuned towards 1600 cm^{-1}) is imprinted on the slowly decaying CARS signal as a function of the probe pulse delay. Please to note the characteristic narrowing of the acquired spectrum at small probe delays, when CARS overcomes the rapidly diminishing NR FWM contribution. The cross-section of the spectrogram along the CARS trace (see Fig. 4.19(b)) clearly indicates that the contributing Raman modes have different dephasing times. The observed beating quickly transforms into an exponential decay of a single vibrational mode. This dynamics agrees with what one can infer from spontaneous Raman spectrum of crystalline DPA (Fig. 2.7). At last, a reference spectrogram, recorded on a sugar powder, does not exhibit any of the described features except for the NR FWM profile (see Fig. 4.19(c,d)).

As we pointed out earlier, Raman spectra of DPA salts, such as NaDPA or CaDPA, differ from the Raman spectrum of pure DPA. With the preparation pulses tuned towards 1400 cm^{-1}, we have obtained CARS spectrogram of NaDPA powder (see Fig. 4.20). It shows a familiar interference pattern between 1395 and 1442 cm^{-1} Raman modes. We believe the high-frequency beat due to 1572 cm^{-1} mode is not apparent here because of the insufficient effective bandwidth of the probe pulse, cut and distorted by a bandpass filter. The filter is put into the probe beam to remove the optical background at CARS wavelengths.

To summarize, we have successfully demonstrated the applicability of time-resolved technique for CARS on opaque solids. As is shown in the next chapter, we have also managed to combine it with selective Raman excitation through pulse shaping of the pump and Stokes fields. We, however, have failed to observe species-specific CARS signal from B. subtilis spores, chosen as a harmless surrogate for B. anthracis. Typical spectrograms acquired for B. subtilis spores are given in Figs. 4.21 and 4.22. The recorded profiles are purely due to the NR FWM, with no sign of interference or other signatures of Raman-resonant response. Our attempts to vary the acquisition time, the wavelengths and energies of the input laser pulses have not led to the desired outcome. No conclusive evidence of the resonant response has been obtained via time-resolved CARS technique.

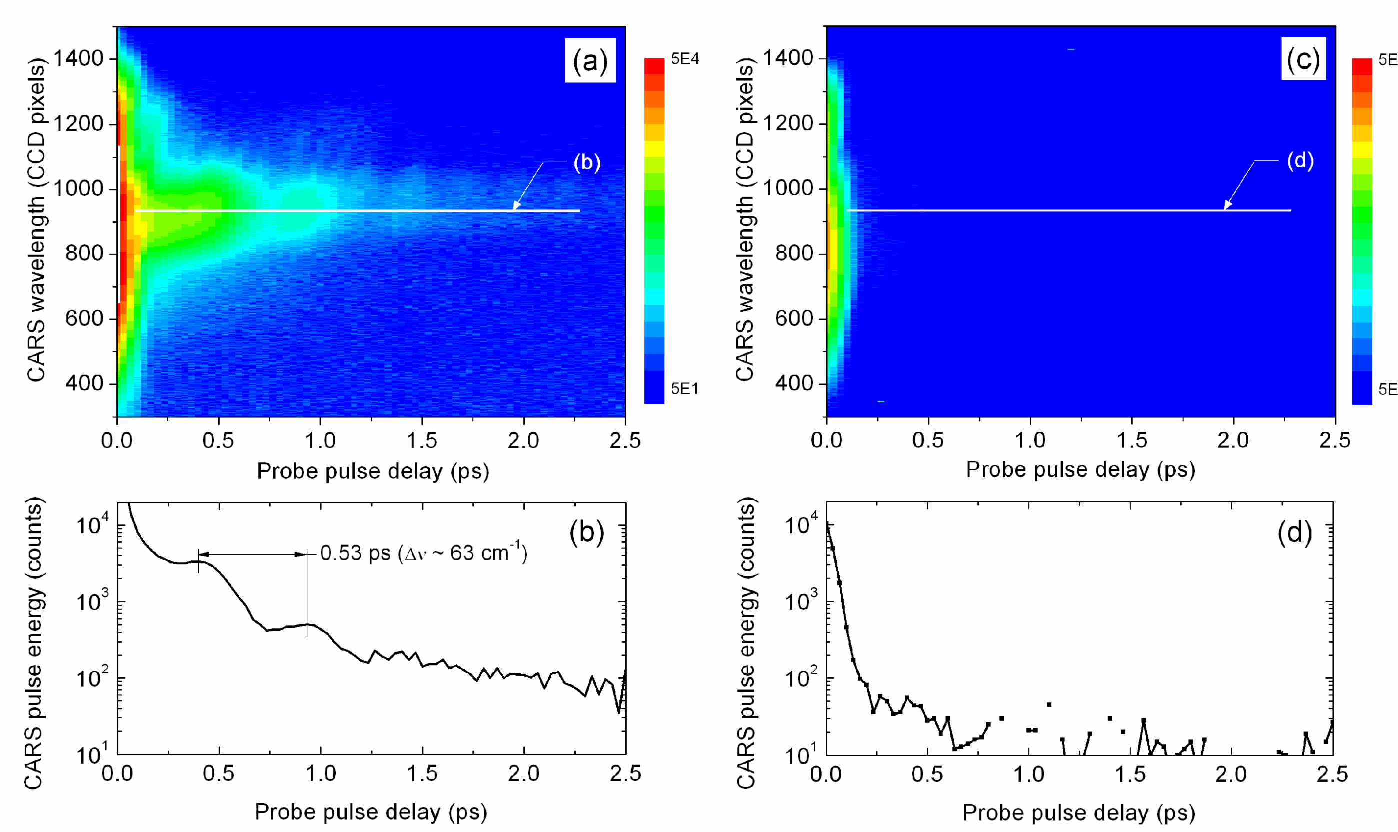

Fig. 4.19. CARS on crystalline DPA powder: (a) CARS spectrogram recorded with a layer of crystalline DPA powder as a sample. Two Raman modes, 1577 and 1644 cm^{-1}, are excited by a pair of ultrashort pulses; (b) a cross-section of the spectrogram along the probe delay; (c) A reference spectrogram recorded with sugar powder as a sample; (d) A cross-section of the spectrogram in Fig. 4.19(c). The three laser beams, focused with 40-50 cm lenses, are overlapped in a BoxCARS geometry. The generated and then scattered signal is collected in the backward direction (slightly off the main axis) by a set of short-focal lenses. The estimated collection angle is $0.02\times4\pi$. Pulse parameters are: pump - λ_1 = 711 nm, 1.0 µJ/pulse; Stokes - λ_2 = 802 nm, 2.5 µJ/pulse; probe - λ_3 = 578 nm, 2.5 µJ/pulse. The spectrograph set wavelength is 528 nm. The acquisition time is 4 s per step (2 s for signal, 2 s for background).

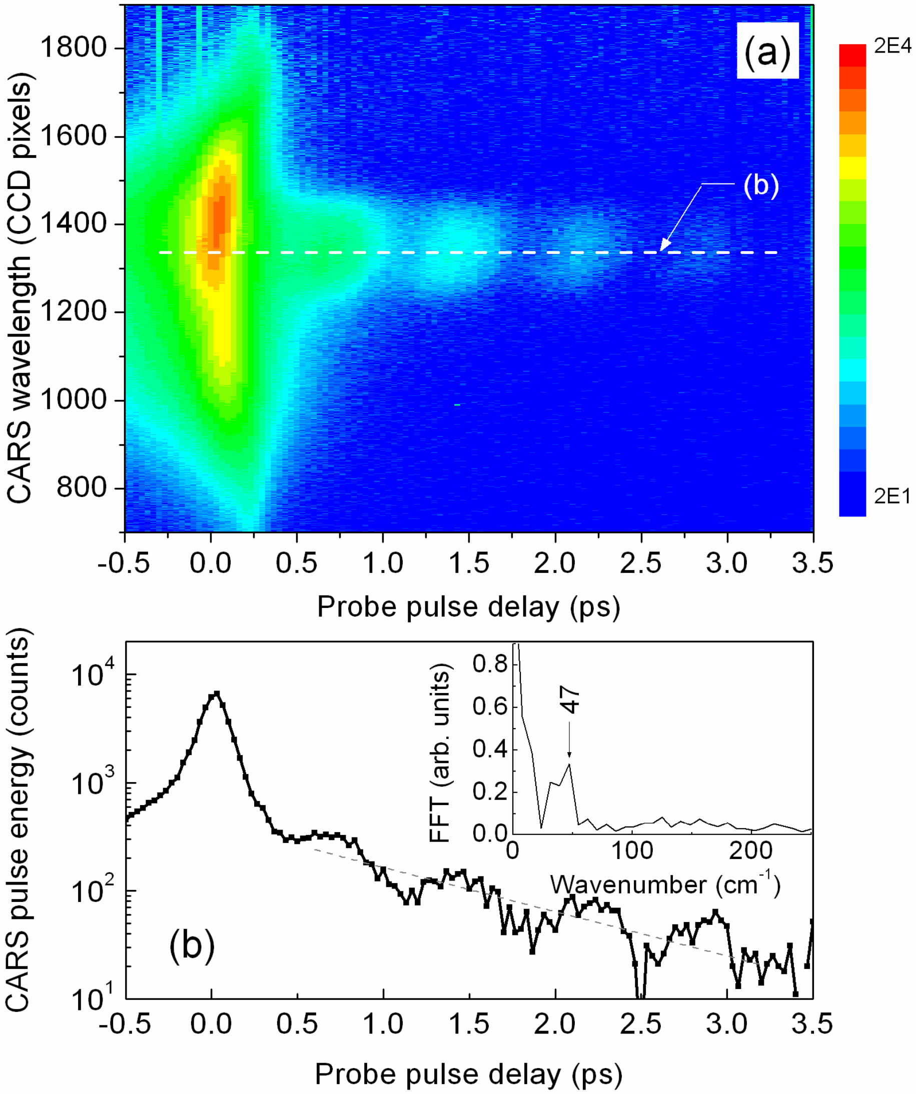

Fig. 4.20. CARS on crystalline NaDPA powder: (a) CARS spectrogram recorded with a layer of crystalline NaDPA powder as a sample. Two Raman modes, 1395 and 1442 cm^{-1}, are excited by a pair of ultrashort pulses; (b) a cross-section of the spectrogram along the probe delay; Inset: Fast-Fourier Transform of the recorded beating, corrected for exponential decay. The three laser beams, focused with a 2-inch lens (f = 20 cm), are overlapped in a BoxCARS geometry. The generated and then scattered signal is collected in the backward direction (slightly off the main axis). Pulse parameters are: pump - λ_1 = 726 nm, 1.8 μJ/pulse; Stokes - λ_2 = 808 nm, 6.0 μJ/pulse; probe - λ_3 = 578 nm, 0.3 μJ/pulse. The spectrograph set wavelength is 520 nm. The acquisition time is 1 s per step (0.5 s for signal, 0.5 s for background).

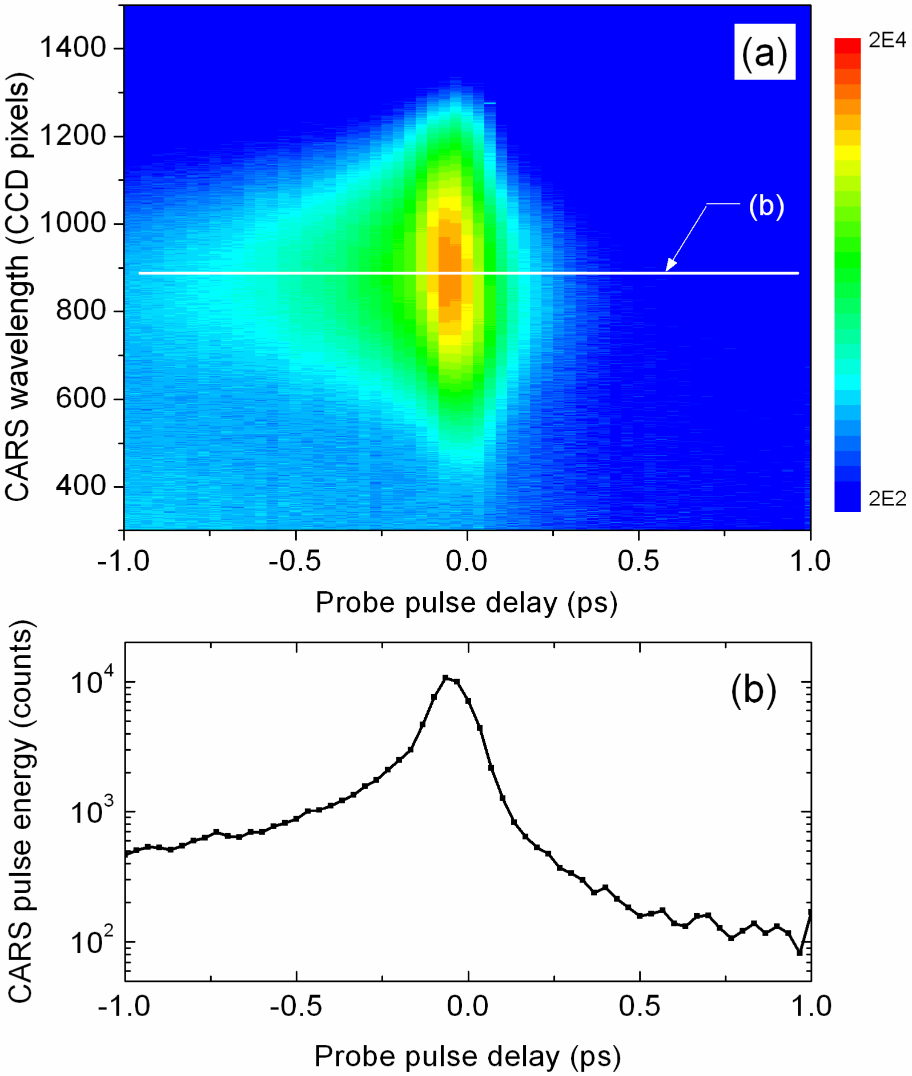

Fig. 4.21. CARS on B. subtilis spores: (a) CARS spectrogram; (b) its cross-section along the probe delay. The experimental conditions are the same as in Fig. 4.19. The frequency difference between the pump and Stokes fields is tuned to 1600 cm^{-1}.

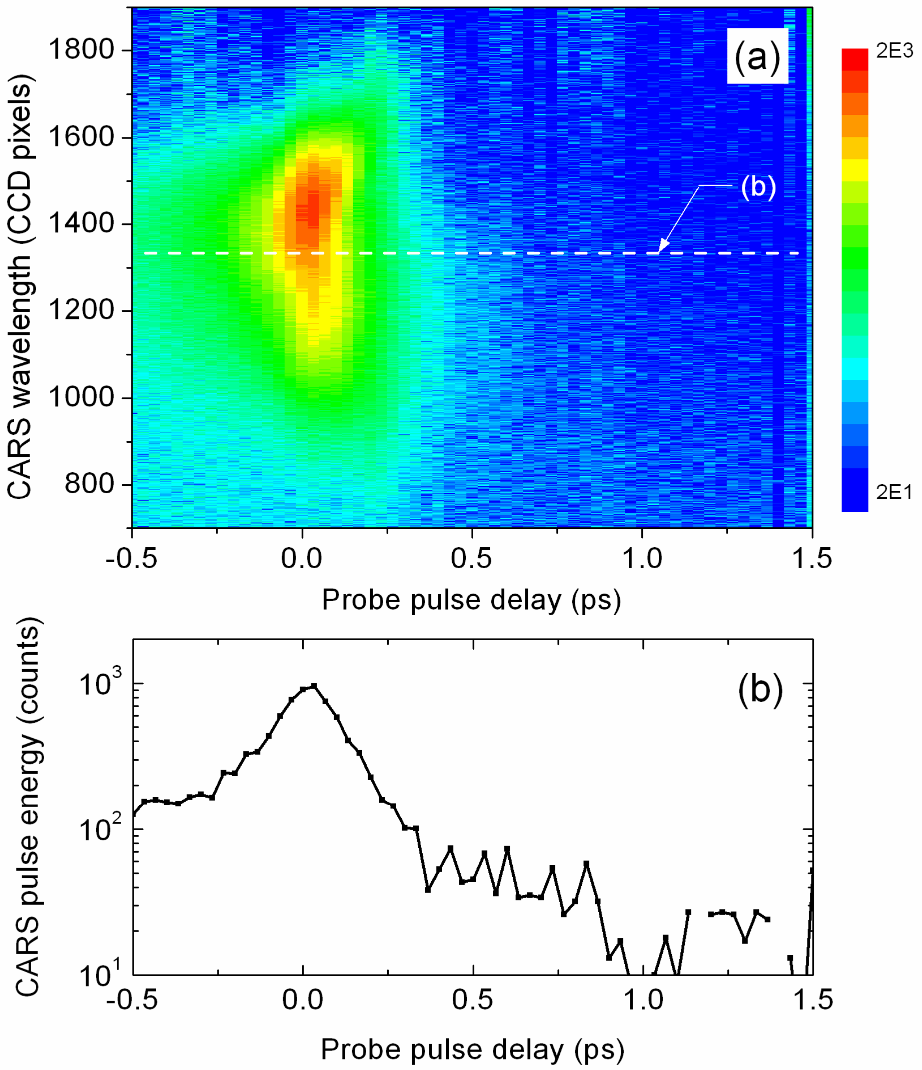

Fig. 4.22. CARS on B. subtilis spores: (a) CARS spectrogram; (b) its cross-section along the probe delay. The experimental conditions are the same as in Fig. 4.20. The frequency difference between the pump and Stokes fields is tuned to 1400 cm^{-1}.

We offer the following reasons for the negative result. Time-resolved CARS scheme relies on monitoring of long-living free-induction decay as opposed to the short-lasting NR FWM, as is the case for powders. The spores, however, exhibit fairly broadened Raman transitions (see Fig. 2.8). In particular, the fingerprint Raman lines (between 1300 and 1700 cm^{-1}) have the line widths on the order of 20-to-30 cm^{-1}, four times of those for the powders. Multiple scattering, on the other hand, traps the incoming pump and Stokes photons inside the sample and generates background NR FWM photons even at large positive probe delays. With a lower number of the target molecules shielded by the outer layers of the spore infrastructure, the weak and rapidly decaying CARS signal now gets buried in the optical noise, while the laser-induced damage of the sample prevents us from compensating these hampering factors by means of longer acquisition times.

The last remedy, even if effective, does not suit well to the main purpose of this study. We, therefore, have approached the problem from a different perspective, outlined in the later chapters (starting with Chapter VI), where (i) extra care is taken to suppress the NR background and associated noise; (ii) time-delayed probing is empowered by the enhanced spectral contrast between the excitation and probing stages enabling a robust and easy-to-interpret frequency-resolved scheme for spore detection.

CHAPTER V

MODE-SELECTIVE ULTRAFAST COHERENT RAMAN SPECTROSCOPY OF HIGHLY SCATTERING SOLIDS[*]

The simplest form of pulse shaping, linear chirp, is utilized here for mode-selective excitation of Raman transitions in the powder of sodium dipicolinate. Probing of the induced molecular vibrations is done by a time-delayed ultrashort pulse, as in time-resolved CARS. However, the preparation pulses are stretched, with matching chirp rates, to attain the spectral width of the pump-Stokes excitation band on the order of the spacing between the Raman lines. Depending on the timing between the pump and Stokes pulses, time-resolved CARS measurements reveal single-mode as well as double-mode free-induction-decay dynamics.

1. Introduction

Recently, a great deal of attention has been drawn to open-loop and adaptive pulse shaping techniques. The inherently large spectral bandwidth of ultrashort pulses has been utilized for various coherent control schemes, where the process outcome is manipulated through constructive and destructive interferences of possible excitation paths. The cancellation of the two-photon absorption [47], the control of branching ratio of chemical reactions [48] or vibrational wave packet dynamics [49, 50] are just a few of the demonstrated effects based on this idea. An important research field relevant to the subject of this chapter is the restoration of the desired spectral selectivity or rather spectral resolution through pulse shaping.

For CARS spectroscopy, where two laser pulses at carrier frequencies ω_1 and ω_2 prepare coherent molecular vibrations and the third pulse (at carrier frequency ω_3) scatters inelastically off them (see Fig. 5.1(a)), the specificity can be gained through the

---

[*] Reprinted with permission from “Pulse shaping for mode-selective ultrafast coherent Raman spectroscopy of highly scattering solids” by D. Pestov *et al.*, 2007, submitted for publication in J. Opt. Soc. Am. B, manuscript #90847.

mode-selective excitation of Raman transitions, i.e. at the preparation stage, as well as through the shaping of the probe pulse. In a series of experiments, Silberberg *et al.* demonstrated the use of periodic modulation [51] and step-like jumps [19, 20, 52] of the pulse phase for this purpose. An attractive alternative is to use linearly chirped pulses [53-57]. This simplest pulse shape is easy to produce and modify. It also comes together with a very intuitive picture of how pulse shaping works.

Here, we utilize a pair of broadband, linearly chirped laser pulses for frequency-resolved excitation of adjacent Raman modes in NaDPA powder [58]. Pulse chirp leads to the effective reduction of its instantaneous bandwidth. Provided that the preparation pulses have the same amount of chirp, as in Fig. 5.1(b), their instantaneous frequency difference can be kept constant over the whole overlap region between the pulses. The excitation bandwidth is then determined by the effective spectral widths of the pump and Stokes pulses. The frequency difference depends on the time delay between the two pulses and can be conveniently adjusted.

Our approach is analogous to those described in [55, 56], but the probing of the induced molecular vibrations differs. We use a third, time-delayed ultrashort pulse to generate the background-free CARS signal. By varying the probe pulse delay, we can observe the free-induction decay or even quantum beats if several Raman transitions are excited [23]. Sweeping the timing between the shaped pump and Stokes pulses, we can directly map out the CARS signal intensity versus the Raman shift.

Note that the pulse configuration used here is conceptually opposite to the discussed later hybrid CARS scheme, where broadband excitation of multiple Raman transitions via a pair of ultrashort transform-limited pulses is combined with their time-delayed but frequency-resolved probing.

2. Materials and Methods

The schematic layout of the setup and the pulse sequence is given in Fig. 5.1(c). The very same Ti:Sapphire-based regenerative amplifier system (Legend, Coherent), evenly pumping two OPAs, is used to produce the synchronized pump (λ_1 = 722.5 nm, $\Delta\nu_1 \equiv \Delta\omega_1/(2\pi c) \approx$ 287 cm^{-1}), Stokes (λ_2 = 804 nm, $\Delta\nu_2$ = 464 cm^{-1}), and probe (λ_3 = 579 nm, $\Delta\nu_3$ = 210 cm^{-1}) laser pulses. The chirping of the pump and Stokes pulses is done by sending the initially transform-limited preparation pulses through a 4-cm slab of SF11 glass. Additionally, the Stokes pulse is guided through a pulse shaper (Silhouette, Coherent). The last is used for fine tuning of the Stokes pulse phase to match its chirp to the chirp of the pump pulse. After the computer-controlled delay stages, the three beams are focused (with 40 to 50 cm focal length lenses) onto a single spot on the surface of the sample, a rotated pellet of NaDPA powder. The scattered CARS signal is collected in the backward direction by a 2-in concave mirror, slightly offset from the main axis. The light is pre-filtered from the dominant pump, Stokes, and probe photons and refocused on the entrance slit of the imaging spectrograph (Chromex-250is) with a LN2-cooled CCD. CARS spectrum is recorded as a function of the probe or pump pulse delay, depending on the experiment.

3. Shaping of the Preparation Pulses

As it was mentioned above, we shape the initially transform-limited pulses by sending them through a slab of SF-11 glass. To the first approximation, the dispersion of the medium produces a linear chirp of the pulses. Note that since the beams are not focused inside the glass, pulse propagation is well described within the linear model, i.e. without taking into account possible pulse reshaping due to the field-induced nonlinearities.

For the sake of simplicity, we assume the input pulses to have a Gaussian temporal profile, i.e.

$$E(t) = E_0 \times \exp[-\Gamma_0 t^2 + i\omega_0 t], \tag{5.1}$$

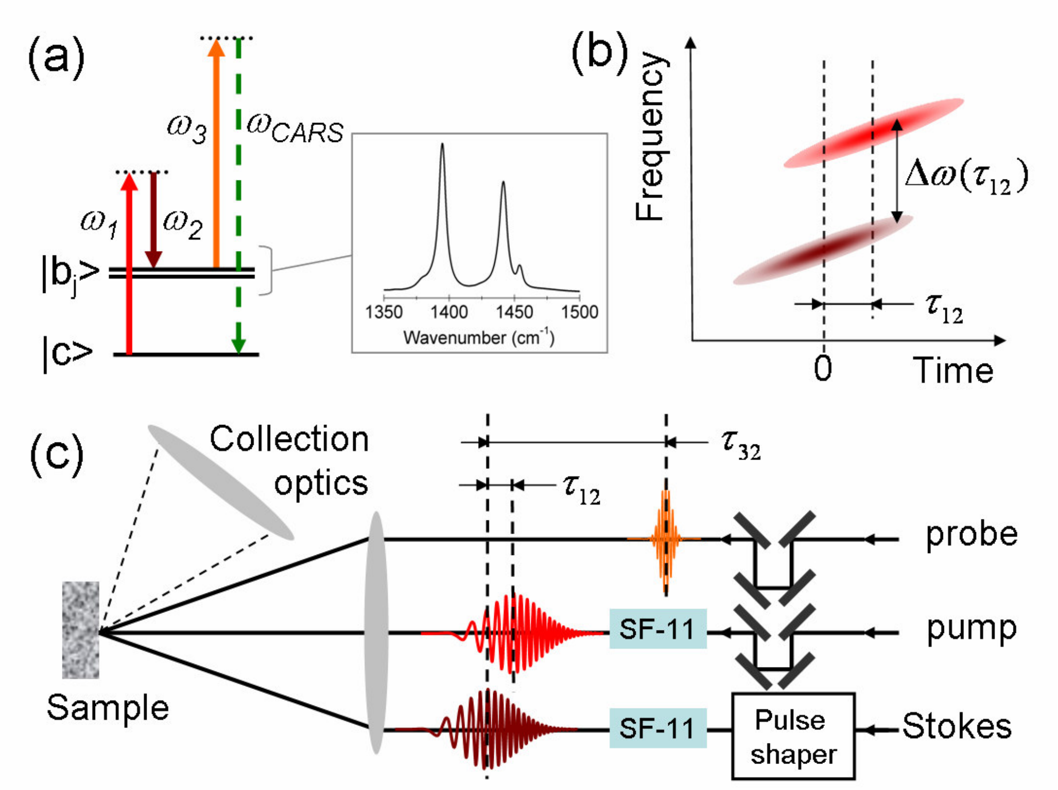

Fig. 5.1. The technique and experiment schematics: (a) CARS energy level diagram. The two broadband but shaped preparation pulses, pump (ω_1) and Stokes (ω_2), excite Raman-active vibrational modes of the sampled molecules. The third pulse (ω_3) probes the initiated coherent molecular vibrations. Inset: spontaneous Raman spectrum of NaDPA powder in the range of interest. (b) Time-frequency diagram of the selective Raman excitation with linearly chirped laser pulses. The difference frequency $\Delta\omega \equiv \omega_1 - \omega_2$ depends on the relative timing τ_{12} between the preparation pulses. (c) Experimental setup layout. The pump and Stokes pulses are sent through 4-cm pieces of SF-11 glass. The Stokes pulse also passes through a commercially available pulse shaper (Silhouette, Coherent), where a parabolic phase mask is added to compensate for the difference in the chirp, produced by the glass slabs. [58]

where E_0 is the complex amplitude of the electric field, ω_0 is the pulse carrier frequency, and $\Gamma_0 \equiv a_0 - ib_0$ is related to the full-width-at-half-maximum (FWHM) duration of the pulse, τ, and its spectral width, $\Delta\omega$. Explicitly, $\tau = \sqrt{2\ln(2)/a_0}$ and $\Delta\omega = 2\sqrt{2\ln(2)a_0(1+b_0^2/a_0^2)}$. If the frequency-dependent wavenumber is approximated by the first three terms of its Taylor series expansion near ω_0, i.e.

$$k(\omega) \equiv \omega n(\omega)/c \approx k(\omega_0) + k'(\omega_0)\times(\omega-\omega_0) + k''(\omega_0)\times(\omega-\omega_0)^2/2, \tag{5.2}$$

the output pulse traveling distance L through the dispersive medium with negligible absorption is given by

$$E(t) = E_0 \times \exp[i\omega_0(t - L/V_\phi(\omega_0)]\times\exp[-\Gamma(L)\times(t - L/V_g(\omega_0))^2], \tag{5.3}$$

where $V_\phi(\omega_0) \equiv \omega_0/k(\omega_0)$ is the phase velocity, and $V_g(\omega_0) \equiv 1/k'(\omega_0)$ is the pulse group velocity [59]. The pulse acquires a linear chirp with

$$\frac{1}{\Gamma(L)} \equiv \frac{1}{a-ib} = \frac{1}{\Gamma_0} + 2ik''(\omega_0)L\,. \tag{5.4}$$

From the measured spectrum of the pump pulse and the known dispersion properties of the glass, we estimate the input pulse duration, τ_1^{in}, to be 51 fs, and the output, after 4 cm of SF11 glass, τ_1^{out} = 0.48 ps. The last number agrees well with the measured FWHM of the cross-correlation profile between the stretched pump and ultrashort transform-limited probe pulses ($2\omega_3 - \omega_1$ process, see Fig. 5.2(a)), which is 0.47 ps. The calculated linear chirp, $2b$, is equal to 0.11 mrad·fs^{-2} (0.58 cm^{-1}·fs^{-1}). It corresponds to $d\lambda_1/dt \approx$-31 nm/ps and results in 14 nm/ps-slope for the recorded cross-correlation spectrogram, since $d\lambda_{FWM}/dt \approx -(\lambda_{FWM}/\lambda_1)^2 d\lambda_1/dt$. The effective bandwidth of the pump pulse is reduced by almost an order of magnitude, $\Delta\nu_1^{eff} \equiv (\tau_1^{in}/\tau_1^{out})\Delta\nu_1 \approx 30$ cm^{-1}.

Because of slightly different dispersion of SF-11 glass at the Stokes wavelength and the different initial bandwidth of the Stokes pulse, its propagation through the same glass thickness does not result in the same chirp. Indeed, the calculations give the linear chirp 0.13 mrad·fs^{-2} (0.70 cm^{-1}·fs^{-1}). To match the chirp of the two preparation pulses,

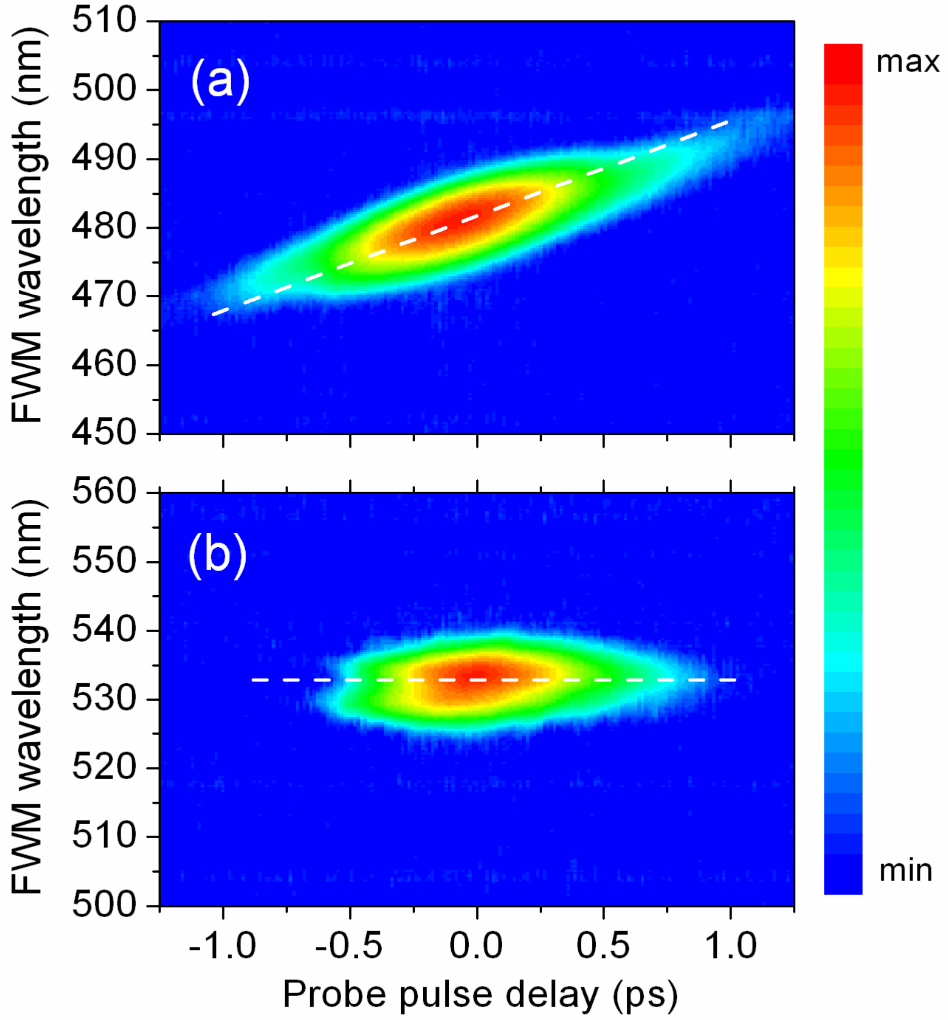

Fig. 5.2. Pulse shaping characterization: (a) Cross-correlation spectrogram between the chirped pump and transform-limited probe pulses. The spectrum of the FWM signal ($2\omega_3 - \omega_1$ process), generated on a cover glass slide, is recorded as a function of the probe pulse delay; (b) Cross-correlation spectrogram between the linearly chirped pump, Stokes, and ultrashort probe pulses. Again, the spectrum of the FWM signal ($\omega_1 - \omega_2 + \omega_3$ process) from a cover glass slide is acquired as a function of the probe pulse delay. [58]

we use the pulse shaper. We first run the MIIPS algorithm [60, 61] to compensate for the distortion due to optical elements other than SF-11 glass (with the slab removed from the beam path), and then put the glass bar back and impose a parabolic phase on top of the found spectral phase compensation mask. This is equivalent to merely changing the length of the glass slab. With a thin microscope slide placed in the focus of the overlapped beams, we monitor the FWM of the pump, Stokes, and probe pulses ($\omega_1 - \omega_2 + \omega_3$ process) as a function of the probe pulse delay to check for the frequency drift in the generated FWM signal (see Fig. 5.2(b)). Obviously, its cancellation is a direct indication that the two pulses have the same chirp.

Note that the spectral bandwidth of the recorded signal is determined by the bandwidth of the probe pulse rather than of the preparation pulses. Assuming perfect match of the pump and Stokes linear chirps, we estimate the output Stokes pulse duration as 0.79 ps and the effective bandwidth $\Delta\nu_2^{eff} \approx 18.5$ cm^{-1}. The resulting spectral bandwidth of the pump-Stokes convolution, responsible for Raman excitation, is therefore $\Delta\nu_{12}^{eff} = \sqrt{(\Delta\nu_1^{eff})^2 + (\Delta\nu_2^{eff})^2} \approx 35$ cm^{-1}, i.e. less than the frequency difference between the two Raman modes of NaDPA powder, 1395 cm^{-1} and 1442 cm^{-1}, shown in the inset of Fig. 5.1(a).

4. Selective Excitation and Background-free Probing

According to the spontaneous Raman spectrum of NaDPA, the vibrational transitions of interest have a wavenumber difference of 47 cm^{-1}, i.e. they are well within the bandwidth of the probe pulse. It makes it difficult to resolve the two Raman transitions by means of a straightforward CARS spectrum acquisition. Fortunately, one can still gain the required resolution through the time-resolved measurements, and there are two complementary ways to do it.

The first one is demonstrated in Fig. 5.3. CARS spectra are recorded as a function of the probe pulse delay for fixed pump-Stokes timing, as it is typically done in time-resolved CARS spectroscopy. The set of spectrograms in Fig. 5.3 shows a gradual change from a single-mode to double-mode excitation, and then back to the single-mode

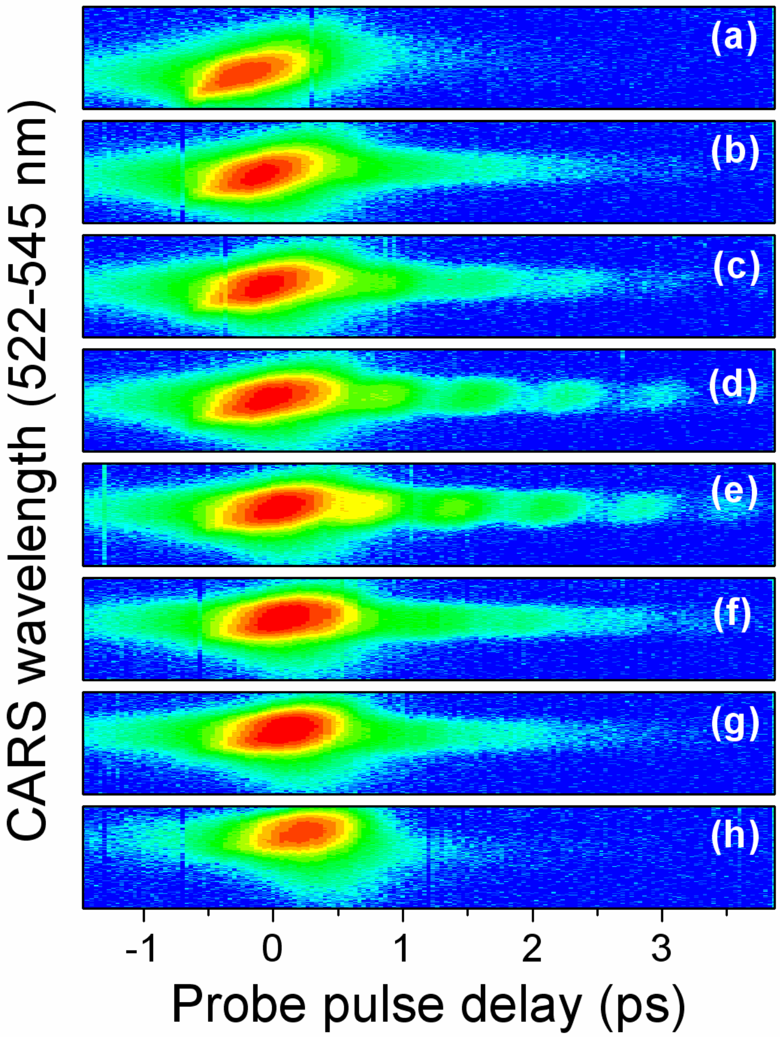

Fig. 5.3. Selective excitation of Raman modes at 1395 and 1442 cm^{-1} in NaDPA powder. The relative timing $\tau_{12} \equiv t_1 - t_2$ between the two linearly chirped preparation pulses, pump (λ_1 = 722.5 nm) and Stokes (λ_2 = 804 nm), is set as: (a) -333 fs, (b) -133 fs, (c) -100 fs, (d) -67 fs, (e) 0 fs, (f) +67 fs, (g) +100 fs, (h) +300 fs. The induced molecular vibrations are probed with an ultrashort pulse at λ_3 = 579 nm. CARS spectrum as a function of the probe pulse delay is recorded. Changing the pump-Stokes timing from (a) to (h), we consecutively excite a single Raman mode at 1442 cm^{-1}; both Raman modes, as it can be inferred from the beating; a single Raman mode at 1395 cm^{-1}. The pump, Stokes, and probe pulse energies are 2.8 μJ, 1.1 μJ, and 0.39 μJ, respectively. The integration time is 0.2 s per step. [58]

dynamics but for the other Raman transition. From the intermediate case, when the beating is observed, the difference frequency can be retrieved (see Fig. 5.4). In particular, we get 46±3 cm^{-1} from the Fast-Fourier Transform (FFT; built-in function of OriginPro 7.5) of the recorded signal, corrected for its exponential decay. The decay times for 1395 cm^{-1} and 1442 cm^{-1} transitions are found to be 0.7±0.1 ps (line width $\Delta\nu$ = 7.6±1.1 cm^{-1}) and 0.8±0.2 ps ($\Delta\nu$ = 6.6±1.6 cm^{-1}), respectively. They are in agreement with the line widths estimated from the spontaneous Raman spectrum of NaDPA powder, 6.7 cm^{-1} and 7.5 cm^{-1}.

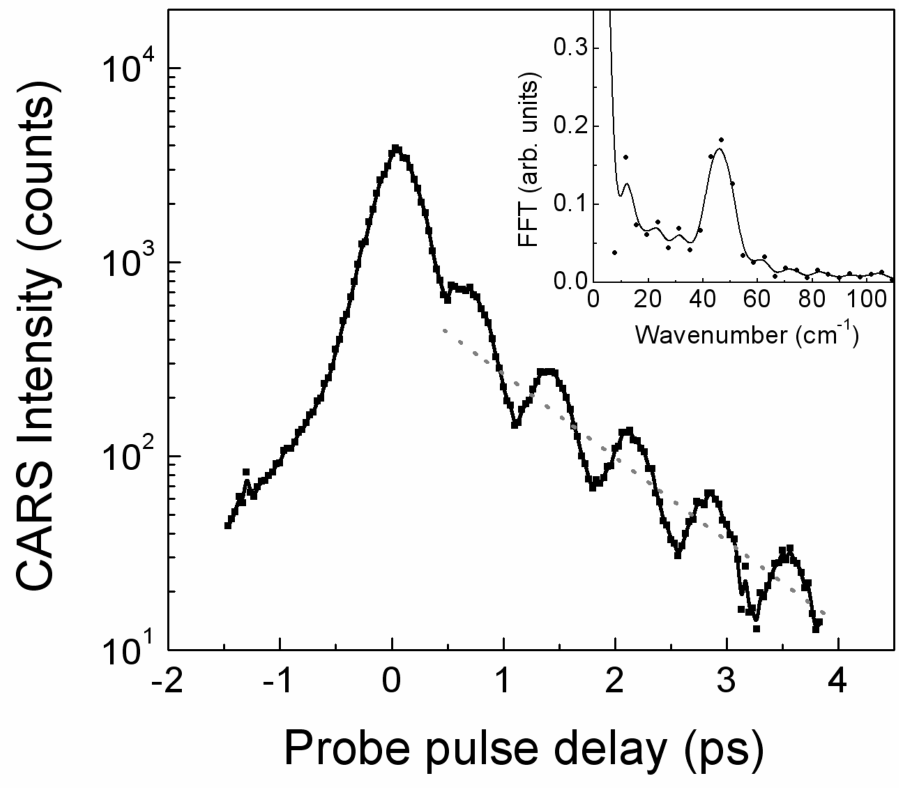

Fig. 5.4. Cross-section of the spectrogram in Fig. 5.3(e) at λ = 535 nm. The beat frequency at positive probe delays corresponds to the frequency difference between the two excited Raman modes, 47 cm^{-1}. Inset: FFT of the recorded modulation, corrected for the exponential decay. [58]

The second approach is to fix the probe pulse timing and record the CARS signal as a function of the pump or Stokes pulse delay. Obviously, it is advantageous to have the probe pulse delayed with respect to the preparation pulses in order to suppress the NR contribution into the generated signal. The resulting profiles of the spectrally integrated CARS signal, when the probe pulse timing corresponds to the quantum-beat peaks, are shown in Fig. 5.5. CARS spectrum (with the spectral resolution of the pump-Stokes pair) is mapped out along the pump pulse timing. From the known pulse chirp, one can determine the frequency difference between the two Raman transitions. We estimate it to be 62±14 cm^{-1}, which is somewhat higher than value derived from spontaneous Raman measurements. The inset in the right top corner of Fig. 5.5 is an example of original CARS spectrograms, before the integration over the spectrum. One can see a slight upward shift of the peak CARS wavelength when the excitation of the 1442-cm^{-1} vibrational mode is superseded by induced molecular vibrations at 1395 cm^{-1}.

5. Conclusions

A combination of the linearly-chirped preparation pulses and time-delayed ultrafast probing conveniently brings together the excitation selectivity and background-free monitoring of the Raman-resonant signatures. The two time scales anticipate the standard time-resolved measurements of the free induction decay as well as the frequency-resolved mapping of the CARS spectrum as a function of the relative pump-Stokes delay. The approach is shown to work even for highly scattering solids, such as powders, where one would expect the pulse phase shaping to be ineffective. At last, the linear chirp is one of the simplest pulse shapes to produce and manipulate, which makes the discussed technique attractive for practical applications.

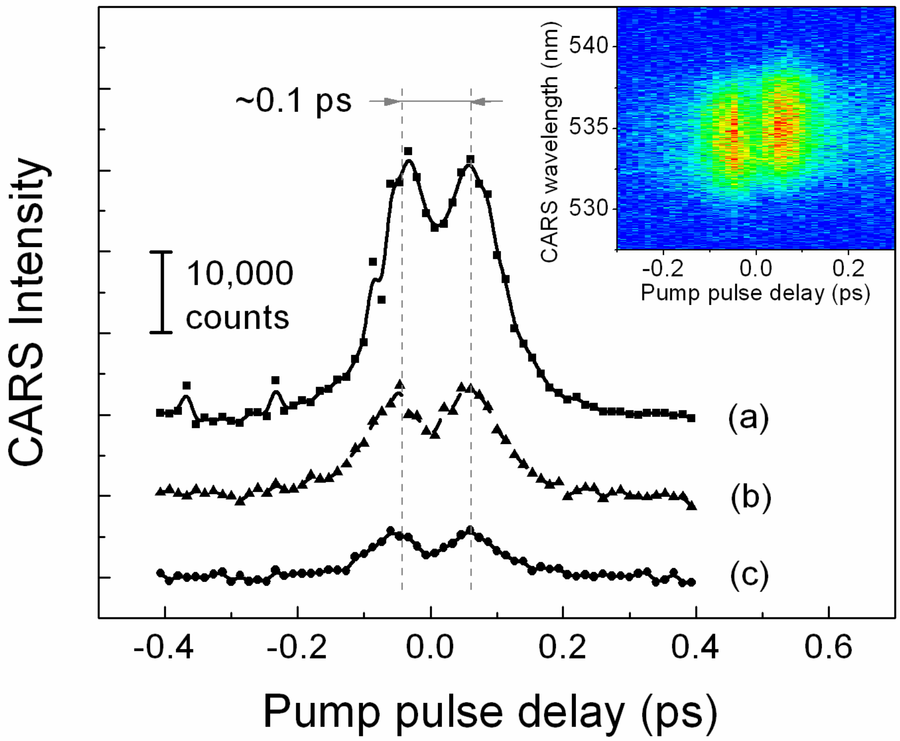

Fig. 5.5. Spectrally-integrated CARS signal as a function of the pump-Stokes pulse timing, τ_{12}. The probe pulse delay is set as (a) 1.4 ps, (b) 2.2 ps, (c) 2.9 ps, i.e. close to the peaks of the quantum beat profile in Fig. 5.4, when the two Raman modes are excited. The pump, Stokes, and probe pulse energies are 3.3 μJ, 1.2 μJ, and 0.37 μJ, respectively. The integration time is 0.2 s per step. Inset: CARS spectrogram recorded in case (b). [58]

CHAPTER VI

HYBRID TECHNIQUE FOR CARS: THEORETICAL STUDY*

Here we discuss the principles that form the foundation of the devised hybrid technique for coherent Raman spectroscopy. We make emphasis on discrimination between the NR FWM and Raman-resonant CARS as well as suppression of the NR background. We also address some peculiar properties of the CARS spectrum as a function of the probe pulse delay when the excited molecular vibrations are probed with a laser pulse with a sinc-squared temporal profile, as it is done in our experiments.

1. Introduction

The overwhelming NR background due to multiple off-resonant vibrational modes and the instantaneous electronic response (see the energy level diagrams in Fig. 1.4) is a major practical constraint on the utilization of CARS as an otherwise powerful spectroscopic tool. Even though there are techniques that make use of the interfering NR FWM to enhance weak CARS signal [18, 21, 62, 63], they are susceptible to depolarization and dephasing because of scattering in realistic samples. The very same arguments works against polarization-sensitive [16] and phase-dependent [19] schemes designed to suppress the NR FWM contribution and associated optical noise.

Broadband Raman excitation of molecular vibrations with consecutive time-delayed narrowband probing, employed in hybrid CARS, is an alternative solution to the indicated problem that seems to withstand the hassles encountered with realistic samples. In this chapter, we review the benefits of such a scheme and indicate the parameters essential for its optimization [64].

---

* Part of the material presented in this chapter is reprinted with permission from “Single-shot Detection of Bacterial Endospores via Coherent Raman Spectroscopy” by D. Pestov *et al.*, 2007, accepted for publication in Proc. Natl. Acad. Sci. U.S.A., manuscript #2007-10427.

2. Theoretical Model and Calculations with Gaussian Pulses

As is well known, the third-order polarization induced by pump, Stokes, and probe pulses naturally splits into two parts, nonresonant and resonant contributions. We find it convenient to adopt the notation of Silberberg *et al.* [65] and write the nonlinear polarization as

$$P^{(3)} = P_{NR}^{(3)}(\omega,\tau) + P_{R}^{(3)}(\omega,\tau) = \int_{0}^{+\infty} (\chi_{NR}^{(3)} + \chi_{R}^{(3)}(\Omega)) E_3(\omega-\Omega,\tau) S_{12}(\Omega) d\Omega, \quad (6.1)$$

where

$$S_{12}(\Omega) \equiv \int_{0}^{+\infty} E_1(\omega'+\Omega) E_2^{*}(\omega') d\omega \quad (6.2)$$

is the convolution of the pump and Stokes spectral amplitudes, $E_1(\omega)$ and $E_2(\omega)$; and $E_3(\omega,\tau)$ is the spectral amplitude of the probe pulse with the explicitly written dependence on its time delay, τ, relative to the preparation pulses. It is assumed that the three pulses are spectrally isolated from each other and only the indicated combination of the fields produces the FWM signal within the frequency domain of interest.

The main difference between the two contributions comes from the fact that the NR nonlinear susceptibility, $\chi_{NR}^{(3)}$, is frequency insensitive and can be treated as a constant, while its counterpart is two-photon resonant and can be modeled as

$$\chi_{R}^{(3)}(\omega_1 - \omega_2) = \sum_{j} \frac{\alpha_j}{\Omega_{Rj} - (\omega_1 - \omega_2) - i\gamma_j}. \quad (6.3)$$

Here the summation is held over all affected Raman transitions; Ω_{Rj} and γ_j denote the vibrational frequency and the Raman line half-width; α_j is a constant related to the spontaneous Raman cross-section; ω_1 and ω_2 are the frequencies of the pump and Stokes laser fields.

For the sake of simplicity, we consider the interplay between the NR and resonant contributions when a single vibrational mode at frequency Ω_R is excited by a pair of ultrashort Gaussian laser pulses centered at ω_{c1} and ω_{c2} for the pump and Stokes fields

$$E_l(\omega_l) = A_l \exp\left(-2\ln(2)\frac{(\omega_l - \omega_{cl})^2}{\Delta\omega_l^2}\right), \quad l = 1,2, \tag{6.4}$$

and probed by a time-delayed Gaussian pulse centered at ω_{c3}

$$E_3(\omega_3, \tau) = A_3 \exp\left(-2\ln(2)\frac{(\omega_3 - \omega_{c3})^2}{\Delta\omega_3^2}\right)\times\exp(i\omega\tau) \tag{6.5}$$

with two adjustable parameters: the spectral full-width-at-half-maximum (FWHM) $\Delta\omega_3$ of the pulse and its time delay τ. Other simplifying assumptions are that $\omega_{c1} - \omega_{c2} = \Omega_R$ and $\omega_{cl} >> \Delta\omega_l$ for $l = 1, 2, 3$, which yields

$$S_{12}(\Omega) = S_0 \exp(-2\ln(2)\cdot(\Omega - \Omega_R)^2 / \Delta\omega_{12}^2) \tag{6.6}$$

with $\Delta\omega_{12} = (\Delta\omega_1^2 + \Delta\omega_2^2)^{1/2}$ and

$$S_0 = \sqrt{\frac{\pi}{2\ln(2)}}\frac{\Delta\omega_1\Delta\omega_2}{\Delta\omega_{12}}A_1 A_2^*. \tag{6.7}$$

From Eq. 6.7, it immediately follows that the excitation within a fixed band of width $\Delta\omega_{12}$ centered at Ω_R is optimal when $\Delta\omega_1 = \Delta\omega_2 = \Delta\omega_{12}/\sqrt{2}$, i.e. two equally-broadband pulses are used. Since the pulses are assumed to be transform-limited, it is equivalent to having the pump and Stokes pulses of the same temporal duration. Note that this is usually not the case for the standard broadband CARS arrangement, where a spectrally narrowband pump pulse is combined with a broadband Stokes-shifted continuum. To give a sensible example, the excitation amplitude $|S_0|^2$ increases by 50 times when a 3-ps pump and 30-fs Stokes pulses are replaced with two 42-fs pulses of the same energy. The width of the excitation band stays the same.

A. Probe Spectral Bandwidth as an Optimization Parameter

We first put the delay time τ equal to zero, i.e. make the preparation and probe pulses overlap in time; and consider the dependence of the nonlinear response of the medium, subject to the broadband excitation by the preparation pulses ($\Delta\omega_{12} >> \gamma$), on the bandwidth of the probe pulse $\Delta\omega_3$. Two quantities, the spectral bandwidth and the peak spectral magnitude of $\left|P_{NR}^{(3)}\right|^2$ and $\left|P_R^{(3)}\right|^2$, are indicative of the observed changes.

Indeed, Fig. 6.1(a) shows the calculated dependence of the FWHM bandwidth for the resonant CARS and NR FWM. As expected, the spectral width of the NR profile is determined by the convolution of all the three laser pulses and therefore has the lower limit of $\Delta\omega_{12}$, which is fixed. On the other hand, the lower limit for the resonant part is dictated by the bandwidth of the Raman line, $\sim 2\gamma$. For $\Delta\omega_{12} >> \gamma$, it is advantageous to use $\Delta\omega_3 << \Delta\omega_{12}$, i.e. narrowband probing, and gain the spectral contrast between the two contributions.

Furthermore, cutting the probe spectrum facilitates substantial reduction of the NR background without appreciable loss in the peak spectral intensity of the CARS signal (see Fig. 6.1(b)). Please to note that the relative position of the two curves along the vertical axis in Fig. 6.1b depends upon the choice of $\chi_{NR}^{(3)}$, the Raman scattering coefficient α (see Eq. 6.2), and the molecular vibration decay rate γ. In particular, they happen to merge in the limit $\Delta\omega_3 << \gamma$ because $\gamma\chi_{NR}^{(3)}/\alpha = 1$ is taken for the calculations.

One can obtain the following analytical expression for the ratio of the two peaks at $\omega = \omega_{c3} + \Omega_R$:

$$\left|\frac{P_R^{(3)}(\omega_{c3}+\Omega_R)}{P_{NR}^{(3)}(\omega_{c3}+\Omega_R)}\right|^2 = \\ = \frac{2\pi\ln(2)}{W^2}\left|\frac{\alpha}{\chi_{NR}^{(3)}}\right|^2 \exp\left(4\ln(2)\frac{\gamma^2}{W^2}\right)\cdot\left(1-erf(\sqrt{2\ln(2)}\frac{\gamma}{W})\right)^2. \tag{6.8}$$

Here $W \equiv \Delta\omega_{12}\Delta\omega_3/(\Delta\omega_{12}^2+\Delta\omega_3^2)^{1/2}$, and $erf(x) \equiv (2/\pi^{1/2})\int_0^x \exp(-t^2)dt$ is the error function. In the limit of a large probe bandwidth, i.e. for $\Delta\omega_3 >> \gamma$ (we also assume $\Delta\omega_{12} >> \gamma$),

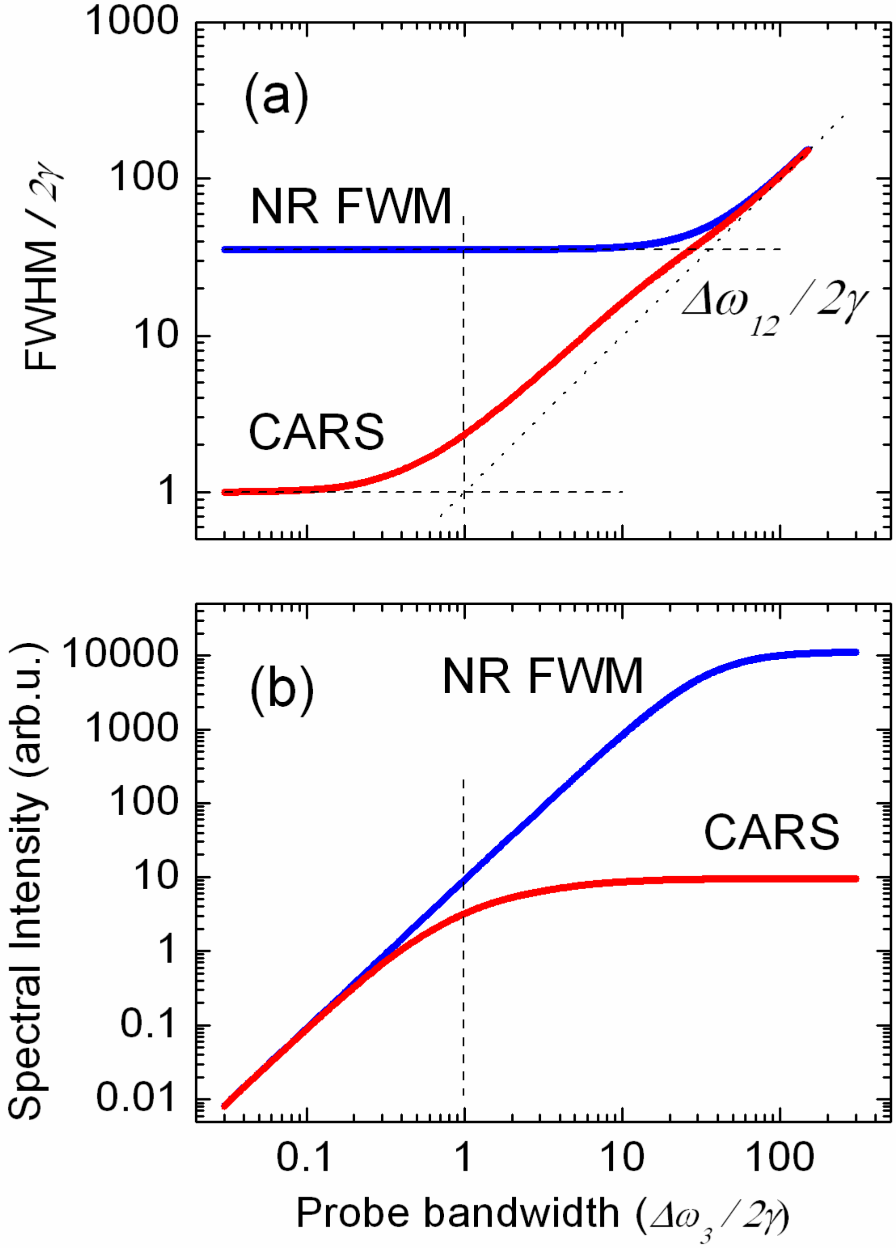

Fig. 6.1. The calculated spectral bandwidth (a) and peak spectral intensity (b) of the resonant (CARS) and nonresonant (NR FWM) contributions into $\left|P^{(3)}\right|^2$, without taking into account the interference term. The parameters used are: $\chi_{NR}^{(3)}=1$, $\alpha=1$, $\gamma=1$, $\Delta\omega_1=\Delta\omega_2=50\gamma$, $\tau=0$, $S_0=1$, and $A_3=1$. [64]

$$\left|\frac{P_R^{(3)}(\omega_{c3}+\Omega_R)}{P_{NR}^{(3)}(\omega_{c3}+\Omega_R)}\right|^2 \approx \frac{2\pi\ln(2)}{W^2}\left|\frac{\alpha}{\chi_{NR}^{(3)}}\right|^2. \tag{6.9}$$

In the opposite limit, i.e. for $\Delta\omega_3 << \gamma$, one gets

$$\left|\frac{P_R^{(3)}(\omega_{c3}+\Omega_R)}{P_{NR}^{(3)}(\omega_{c3}+\Omega_R)}\right|^2 \approx \frac{1}{\gamma^2}\left|\frac{\alpha}{\chi_{NR}^{(3)}}\right|^2. \tag{6.10}$$

Finally, the ratio $\left|P_R^{(3)}/P_{NR}^{(3)}\right|^2$ scales as $\Delta\omega_3^{-2}$ for $\gamma << \Delta\omega_3 << \Delta\omega_{12}$.

From the dependences in Fig. 6.1, we conclude that $\Delta\omega_3 \sim 2\gamma$ provides the best spectral contrast between the two contributions into the nonlinear response as well as suppression of the NR background without noticeable affect on the peak intensity of the resonant signal.

B. Adjusting the Probe Pulse Delay

The other parameter that has been left out of the discussion so far, but can be used to further improve the signal-to-background ratio, is the probe pulse delay. For any fixed value of the probe pulse bandwidth, the NR contribution peaks at zero probe delay and decreases as the overlap between the three pulses is reduced due to the probe pulse timing (see Fig. 6.2(a)). The resonant response, on the other hand, becomes maximal at some positive probe delay and decreases at larger delays with a decay rate determined by the dephasing time of molecular oscillations rather than the profile of the probe pulse (Figs. 6.2(b) and 6.3). When normalized on the probe pulse energy, the resonant contribution reaches maximum for the probe pulse bandwidth $\Delta\omega_3$ on the order of 2γ, and its delay $\sim\Delta\omega_3^{-1}$. The NR FWM peaks at zero probe delay and $\Delta\omega_3 \sim \Delta\omega_{12}$ (which is out of the range plotted in Fig. 6.2(a)).

Simulations presented in Fig. 6.4 summarize the effect of the probe bandwidth and delay on the spectrally resolved profiles of $\left|P_{NR}^{(3)}\right|^2$, $\left|P_R^{(3)}\right|^2$, and $\left|P_{NR}^{(3)}+P_R^{(3)}\right|^2$, where the last one corresponds to what is actually recorded in the experiment. The initially featureless spectrum, dominated by the NR FWM (see Figs. 6.4(a-c)), reveals the

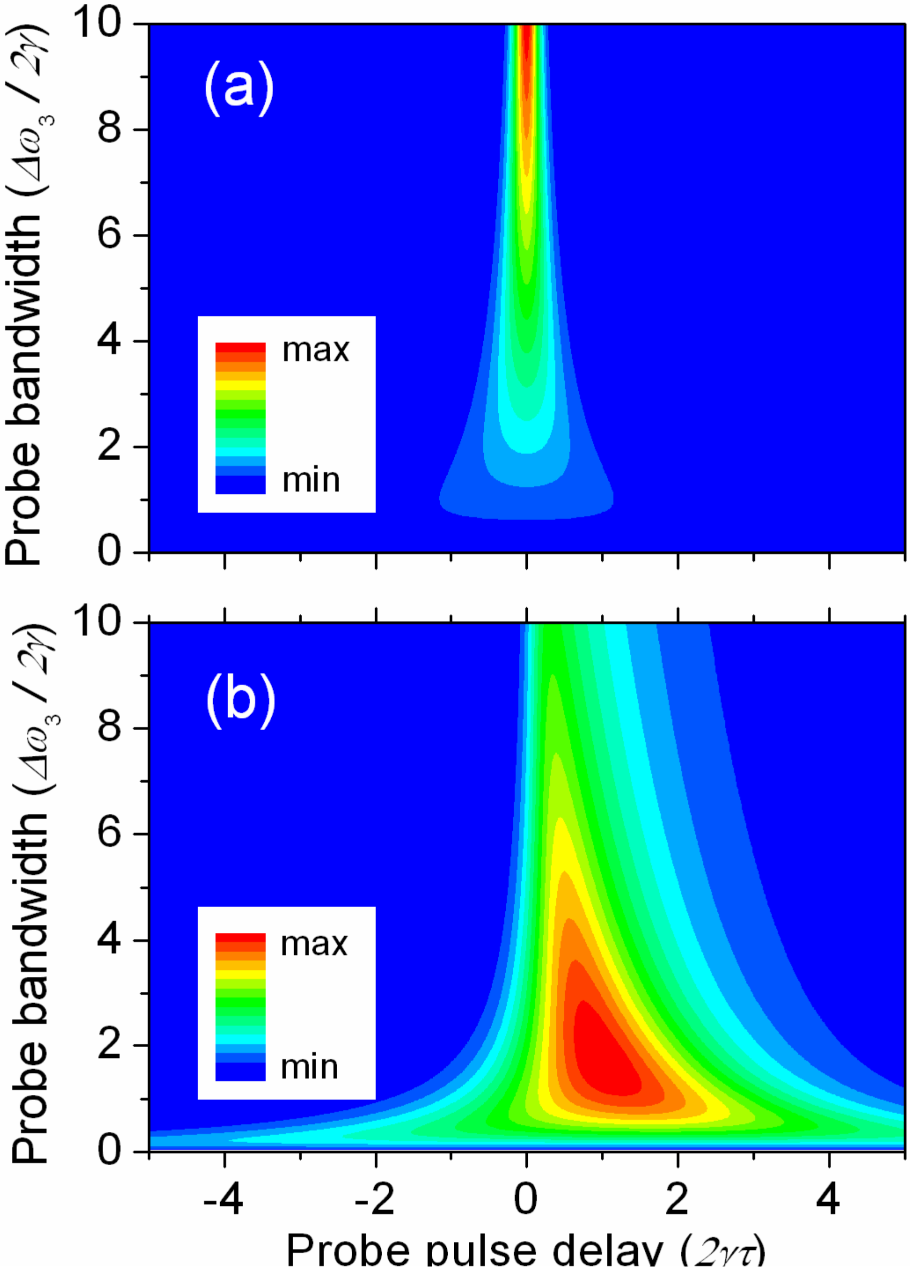

Fig. 6.2. The calculated intensities of $\left|P_{NR}^{(3)}\right|^2$ (a) and $\left|P_{R}^{(3)}\right|^2$ (b) at $\omega = \omega_{c3} + \Omega_R$ as a function of the probe spectral bandwidth $\Delta\omega_3$ and time delay τ relative to the overlapped preparation pulses. The parameters are similar to those used for Fig. 6.1 but τ is varied and the probe pulse amplitude is normalized such that $A_3 = (4\ln(2)/\pi)^{1/4}\Delta\omega_3^{-1/2}$ to have the probe pulse energy constant. [64]

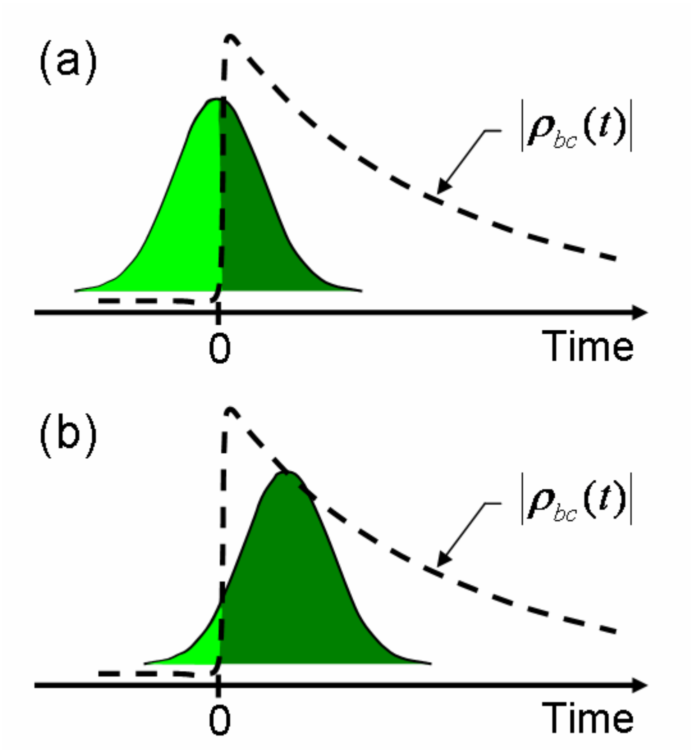

Fig. 6.3. Scattering off the excited molecular vibrations: (a) The spectrally narrowband probe pulse is fully overlapped with the ultrashort preparation pulses (zero probe delay) but only about half of the probe photons scatters off the induced refractive index grating. The first half passes by before the transient grating is formed; (b) The probe pulse is delayed with respect to the preparation pulses to maximize the number of scattered photons. The optimal probe delay depends on the pulse duration and the decoherence time.

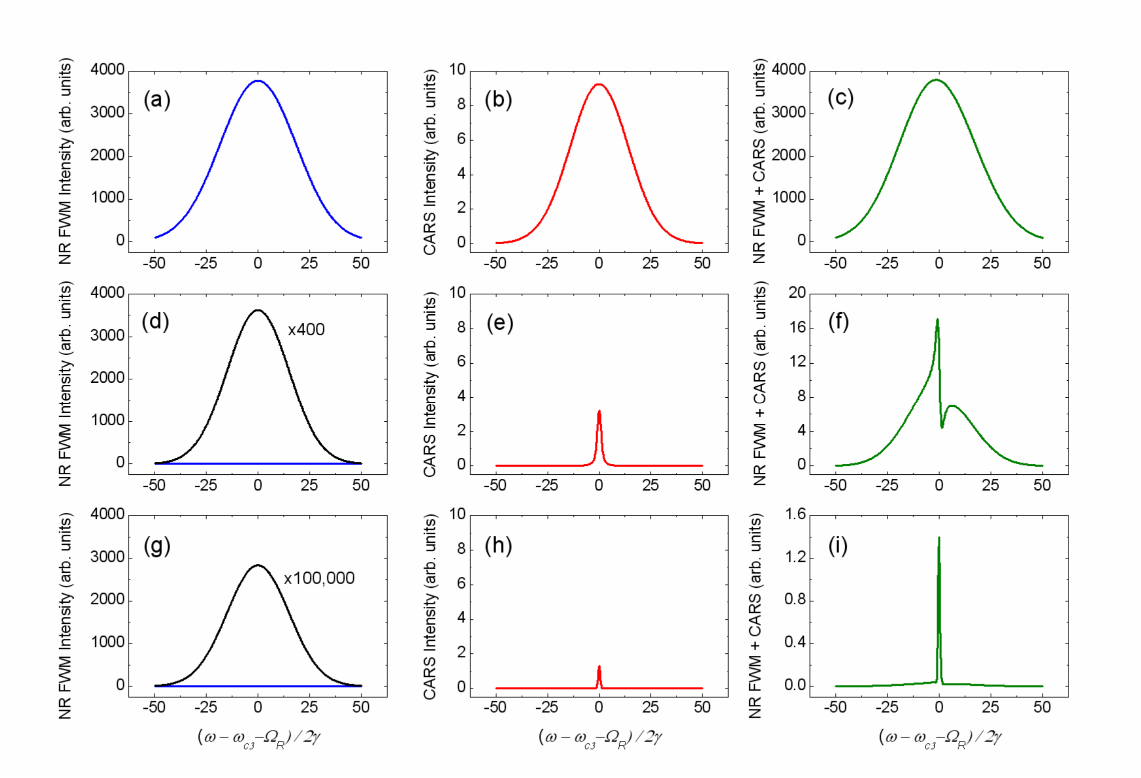

Fig. 6.4. The calculated spectrally resolved profiles of $\left|P_{NR}^{(3)}\right|^2$ (on the left), $\left|P_{R}^{(3)}\right|^2$ (in the middle), and $\left|P_{NR}^{(3)} + P_{R}^{(3)}\right|^2$ (on the right) for: (a-c) $\Delta\omega_3 = 50\gamma$, $\tau = 0$; (d-f) $\Delta\omega_3 = 2\gamma$, $\tau = 0$; and (g-i) $\Delta\omega_3 = 2\gamma$, $\tau = 2/\gamma$. The other parameters are the same as in Fig. 6.1. [64]

presence of Raman-resonant response, distinct from the interfering NR background, when the probe pulse bandwidth is reduced (Figs. 6.4(d-f)); adding probe delay further improves the signal-to-background ratio, as is shown in Figs. 6.4(g-i). The actual optimal values of the probe pulse parameters depend on γ, the ratio $\gamma\chi_{NR}^{(3)}/\alpha$, and the tolerable spectral resolution. The choice of parameter values is also affected by the optical quality of the sample. In particular, strong multiple scattering in spore samples prevents us from complete elimination of the NR FWM. We rather compromise between the spectral signal-to-background contrast and the strength of the acquired resonant signal.

3. Sinc^2-shaped Probe Pulse

It is worthwhile to note that possible probe pulse shapes are not limited to the considered Gaussian waveform. For example, one can use a probe pulse with a sinc$^2(\Delta\omega_3 t/2)$-shaped temporal profile. This pulse shape is of interest to us because it is exactly what one gets by cutting the broadband spectrum, dispersed in the Fourier plane of the 4-f pulse shaper (refer to the setup schematics in Fig. 2.3), with a narrow slit. Putting the preparation pulses on the node of the probe field, as shown in Fig. 6.5, one can virtually cancel out the NR FWM contribution at a finite probe pulse delay. Of course, the timing between the pulses is essential here, therefore in practice, dispersion and multiple scattering inside the sample, if present, fill in the node to some extent.

The spectral amplitude, $E_3(\omega_3,\tau)$, of the shaped probe electric field can be well approximated as

$$E_3(\omega_3,\tau) = A_3\exp(i\omega_3\tau)\times\begin{cases}1 & if \quad \omega_{c3}-\Delta\omega_3/2<\omega_3<\omega_{c3}+\Delta\omega_3/2 \\ 0 & otherwise\end{cases}, \tag{6.11}$$

and used within the same model, described above. In this case, the dependence of the CARS spectrum on the probe pulse delay exhibits rather complex dynamics. Indeed, Fig. 6.6 shows calculated CARS spectrograms for purely resonant response of a medium ($\chi_{NR}^{(3)}=0$) with a single Raman transition. One can see that the expected single resonant peak actually splits and gains modulation while the probe pulse is delayed with respect to the preparation pulses. Please to note that the structure is asymmetric with respect to the zero probe delay. It also looses the symmetry along the frequency axis when the NR response is present ($\chi_{NR}^{(3)} \neq 0$; see Figs. 6.7 and 6.8). This is because of the known π-phase shift when the frequency of the driving force is tuned through the resonance.

Cross-sections of the spectrogram before the first node of the probe pulse give CARS spectra similar to those calculated with a Gaussian probe pulse profile. With the preparation pulses on the node of the probe field (see Fig. 6.8(c)), one gets a single resonant peak, free of the NR background. At larger probe delays, however, the interference pattern exhibits a π-phase shift, which is not present in CARS spectrograms with a Gaussian probe pulse. This is due to the phase jump of the NR contribution, originating from the overlap of the preparation pulses with the probe field at different sides from the node.

Finally, to support the above calculations, we present here an example of experimentally obtained CARS spectrogram on NaDPA powder (the details of the

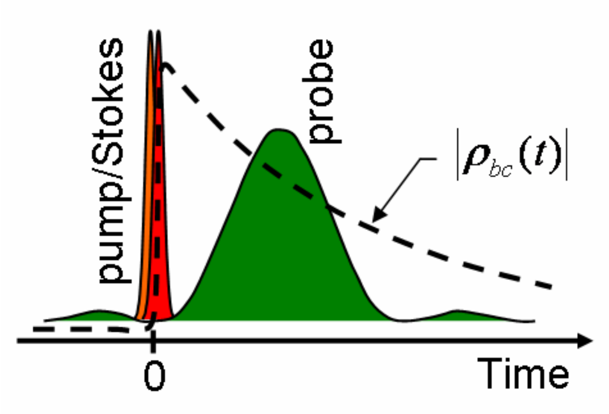

Fig. 6.5. Suppression of NR FWM at finite probe delay by the use of $\mathrm{sinc}^2(\Delta\omega_3 t/2)$ temporal profile. The preparation pulses are put on the first node of the delayed probe field.

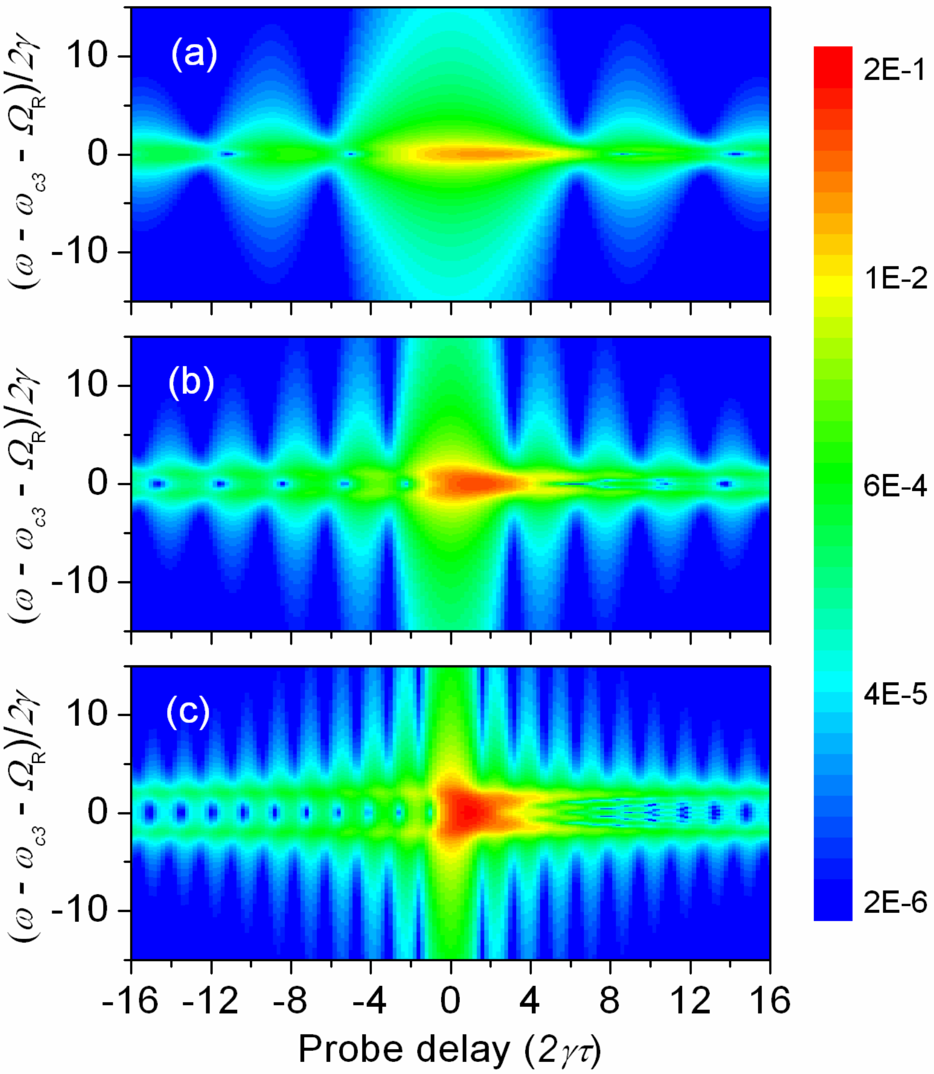

Fig. 6.6. Calculated spectrograms for $\left|P_R^{(3)}\right|^2$ when a probe pulse with sinc-squared temporal profile is used: (a) $\Delta\omega_3 = 2\gamma$, (b) $\Delta\omega_3 = 4\gamma$, (c) $\Delta\omega_3 = 8\gamma$. The other parameters are $\chi_{NR}^{(3)} = 0$, $\alpha = 1$, $\Delta\omega_{12} = 500\gamma$, $S_0 = 1$, and $A_3 = 1$.

experiment are provided in the following chapter), see Fig. 6.9. For all three excited Raman lines, one can see a characteristic splitting at the delay right after the point where the node of the probe field passes the overlapped pump-Stokes pair.

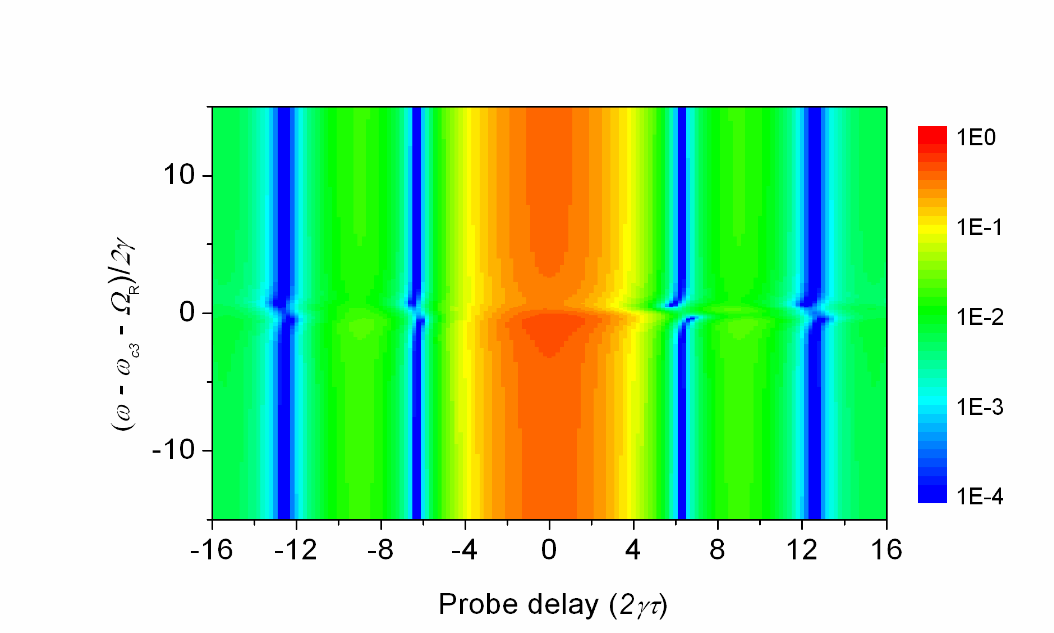

Fig. 6.7. Calculated spectrogram for $\left|P_{NR}^{(3)} + P_{R}^{(3)}\right|^2$ when a probe pulse with sinc-squared temporal profile is used. Here $\Delta\omega_3 = 2\gamma$, $\chi_{NR}^{(3)} = 3$, $\alpha = 1$, $\Delta\omega_{12} = 500\gamma$, $S_0 = 1$, and $A_3 = 1$.

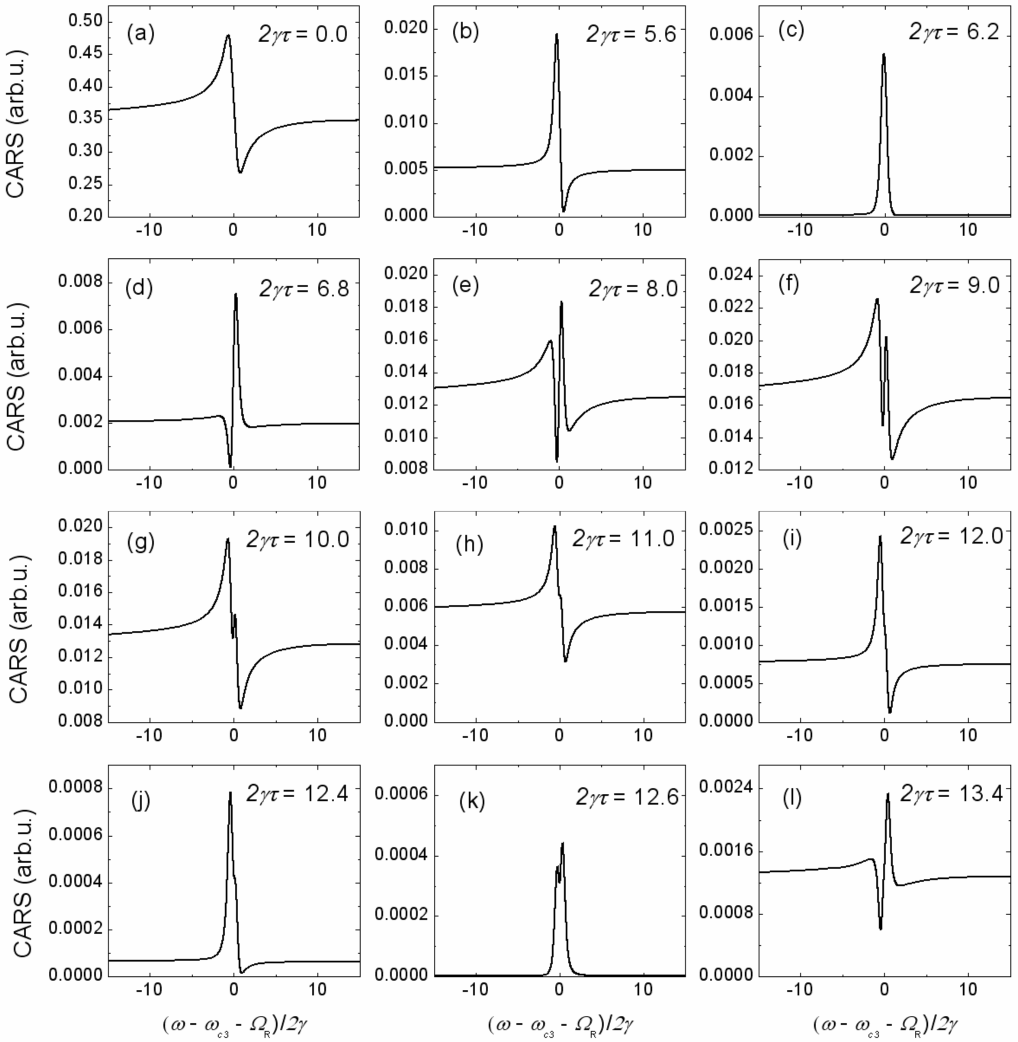

Fig. 6.8. Cross-sections of the spectrogram in Fig. 6.7 for various probe pulse delays.

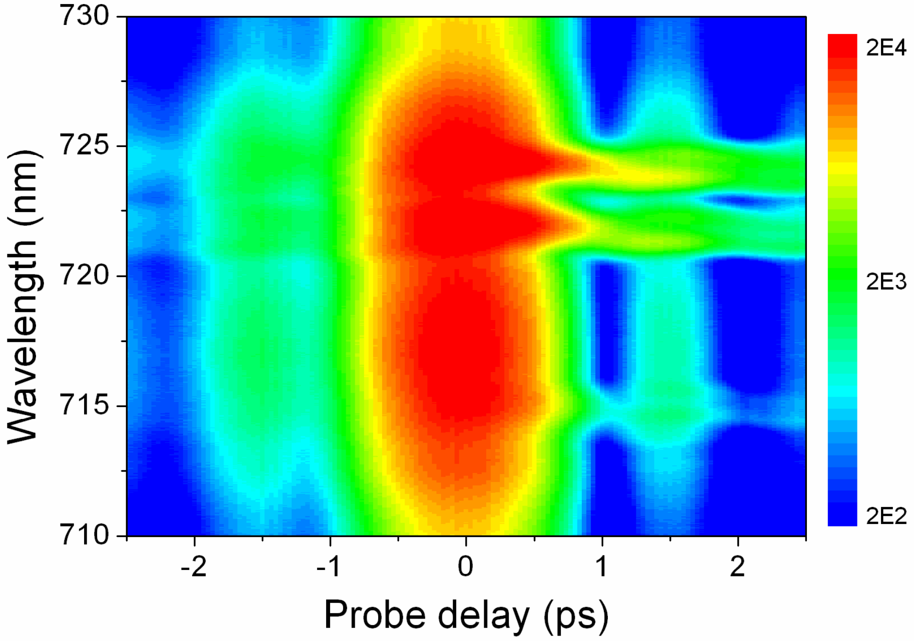

Fig. 6.9. Experimentally obtained CARS spectrogram of NaDPA powder. Pulse parameters are: pump – λ_1 = 1247 nm, 2 μJ/pulse; Stokes – λ_2 = 1537 nm, 2 μJ/pulse; probe – λ_3 = 805.8 nm, 3.2 μJ/pulse.

CHAPTER VII
HYBRID TECHNIQUE FOR CARS:
EXPERIMENTS ON NADPA AND BACTERIAL SPORES[*]

In this chapter, we review a set of hybrid CARS measurements on NaDPA powder (as proof-of-principal) and B. subtilis spores. After the demonstration of the technique capabilities, we follow up with the optimization of the setup parameters to tailor it to the needs of spore detection. We obtain single-shot CARS spectra from about 10^4 spores in the laser focus. Scalability of the demonstrated performance with the power of the input beams is discussed.

1. Introduction

The theoretical analysis, given in the previous chapter, suggests that a combination of broadband preparation and frequency-resolved multi-channel acquisition with time-delayed narrowband probing yields a sensitive and robust technique, which has a great potential for detection applications. We refer to it as hybrid CARS [26] for short but have found that it was also introduced as fs/ps-CARS by Stauffer *et al.*, who used it for coherent Raman measurements on neat solutions of toluene and chloroform as well as rhodamine 6G with an emphasis on prospective monitoring of intramolecular vibrational energy redistribution [27]; another but conceptually similar scheme was also implemented by Hamaguchi *et al.* [66]. By delaying a narrowband pulse relative to dispersion-compensated supercontinuum, they observed NR background-free CARS signal from impulsively excited vibrational modes of indene. Finally, the time-resolved

---

[*] Part of the data reported in this chapter is reprinted with permission from "Optimizing the Laser-Pulse Configuration for Coherent Raman Spectroscopy" by D. Pestov *et al.*, 2007. *Science*, 316, 265-268. Copyright 2007 by American Association for the Advancement of Science (AAAS). Part of the data is reprinted with permission from "Single-shot Detection of Bacterial Endospores via Coherent Raman Spectroscopy" by D. Pestov *et al.*, accepted for publication in Proc. Natl. Acad. Sci. U.S.A., manuscript #2007-10427.

dynamics of the resonant and NR broadband picosecond CARS signals from gas-phase nitrogen was investigated in [67].

From a broader perspective, our approach is a superposition of two well-known techniques developed over the last few decades and employed for combustion diagnostics (see [68-70], and references therein) and chemically selective microscopic biological imaging [71, 72]. In particular, multi-frequency acquisition has been implemented in so-called broadband or multiplex CARS [73-75], where together with the multi-channel detection, a combination of narrowband pump-probe and broadband Stokes pulses is used to address a wide range of vibrational frequencies. In this degenerate scheme, the NR background has been addressed by means of polarization-sensitive and interferometric techniques, rather than timing.

A delayed probe has been used in time-resolved CARS (see previous chapters and [23, 32, 69, 76]). It eliminates the NR contribution by the timing of the probe pulse, but the technique still remains vulnerable to fluctuations. It has been successfully applied to polycrystalline and opaque solids [77] to observe vibrational dephasing of single excited Raman transitions. We have also demonstrated quantum beats between two Raman modes in DPA and NaDPA (Chapters IV, V). However, the use of the multimode interference pattern for species recognition requires the ability to record high-quality quantum beat profiles over a relatively large probe delay span and therefore remains challenging in the presence of scattering and fluctuations.

2. Implementation

The general schematics of the CARS setup is given in Chap. 2. Here we provide some details relevant to this particular experiment. Namely, we employ a Ti:Sapphire regenerative amplifier (Legend, Coherent) with two evenly pumped OPAs (OPerA-VIS/UV and OPerA-SFG/UV, Coherent). The output of the first OPA (λ_1 = 712-742 nm, tunable; $\Delta\nu_1 \equiv \Delta\omega_1/(2\pi c)$ ≈ 230 cm^{-1}) and a small fraction of the amplifier output (λ_2 = 803 nm, $\Delta\nu_2$ ≈ 500 cm^{-1}) are used as pump and Stokes beams, respectively. The output of the second OPA, the probe beam (λ_3 = 578 nm), is sent through a home-made pulse shaper with an adjustable slit (see Fig. 2.3) that cuts the bandwidth of the pulse. As follows, the Stokes and probe pulses pass through delay stages (DS1,2) and then all the three beams are focused by a convex 2-inch lens (with the focal length f = 200 mm) on the rotated sample. The scattered light is collected with a 2-inch achromatic lens (f = 100 mm) and focused onto the entrance slit of the spectrometer (Chromex Spectrograph 250is) with a LN2-cooled CCD (Spec-10, Princeton Instruments) attached.

Please to note that the described scheme naturally bypasses the issue of laser pulse synchronization common to double-laser multiplex CARS setups [78-80], where two different lasers, a femtosecond and picosecond ones, have to be synchronized. The use of a single femtosecond laser system for multiplex CARS was suggested by Knutsen *et al.* [81], who used a regenerative amplifier with one OPA, and introduced a "temporal slit", i.e. strong chirping of the pump/probe pulse, to gain frequency resolution.

We have to sacrifice pulse energy in order to obtain a narrowband probe but this sacrifice has a remedy. The use of thicker nonlinear crystals for the frequency conversion process that produces the probe pulse would result in a narrower probe spectrum to start with and therefore higher throughput for the pulse shaper. Note that the second OPA can, in principal, be replaced with a second harmonic crystal, placed in the fundamental beam. One can also use other wavelengths simultaneously generated in the first OPA, and therefore, simplify the setup.

3. First Results on NaDPA Powder and B. Subtilis Spores

The CARS traces taken on NaDPA powder for different pump wavelengths are shown in Fig. 7.1. Streak-like horizontal lines are the signature of excited NaDPA Raman transitions while the broadband pedestal is the NR background. As expected, the tuning of the pump wavelength spectrally shifts the NR background leaving the position of the resonant lines untouched. Note also that the two contributions exhibit different dependence on the probe delay. The magnitude of the NR background is determined by the overlap of the three laser pulses and therefore follows the probe pulse profile.

Relatively long decay time of the Raman transitions under consideration favors their long-lasting presence and makes them stand out when the probe is delayed.

The cross-sections of the spectrograms at two different probe delays are given in Fig. 7.2. One can see that when all the three pulses are overlapped, the resonant contribution is severely distorted by the interference with the NR background. Delaying the probe by 1.5 ps, which is close to the node of the probe pulse, improves the signal-to-background ratio by at least an order of magnitude. We infer that the limitation is

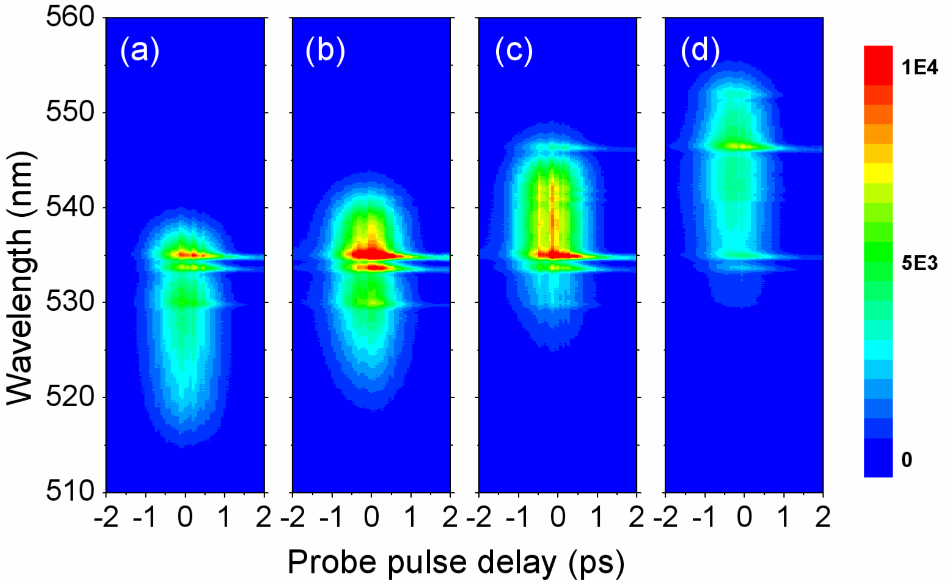

Fig. 7.1. The CARS spectrograms recorded on NaDPA powder for different pump wavelengths, i.e CARS spectrum as a function of the probe pulse delay for λ_1 equal to: (a) 712 nm, (b) 722 nm, (c) 732 nm, (d) 742 nm. The other parameters are: pump – FWHM ≈ 12 nm (corresponds to $\Delta\nu_1 \approx 230$ cm^{-1}), 2 μJ/pulse; Stokes – $\lambda_2 = 803$ nm, FWHM ≈ 32 nm ($\Delta\nu_2 \approx 500$ cm^{-1}), 3.9 μJ/pulse; probe – $\lambda_3 = 577.9$ nm, FWHM ≈ 0.7 nm ($\Delta\nu_3 \approx 21$ cm^{-1}), 0.5 μJ/pulse; Integration time is 1 s per probe delay step (0.5 s for the signal and 0.5 s for the background acquired for the Stokes pulse delayed). [26]

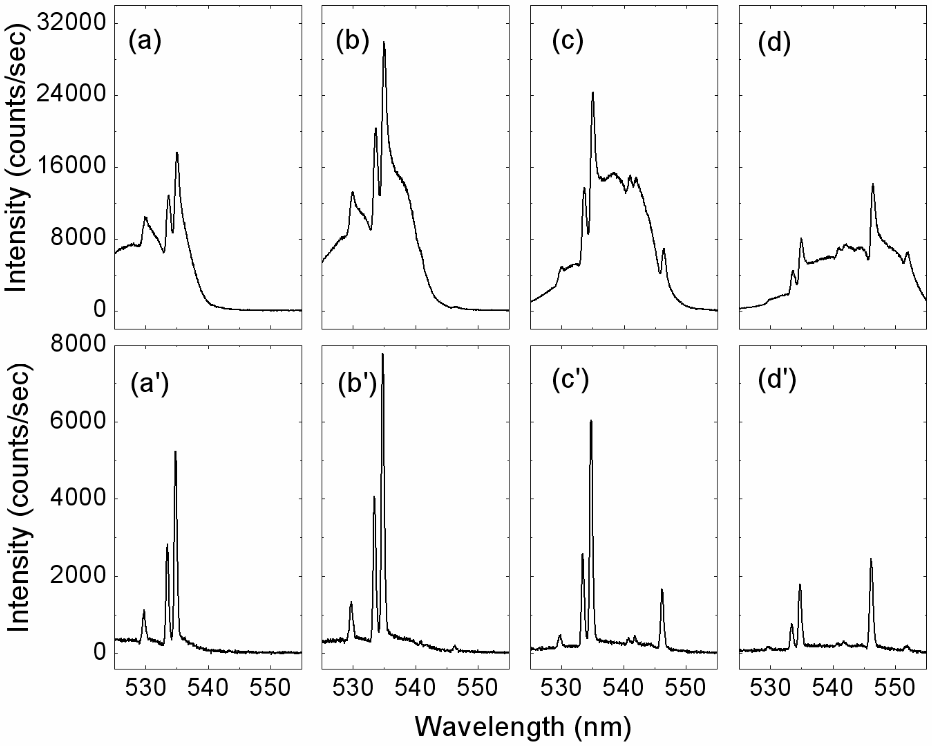

Fig. 7.2. Cross-sections of the CARS spectrograms from Fig. 7.1 for two probe delays, 0 ps (a-d) and 1.5 ps (a′-d′). The corresponding absolute frequencies of the Raman transitions in NaDPA, observed in the CARS experiment and spontaneous Raman measurements, are summarized in Table 7.1. [26]

Table 7.1. The observed Raman peaks and their calculated absolute frequencies for NaDPA and B. subtilis spores. The third column for each of the subsets lists the frequency values from spontaneous Raman measurements. [26]

NaDPA powder			B. subtilis spores		
Peak (nm)	CARS Raman shift (cm^{-1})	Spontaneous Raman shift [*] (cm^{-1})	Peak (nm)	CARS Raman shift (cm^{-1})	Spontaneous Raman shift (cm^{-1})
			527.8	1643	1655[†], 1624[‡]
529.7	1575	1572	529.9	1568	1572[†], 1581[‡]
			531.2	1524	1539[‡]
533.5	1440	1442	533.6	1437	1445[†], 1447[‡]
534.8	1395	1395	535.2	1381	1395[†], 1396[‡]
			537.3	1308	1280[‡]
			539.3	1239	1245[†]
540.8	1187	1189	540.7	1191	1192[‡]
541.8	1153	1152, 1157			
543.9	1082	1087	543.9	1082	
546.2	1004	1007	546.4	998	1001[†], 1013[†] 981[‡], 1018[‡]
551.9	815	817, 827	551.8	819	822[†]

[*] From spontaneous Raman measurement on DPA powder, Fig. 2.6;

[†] Data from Esposito *et al.*, Appl. Spectroscopy **57**, 868 (2003);

[‡] Data from Nelson *et al.*, Appl. Spectroscopy **58**, 1408 (2004).

imposed by multiple scattering. The absolute frequencies of the observed Raman transitions calculated from the retrieved peak positions and the probe wavelength are summarized in Table 7.1. Comparison with the data from spontaneous Raman measurements shows a remarkably good match.

CARS spectra obtained on B. subtilis spores are shown in Fig. 7.3. Zero probe delay is used for these measurements but the data are processed to retrieve the resonant contribution into the acquired signal (for details on the retrieval procedure, see Fig. 7.4). Extracted CARS profiles are summarized in Fig. 7.5. Note that the Raman peaks are not normalized on the strength of the excitation and therefore have an imprint of the pump-Stokes spectral convolution function, which sweeps through the Raman band from 800 cm^{-1} to 1700 cm^{-1} while the pump wavelength is tuned. We assign the Raman transitions in the band (see Table 7.1). Their absolute frequencies are calculated based on the relative shift from the measured probe wavelength. Within our experimental uncertainty of 15 cm^{-1}, the values are in good agreement with the results of spontaneous Raman measurements [7, 82]. The retrieved CARS profiles provide even more details than the spectra obtained recently via multiplex CARS on a water suspension of B. subtilis in a forward configuration [83].

The data shown in Fig. 7.3 are acquired over two minutes, although the strong Raman lines stand out from the background even after seconds of integration. For example, for the two prominent Raman transitions near 1400 cm^{-1}, accumulation over 10 seconds (data are not shown) gives the signal-to-noise ratio 5:1 or better. We conclude that for the setup at hand, the detection speed of major Raman lines of B. subtilis in the fingerprint region is on the order of a few seconds.

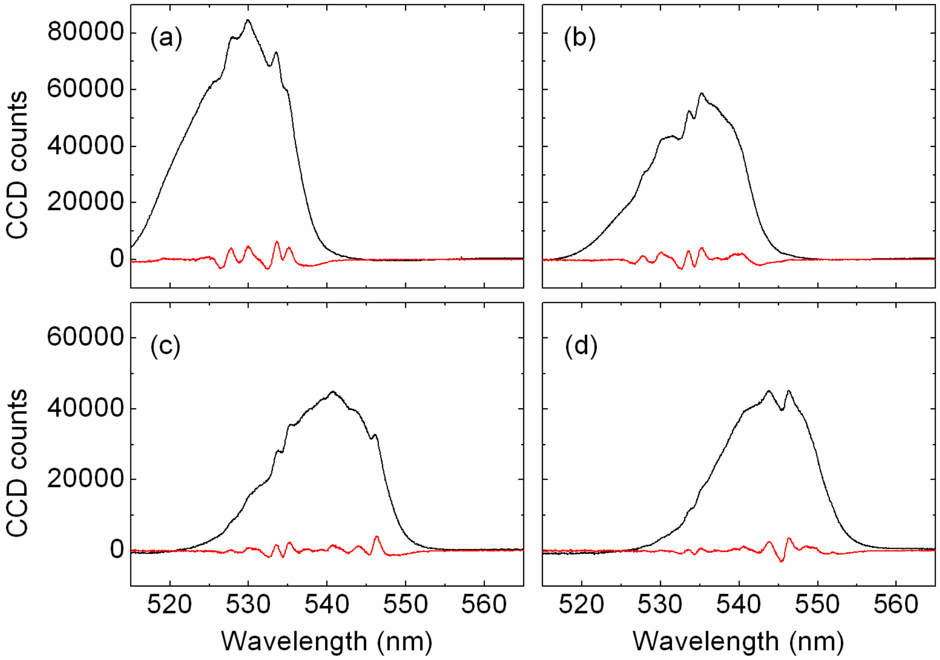

Fig. 7.3. CARS on B. subtilis spores. The probe pulse delay is fixed at zero, the pump central wavelength, λ_1, is tuned: (a) 712 nm, (b) 722 nm, (c) 732 nm, (d) 742 nm. The black curves are the acquired CARS spectra. Red curves are the resonant contribution, retrieved by fitting the NR background with a smooth curve and subtracting it from the total acquired signal. The sample is a pellet of spores fixed in a rotating sample holder. Other parameters are same as for Fig. 7.1. Integration time is 2 min (1 min for the signal and 1 min for the background acquired for the Stokes pulse delayed).

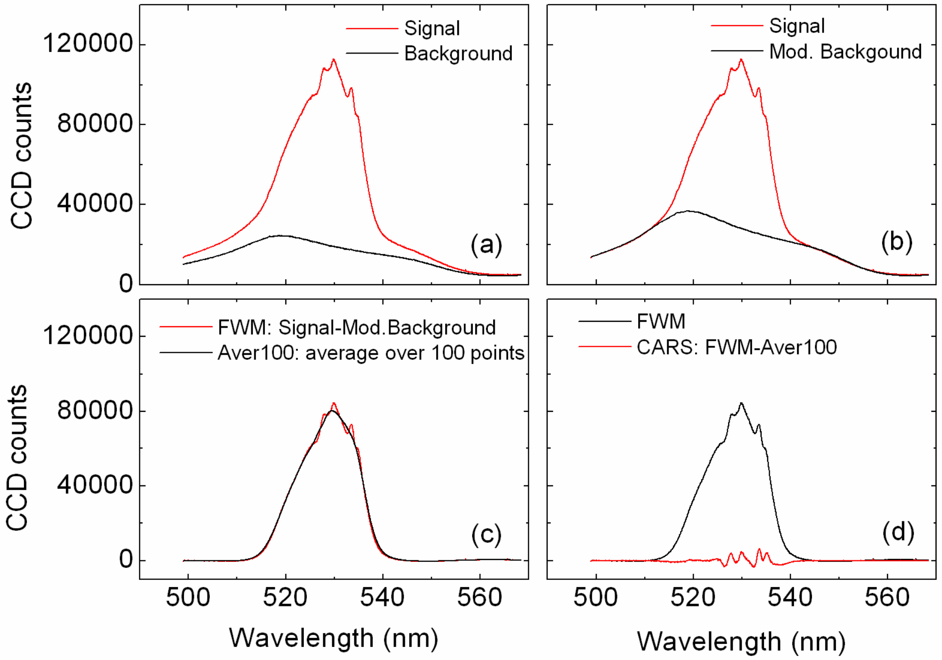

Fig. 7.4. Spore data processing: (a) Acquire the spectrum of the scattered light for zero delay between pump and Stokes pulses (Signal) and nonzero delay between the two (Background). The probe pulse delay is fixed at zero. (b) Smooth the background curve (over 10 adjacent points) and adjust it by linear transformations, vertical shift and stretch, to match the Signal curve on the limits of the range, where no FWM signal is expected (Mod. Background). (c) Subtract Mod. Background curve from Signal curve to obtain FWM, resonant and nonresonant, contribution. Smooth the obtained profile (over 100 adjacent points) to get Aver100 curve. (d) Subtract Aver100 from FWM curve to retrieve CARS contribution.

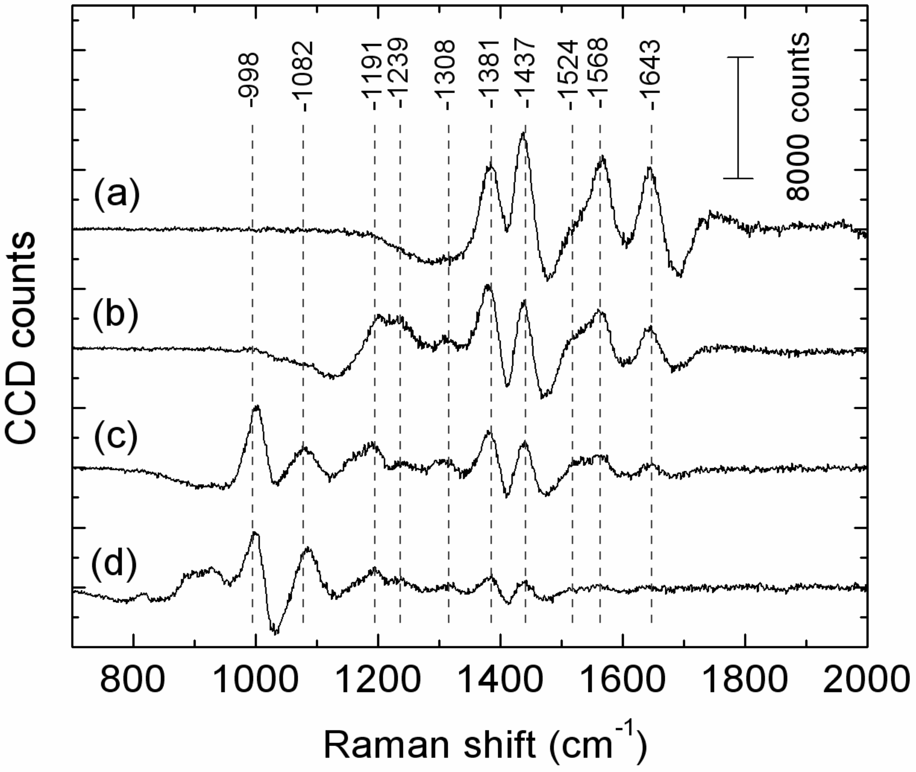

Fig. 7.5. Resonant contributions into CARS spectra of B. subtilis spores, acquired for different settings of the pump central wavelength λ_1: (a) 712 nm, (b) 722 nm, (c) 732 nm, (d) 742 nm. The experimental parameters are the same as in Fig. 7.2. The wavelengths within the observed range are transferred into the Raman shift (by absolute value) relative to the probe central frequency. The comparison between the retrieved Raman frequencies and those available from spontaneous Raman measurements is given in Table 7.1. [26]

4. Optimization of the Detection Scheme

We now turn to optimization of the described scheme, with a goal to minimize the acquisition time required to obtain a distinct CARS spectrum for spores. We make two essential improvements. First, the wavelengths of the pump, Stokes, and probe beams are shifted into the near-IR domain, where the laser-induced damage threshold for the spores is higher as compared to the visible-range wavelengths. Second, the bandwidth and delay of the probe pulse are carefully optimized. These steps have led to 10^2-10^3 increase in the sensitivity of our CARS setup, and enabled us to acquire the spectrum from a small sample volume (~10^4 spores) in a single laser shot. The details follow (see also [64]).

As opposed to the previous setup, we use Signal beams at two different wavelengths, generated in the OPAs by the down-conversion of 805-nm photons, to provide pump ($\lambda_1 \approx 1.25$ μm) and Stokes ($\lambda_2 \approx 1.55$ μm) pulses. The probe pulses come from the residual 805-nm beam spectrally filtered and shaped by a 4-f pulseshaper with a mechanical slit in its Fourier plane. The three beams are still arranged in folded-BOXCAR geometry but focused on the sample by separate lenses. The FWHM diameters for the pump, Stokes, and probe beams on the sample are 36 μm, 43 μm, and 32 μm, respectively (from knife-edge measurements). The described arrangement makes possible to increase the energy of the pulses and their peak intensities by 3-5 times without destroying the spores.

The next step toward superior sensitivity is the optimization of the spectral bandwidth and the time delay of the probe pulse. Since the observed NR background in the recorded CARS spectra is dominated by the multiple scattering within the sample, this is done experimentally. A set of spectrograms, shown in Fig. 7.6 (left), has been recorded for different spectral bandwidths of the probe pulse. For each probe delay in a spectrogram, the acquired spectrum has been processed to remove the NR background and account for the pump-Stokes excitation profile. The resulting normalized spectrograms (see Fig. 7.6 (right)) reveal the sharp features on top of the smooth NR background as well as the optimal probe delay τ_{opt}, corresponding to the maximal ratio

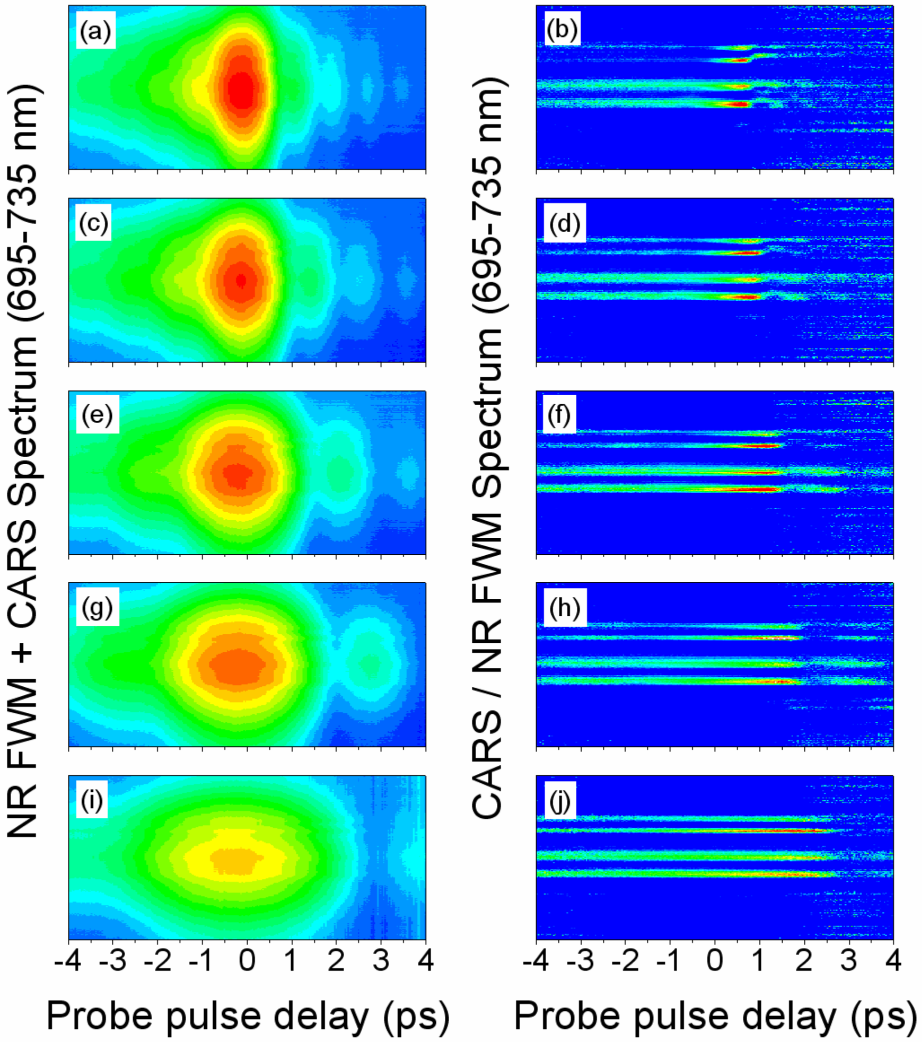

Fig. 7.6. The experimentally obtained CARS spectrograms (left) and processed CARS-versus-FWM profiles (right) acquired with a pellet of B. subtilis spores for different FWHM spectral bandwidths of the probe pulse $\Delta\nu_3 \equiv \Delta\omega_3/(2\pi c)$: (a,b) 40 cm^{-1}, (c,d) 30 cm^{-1}, (e,f) 20 cm^{-1}, (g,h) 15 cm^{-1}, and (i,j) 10 cm^{-1}. The integration time is 1 s. The central wavelengths of the pump, Stokes, and probe pulses are 1.28 μm, 1.62 μm, and 805 nm, respectively. The energy of the probe pulse is kept constant while the spectral bandwidth is adjusted. [64]

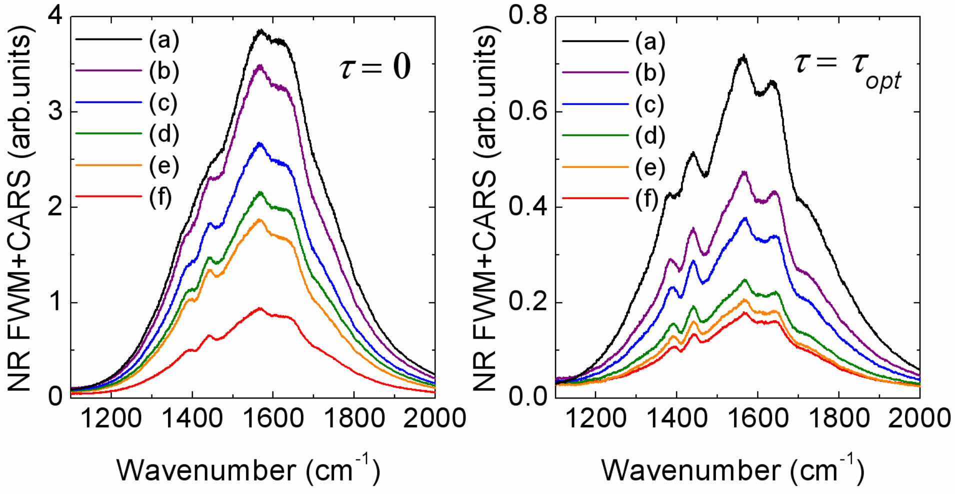

Fig. 7.7. Cross-sections of the recorded CARS spectrograms, similar to those in Fig. 7.5, for two different probe delays: zero delay (on the left) and optimal delay (on the right). The last one is adjusted for different values of $\Delta\nu_3$: (a) 60 cm^{-1}, (b) 40 cm^{-1}, (c) 30 cm^{-1}, (d) 20 cm^{-1}, (e) 15 cm^{-1}, (f) 10 cm^{-1}. [64]

between CARS and NR FWM, for every chosen value of $\Delta\nu_3$. Fig. 7.7 illustrates the recorded, flat-field corrected CARS spectra at $\tau = 0$ and $\tau = \tau_{opt}$.[*] As expected, two tendencies can be observed. If the probe bandwidth is small compared to the Raman linewidth, the visibility of the Raman peak is only weakly dependent of the probe delay, and the signal magnitude is low. If the probe bandwidth is large, the signal is stronger but the contrast degrades. For the observed Raman transitions, $\Delta\nu_3 \approx 30$ cm^{-1} and the time delay $\tau \approx 1.3$ ps are found to be optimal, see Figs. 7.6(c,d) and 7.7(c).

5. Single-shot Detection of Bacterial Endospores

Once we have the parameters optimized, the setup performance is evaluated by decreasing the acquisition time. Fig. 7.8 shows CARS spectra of B. subtilis spores taken

---

[*] The etaloning effect, common for back-illuminated CCDs in the spectral range of interest, leads to inhomogeneous optical response of the CCD over its surface. It results in parasitic amplitude modulation of recorded spectra. To correct for ghost spectral peaks, we acquired a sample spectrum with the probe beam blocked (high-harmonic generation due to the pump and Stokes fields contributed as a smooth background), and then divided all CARS spectra by the obtained profile.

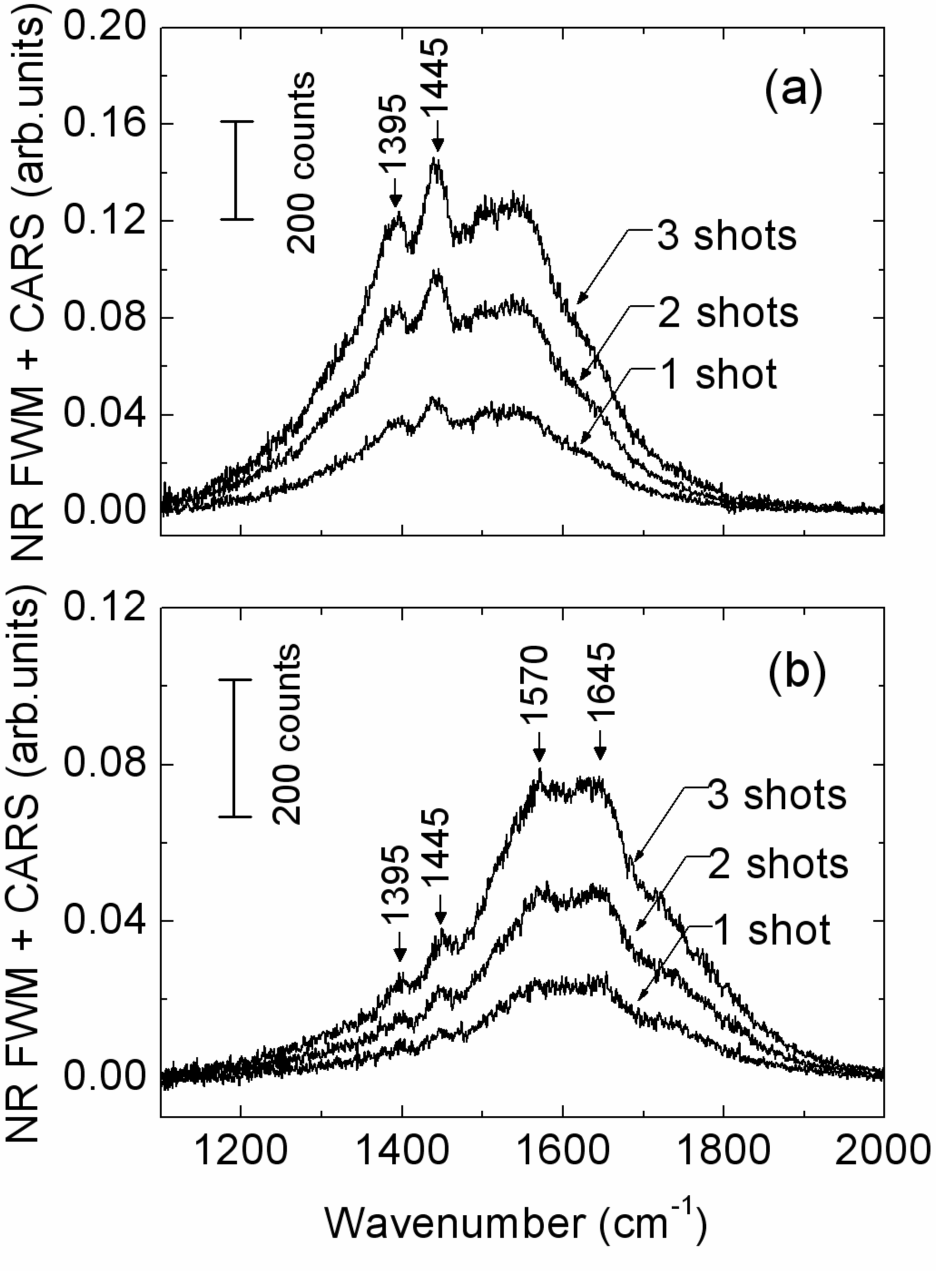

Fig. 7.8. Acquired CARS spectra for one, two, and three laser shots at the optimal probe delay. Sample is a pellet of B. subtilis spores. Parameters: pump wavelength λ_1 = 1.25 μm, 4 μJ/pulse; probe - λ_3 = 805.8 nm, $\Delta\nu_3$ = 30 cm^{-1}, 3 μJ/pulse; Stokes - λ_2 = 1.54 μm, 4 μJ/pulse (a); Stokes - λ_2 = 1.56 μm, 4 μJ/pulse (b). [64]

in only one to three laser shots. Spore Raman transitions in the fingerprint region (1300-1700 cm^{-1}) are apparent even after a single shot. For these measurements, the laser system is switched from normal (continuous) operation at 1 kHz rep rate into the single-shot mode, and the laser pulses are fired manually. The integration time of the CCD camera is set to 3 seconds to insure a comfortable time span for the manual firing of up to ten shots. The variation of the CCD integration time from 0.5 to 10 seconds has not shown any appreciable change in the noise level of the single-shot spectra, since the dominant part of the noise comes from the scattered laser radiation entering the spectrometer.

The pulse energies in Fig. 7.8 are deduced from the power measurements in the normal (continuous) operation mode. We have found, however, that they differ from the pulse energies for the laser system operated in the single-shot regime. The ratios of the single-shot to the continuous-mode pulse energies are 0.75, 0.47, and 1.3 for the pump, Stokes, and probe beams, respectively. They need to be taken into account to obtain the actual pulse energies used in the single-shot experiments.

Note that the single-shot spectra are obtained from a fairly small number of spores. Taking the effective laser pulse penetration depth for the highly-scattering sample (a clump of closely packed spores) to be 10 μm and the diameter of the probed region 32 μm, one gets a rough estimate for the probed volume of 10^4 μm^3. Allocating 1 μm^3 for a single spore gives about 10^4 contributing spores.

The dependence of the resonant CARS signal on the energy of the pump and Stokes pulses is shown in Fig. 7.9. Here, the resonant contribution is defined as an integral over the two Raman peaks, 1395 cm^{-1} and 1445 cm^{-1}. The reported pulse energies are again measured and reported for the continuous operation mode of the laser system. The data suggests that at high enough pulse energies, the dependence strongly deviates from the expected linear increase. The CARS signal magnitude saturates and even decreases at higher pulse energies. The total acquired signal, which is dominated by the NR contribution, exhibits similar dependence on the pulse energies but with a slightly weaker roll-of at the high-energy limit (not shown). At last, within the available

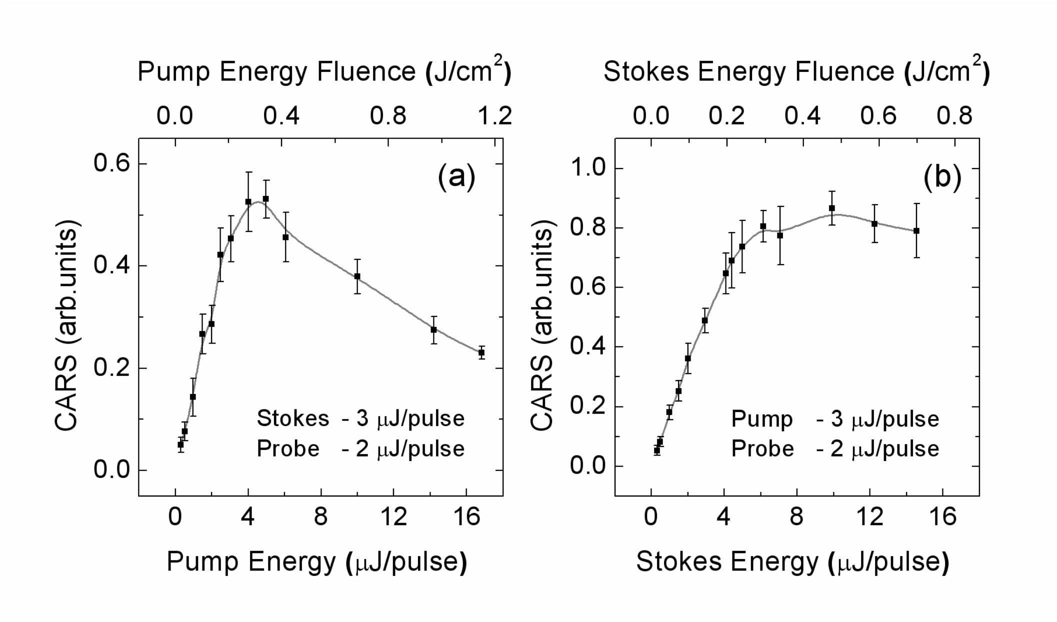

Fig. 7.9. The dependence of the CARS signal on the energy of the pump (a) and Stokes (b) pulses. Other parameters are: λ_1 = 1.24 μm, λ_2 = 1.54 μm, λ_3 = 805.7 nm, $\Delta\nu_3$ = 30 cm^{-1}. The CARS signal was recorded in the single-shot regime, moving the sample after each laser shot to avoid accumulated effects due to the laser-induced damage. [64]

range (up to 3 μJ/pulse), we have observed a linear dependence of the CARS signal on the energy of the probe pulse.

The saturation and decrease of the generated CARS signal as a function of the pump or Stokes pulse energies is probably due to the laser-induced damage of the exposed endospores. Taking into account the beam focusing and the scaling factors, we estimate the damage threshold for our spore sample to be 0.2 J/cm^2 per ultrashort pump or Stokes pulse. For 50-fs pulses, this energy fluence corresponds to a peak intensity of ~3×10^{12} W/cm^2. Note that this threshold is retrieved from the single-short measurements, and corresponds to ultrafast (femtosecond-scale) photodamage. We have also observed a longer-scale cumulative effect of CARS signal degradation as a function of the shot number. To avoid the substantial damage of the sample over a hundred laser shots, one needs to use a pulse energy fluence which is at least three times lower than the single-shot threshold value.

The obtained single-shot threshold, where the CARS signal dependence on the laser pulse energy deviates from linear, defines the ultimate limit to which the demonstrated results can be scaled with the energy, or rather the peak field intensity, of the input laser pulses. We speculate that higher electric fields modify molecular potential energy surfaces and unfavorably alter the Raman transitions strengths. As it follows from the next chapter, the magnitude of the induced coherence is still far from maximal and cannot account for the observed dependence of the CARS signal on the energies of the preparation pulses.

CHAPTER VIII

COHERENT VERSUS INCOHERENT RAMAN SCATTERING[*]

The instantaneous Raman excitation of molecular vibrations is a step that brings ultrafast coherent Raman spectroscopy to another level of complexity, as compared to the ordinary Raman measurements. A fair question to ask is how much one would benefit from it? In this chapter, a comparative experimental analysis of spontaneous and coherent Raman scattering on pyridine is presented. We report a 10^5-fold increase in the efficiency of the Raman scattering process due to the broadband pump-Stokes excitation. From the photon number ratio, we also infer the magnitude of the induced coherence, $\sim 0.5\times10^{-3}$. At last, we show the results of similar measurements on NaDPA powder, a strongly scattering medium.

1. Introduction

Because of the enhanced efficiency of the Raman scattering process, coherent Raman spectroscopy is conventionally believed to be more powerful than spontaneous Raman measurements [13, 84]. The enhancement comes from the presence of the driving fields and the coherent build-up of the generated signal over the sampled volume, provided that the phase-matching condition is satisfied. Let us note here though that the driving-field argument generally implies the use of strong laser pulses with durations, τ, on the order of the decoherence time of molecular vibrations or longer. Since the coherence relaxation time usually exceeds the vibration period, T_{vib}, by a few orders of magnitude, the relation $\tau >> T_{vib}$ is fulfilled.

On the other hand, ultrashort pulses, utilized in femtosecond CARS spectroscopy [23, 29, 32, 76, 85], have the duration on the order of the vibrational period or less. Moreover, the strengths of the driving fields that could be used in practice are limited by

---

[*] Part of the data reported in this chapter is reprinted with permission from "Coherent versus incoherent Raman scattering: molecular coherence excitation and measurement" by D. Pestov *et al.*, 2007. *Optics Letters*, 32, 1725-1727. Copyright 2007 by Optical Society of America.

undesirable processes, like photo-dissociation, ionization, self-focusing, and continuum generation. All above suggests that the traditional viewpoint needs to be reevaluated and a fair one-to-one comparison between spontaneous Raman and ultrafast coherent Raman spectroscopy should be made.

In this chapter [86], we make such a comparison for two strong Raman lines, 992 cm^{-1} and 1031 cm^{-1}, in pyridine (C_5H_5N). We quantify the increase in the efficiency of Raman scattering due to the coherent drive of molecular motion with a pair of ultrashort laser pulses, when the applied intensities are close to the limit ones. We infer the magnitude of the induced coherence from the relation:

$$\frac{P_{CSRS}}{P_{SpRaman}} \cong \lambda_3^2 \frac{N}{V} \frac{|\rho_{bc}|^2}{\rho_{cc}} \Delta L, \tag{8.1}$$

discussed elsewhere (ref. [87], see also Appendix D). Here, P_{CSRS} and $P_{SpRaman}$ are time-averaged total fluxes of the photons generated through CSRS and spontaneous Raman scattering of a particular vibrational mode; λ_3 is the wavelength of the probe pulse, ΔL is the length of the medium, and N/V is the concentration of the Raman-active molecules; ρ_{cc} is the population of the molecular ground state $|c>$, and ρ_{bc} is the induced coherence between the state $|c>$ and excited Raman-active state $|b>$. Note that equation (8.1) has no parameters other than those available directly from the experiment.

2. Experimental

For straightforward comparative analysis of the two processes, we employ a hybrid technique for CSRS, described in the context of CARS spectroscopy earlier. Conveniently, in such a scheme the same narrowband laser pulse can be utilized for spontaneous Raman measurements. Only the difference in the collection of the generated signal has to be taken into account.

For this experiment, we again employ a femtosecond Ti:Sapphire-based laser system (Legend, Coherent: 1 kHz rep.rate, ~1 mJ/pulse) with two OPAs (OPerA-

VIS/UV and OPerA-SFG/UV, Coherent), described in detail in Chapter II. Briefly, the output of the first OPA ($\lambda_1 = 738$ nm, $\Delta\nu_1 \approx 260$ cm^{-1}) and a small fraction of the regenerative amplifier output ($\lambda_2 = 802$ nm, $\Delta\nu_2 \approx 480$ cm^{-1}) are used as pump and Stokes beams. The output of the second OPA, the probe beam ($\lambda_3 = 577.9$ nm), is sent through the home-made pulse shaper. The three beams are overlapped in the BoxCARS geometry (under ~5° to each other) and focused on a sample. The FWHM beam diameter in the focal plane is about 57 μm, 75 μm, and 47 μm for the pump, Stokes, and probe, respectively.

The collection part for CSRS and spontaneous Raman photons differ (see the layout in Chapter II). While the directional CSRS beam is spatially filtered with a small-aperture iris (I2), the incoherently scattered light is collected from the back of the sample (under about 30° to the main axis) with a 2-inch short-focal lens (f = 10 cm). A 2-inch iris (I1), installed right after the lens, is used to change the solid angle, over which the photons are collected. Each of the two acquired signals is sent through the same set of bandpass filters and refocused onto the entrance slit of the spectrometer (Chromex Spectrograph 250is) with a LN2-cooled CCD (Spec-10, Princeton Instruments). When CSRS signal is recorded, an extra set of calibrated neutral density filters is used to avoid CCD saturation.

3. Results and Discussion

Similar to femtosecond CARS, hybrid CARS/CSRS technique is based on broadband excitation of molecular vibrations, which however, is followed by multi-channel, frequency-resolved probing of the induced coherence with a time-delayed narrowband pulse. Fig. 8.1 illustrates the transition from the traditional time-resolved measurement of free induction decay in pyridine to the frequency-resolved one by cutting the bandwidth of the probe pulse from 300 cm^{-1} to 15 cm^{-1}. Note that the spectrograms in Figs. 8.1(a-d) were acquired with ten-fold attenuation of the collected CSRS signal to

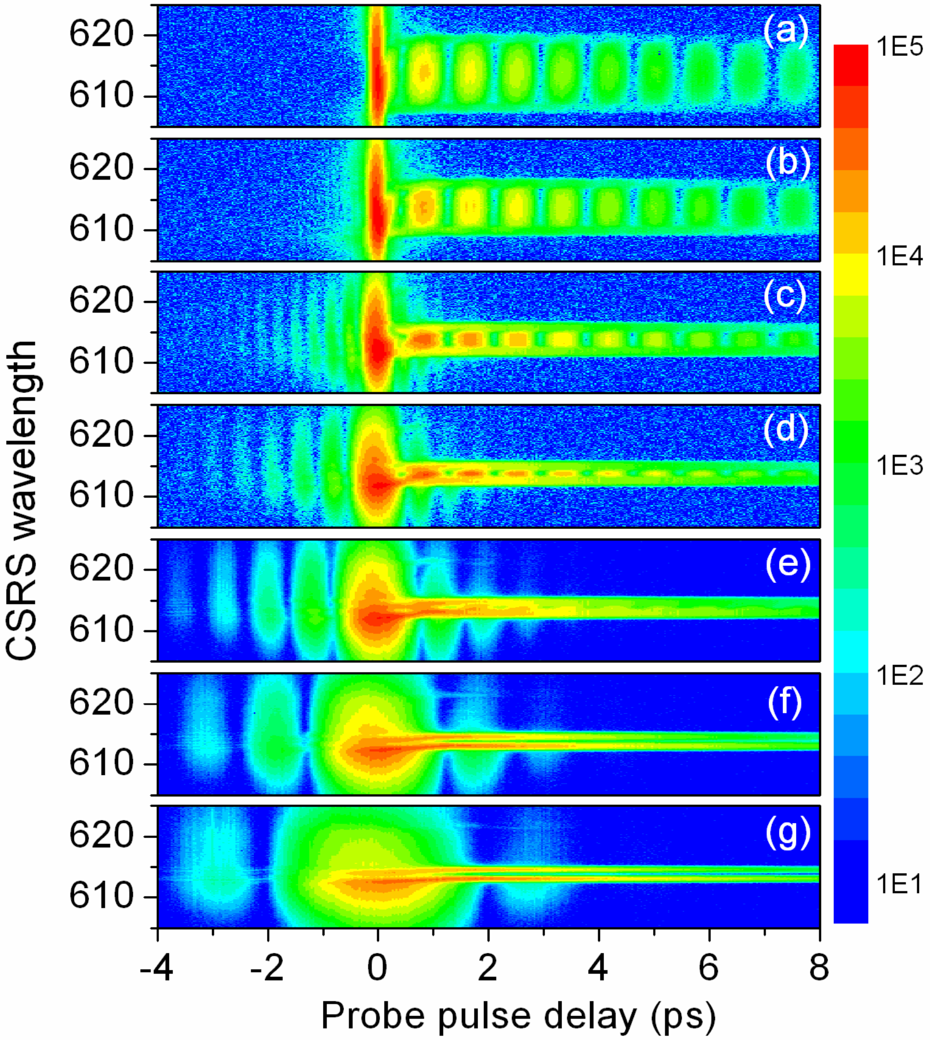

Fig. 8.1. Transition from time-resolved to hybrid CSRS: CSRS spectrograms for different spectral bandwidths of the probe pulse - (a) 300 cm^{-1}, (b) 200 cm^{-1}, (c) 100 cm^{-1}, (d) 60 cm^{-1}, (e) 40 cm^{-1}, (f) 25 cm^{-1}, (g) 15 cm^{-1}. Two Raman lines of pyridine, 992 cm^{-1} and 1031 cm^{-1}, are excited via a pair of ultrashort laser pulses. Pump: $\lambda_1 =$ 737 nm, $\Delta\nu_1 \approx$ 260 cm^{-1}, 0.5 μJ/pulse. Stokes: $\lambda_2 =$ 801 nm, $\Delta\nu_2 \approx$ 480 cm^{-1}, 0.9 μJ/pulse. Probe: $\lambda_3 =$ 577.9 nm, 0.15 μJ/pulse. The energy of the probe pulse is kept constant while its spectral bandwidth is varied. For (a-d), the collected signal is attenuated by a ND=1 filter to avoid saturation of the CCD.

avoid saturation of the CCD at zero probe delay. This is why the noise level in Figs. 8.1(a-d) is slightly higher than in Figs. 8.1(e-g).

The beating pattern between two excited Raman modes (see Fig. 8.1(a) and Fig. 8.2) gradually transforms into a couple of spectrally isolated streak lines. The smooth NR FWM profile due to the instantaneous electronic response stretches along the time axis, indicating the expected lengthening of the probe pulse, and gain side-fringes due to the rectangular-like spectral amplitude mask imposed by the pulse shaper. A cross-section of the spectrograms for the narrowband probe at some fixed positive delay gives a CSRS spectrum. It is advantageous to pick up the delay corresponding to the first node of FWM. For such a delay one gets a strong CSRS signal without the interfering NR background. If the probe pulse is short enough (a few times less than the dephasing time), the coherence decay for this probe delay is negligible.

Spontaneous Raman and CSRS spectra of the excited vibrational modes, acquired at the described setup with a 200-μm cuvette of pyridine, are shown in Fig. 8.3. The spontaneous Raman measurements are done with the pump and Stokes beams blocked. The largest available aperture is used for the signal collection. The integration time is 3 minutes. CSRS spectrum is acquired for the close-to-limit pump and Stokes pulse energies. They are 0.74 μJ and 1.36 μJ per pulse, respectively. Assuming transform-limited preparation pulses with Gaussian profiles, one gets their peak intensities on the sample to be about 4×10^{11} W/cm^2. The integration time is only 1 second, even though the photon flux is attenuated by a factor 10^4 via the neutral-density filters in front of the spectrograph. The probe delay relative to the preparation pulses (~1.8 ps) is optimized to get rid of the NR contribution while keeping the CSRS signal magnitude close to maximum.

The numbers clearly indicate that the efficiency of CSRS process is much higher than of spontaneous Raman scattering (CSRS photon flux is seven orders of magnitude stronger than the flux of collected spontaneously-scattered photons). However, their quantitative comparison requires some analysis of the signal collection. Indeed, while virtually all CSRS photons contribute into the spatially filtered beam of the coherently

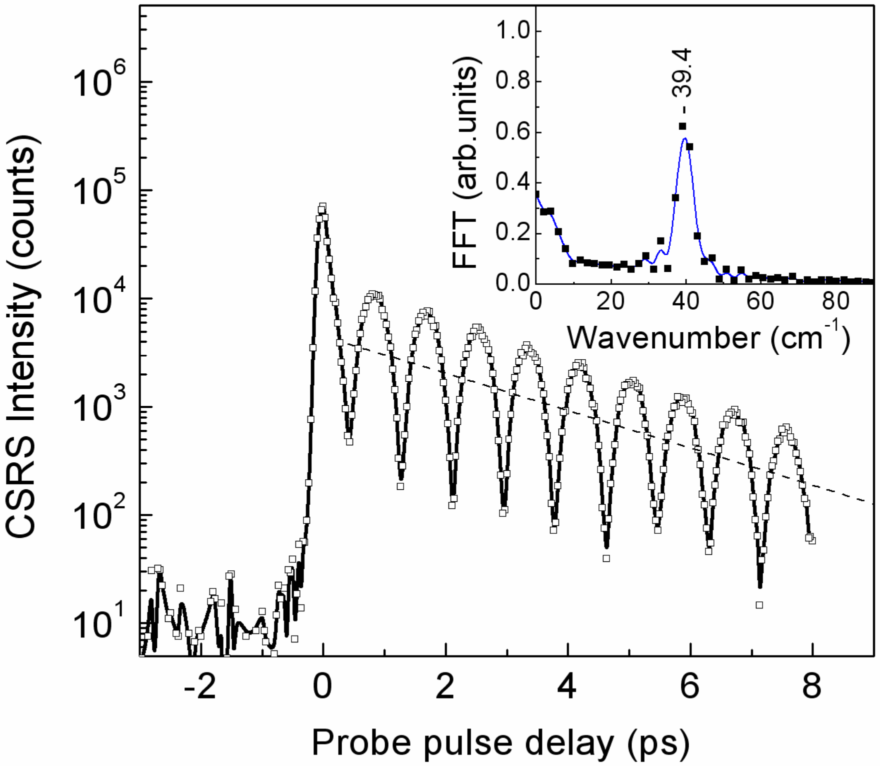

Fig. 8.2. Cross-section of the spectrogram in Fig. 8.1(a) at λ = 614 nm. The beating at positive probe delays is a result of interference between the two excited vibrational modes of pyridine, 992 cm^{-1} and 1031 cm^{-1}. The dashed line corresponds to the dephasing time T_2 = 5.0 ps. Inset: Fast-Fourier Transform of the CSRS signal from 0.4-8 ps interval, corrected for the exponential decay and DC offset. The retrieved beat frequency is 39.4 cm^{-1}.

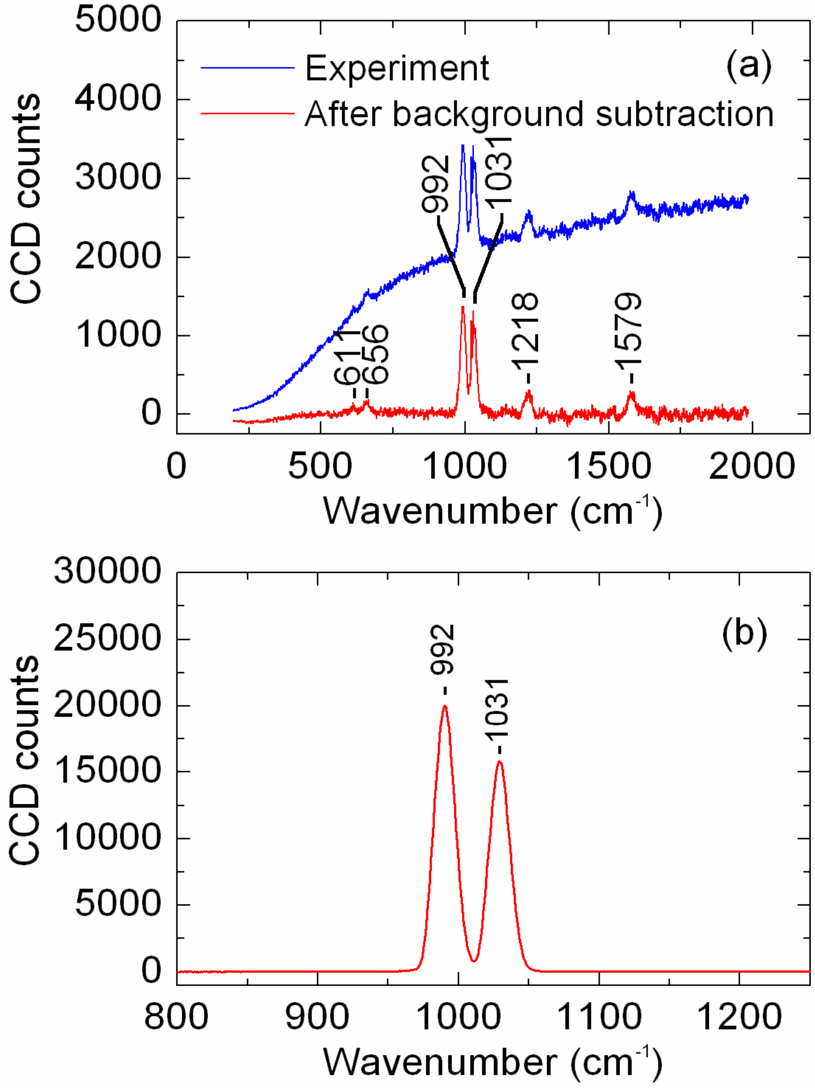

Fig. 8.3. Spontaneous versus coherent Raman scattering on the neat solution of pyridine: (a) Spontaneous Raman spectrum of pyridine. Probe pulse parameters: λ_3 = 577.9 nm, $\Delta\nu_3 \approx 19$ cm^{-1}, average power is 0.13 mW (0.13 μJ/pulse, 1 kHz rep. rate). Integration time is 3 min. The smooth background profile is determined by the transmission of the bandpass filters set in front of the spectrometer. Cuvette path length is 200 μm. (b) CSRS spectrum of pyridine. The two Raman lines, 992 cm^{-1} and 1031 cm^{-1} are selectively excited via a pair of ultrashort pulses. The probe delay relative to the preparation pulses is fixed and equal to 1.8 ps. Pump: λ_1 = 738 nm, $\Delta\nu_1 \approx 260$ cm^{-1}, 0.72 μJ/pulse; Stokes: λ_2= 802 nm, $\Delta\nu_2 \approx 480$ cm^{-1}, 1.36 μJ/pulse. Probe parameters and the sample are the same as spontaneous Raman measurements. With 10^4-attenuation by a set of neutral-density filters, integration time is 1 sec. [87]

scattered light, only a small fraction of spontaneous Raman photons is collected with the 2-inch lens at 10-cm focal distance from the sampled spot. Refraction on the sample-air interface and prominent lens aberration because of the large aperture make the effective collection angle even smaller.

A simple model, neglecting the reflection of light on the interfaces other than the total internal reflection, gives the following distribution of the radiation outside the cuvette:

$$S(\theta,\varphi)=\frac{|\cos\theta|}{4\pi n\sqrt{n^2-\sin^2\theta}}\,,\ \theta\neq\frac{\pi}{2}\,. \tag{8.2}$$

Here, θ and φ are spherical angle coordinates with the z-axis normal to the surface of the cuvette; n is the index of refraction of the sample (we use n=1.509 for pyridine). It is implied that the distribution inside the sample is isotropic and the thickness of the cell is negligible. The quartz walls between the sample and the air contribute into the reflection but do not change the angular distribution $S(\theta,\varphi)$. Note that for n equal to 1, $S(\theta,\varphi)\equiv 1/(4\pi)$. When the refractive index is different from 1 and θ is small, $S(\theta,\varphi)\approx 1/(4\pi n^2)$. One can say that the refraction leads to n^2 reduction of the effective solid angle, Ω_{eff}, over which the photons are collected:

$$\Omega_{eff}=4\pi\int S(\theta,\varphi)\sin\theta\, d\theta\, d\varphi\,. \tag{8.3}$$

While taking into account the corrections due to the angle- and polarization-dependent light reflection is subtle, we estimate its contribution to be below 8%. At the same time, the signal reduction because of the ray refraction is on the order of 50%, i.e. dominant, which justifies the simplifications above.

The dependence of the effective solid angle on the aperture area, calculated from (8.3), is shown in Fig. 8.4. It is practically linear, as one would expect for an isotropic distribution, but the magnitude of the solid angle is scaled down by a factor of two (~ n^2). The red solid-line curve in Fig. 8.4 is deduced from the measured dependence of spontaneous Raman signal on the collection aperture. For proper normalization, the

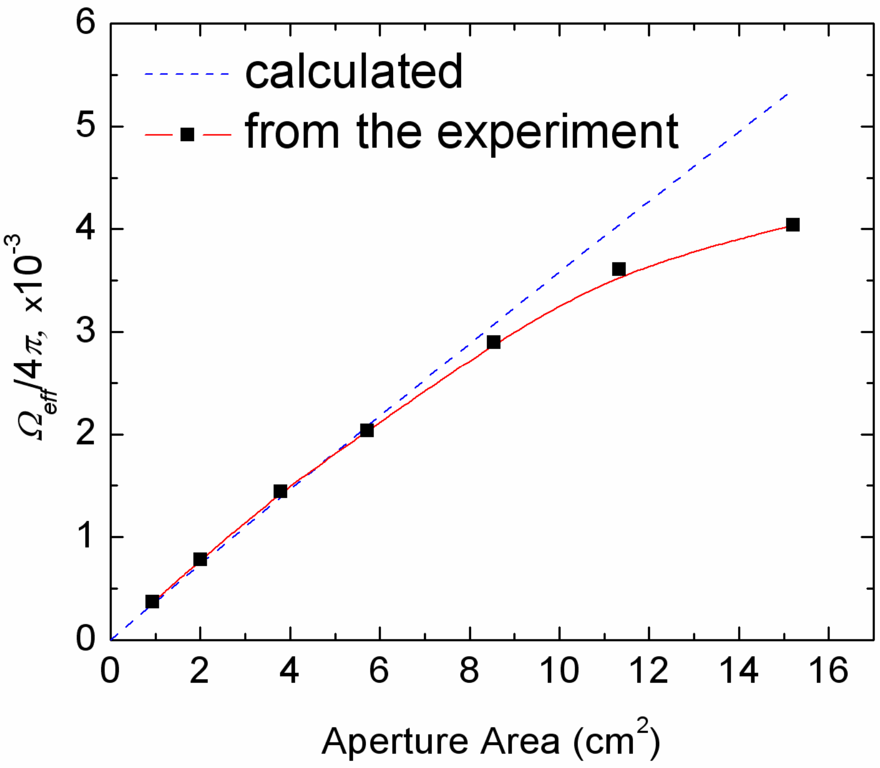

Fig. 8.4. Effective collection angle as a function of the aperture area (iris I1 in Fig. 2.3), calculated from Eqs. (8.2) and (8.3) (dashed blue line) and retrieved from the measured dependence of the spontaneous Raman signal on the aperture area (solid red line). The discrepancy between the two in the large-area limit is attributed to collection lens aberrations and reflection losses.

assumption that the theoretical and experimental curves should merge in the small-area limit is used. The discrepancy between the two in the large-area limit is attributed to the lens aberration and angular-dependent reflection losses, which have not been accounted for in the model.

From the analysis above it follows that for the spontaneous Raman spectrum in Fig. 8.3(a), $\Omega_{eff}/(4\pi) \approx 0.004$, and therefore, for the two excited Raman transitions

$$\frac{P_{CSRS}}{P_{SpRaman}} = \frac{P_{CSRS}}{P^{c}_{SpRaman} \times (4\pi / \Omega_{eff})} \approx (1.1 \text{ and } 0.9) \times 10^{5} \qquad (8.4)$$

for 992 cm^{-1} and 1031 cm^{-1}, respectively. Here $P^{c}_{SpRaman}$ stands for the time-averaged flux of the spontaneously scattered photons collected in the experiment over the effective solid angle.

From the parameters of the cell, it is reasonable to infer that $\Delta L \approx 200$ μm. This assumption is confirmed by the proper scaling of the number of the acquired photons when the 200-μm cuvette is substituted with a 100-μm one. Namely, we observe a reduction by a factor of 2 and 4 for the spontaneous Raman and CSRS signal amplitude, respectively (see Fig. 8.5). Note, however, that for a 500-μm cell the number of collected CSRS photons is less than one would expect from the scaling. In this case the actual interaction length is below 500 μm because of the beams' overlap geometry.

Plugging in $\Delta L = 200$ μm, the density of pyridine molecules, and the probe wavelength, one gets $(N/V)\lambda_3^2 \Delta L \approx 5\times10^{11}$. Since the thermal population of the excited Raman states is negligible, we take $\rho_{cc} \approx 1$ and from Eqns. (8.1) and (8.4) obtain $\rho_{bc} \approx$ (0.46 and 0.43)$\times10^{-3}$ for the two Raman transitions. A crude estimate of the expected magnitude of the coherence from a steady state solution [25], $\rho_{bc} \approx \left|\Omega_1^{*}\Omega_2 / \Delta\right| \tau$, of the density matrix equations gives $\rho_{bc} \sim 10^{-2}$, which is in reasonable agreement with the retrieved values. Here, $\Omega_j \equiv \wp_j E_j / (2\hbar)$ stands for Rabi frequencies of the pump and Stokes fields, Δ is the detuning from the electronic resonance, and τ is the pulse length.

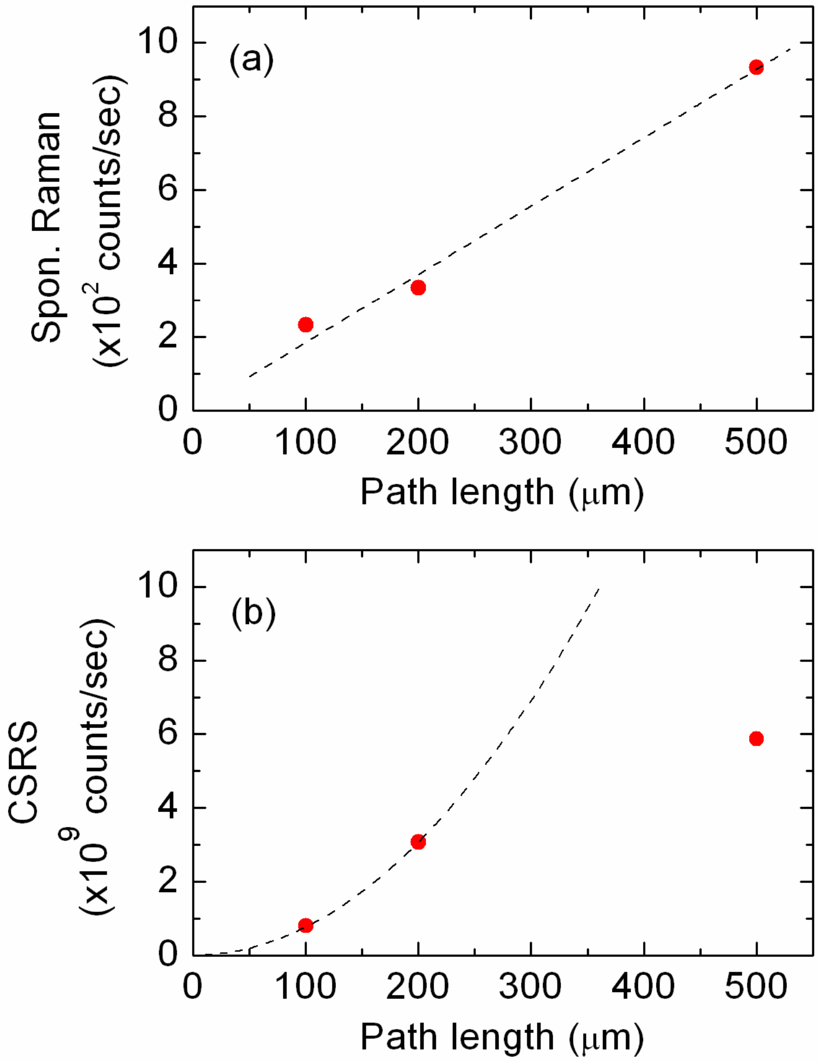

Fig. 8.5. Scaling of spontaneous Raman (a) and CSRS (b) photon fluxes with the length of the cuvette. The photon counts are integrated over the spectrum and normalized on the acquisition time for each of the experiments.

For the estimate, we take the dipole moments to be 1 Debye, τ ~50 fs, and the detuning $\Delta \approx 3\times10^{15}$ rad/s, since the closest absorption band of pyridine is at λ ~260 nm.

As one can see, the coherence is far from maximal. The observed 10^5-fold gain in the efficiency of coherent Raman scattering over incoherent one comes entirely from the phase-driven buildup of the signal over the active volume. For similar excitation strength but $\Delta L \sim$ 1 μm, typical for microscopy, one would have $P_{CSRS} / P_{SpRaman} \approx$ 500 (see, e.g. [87]).

The last estimate agrees with the measurements on NaDPA powder, Fig. 8.6, where the coherent buildup of the frequency-shifted radiation is mitigated by strong scattering within the sample. The experiment with NaDPA powder is similar to the described above but the laser pulse wavelengths are shifted into IR domain (λ_1 = 1285 nm, λ_2 = 1565 nm, λ_3 = 805.5 nm), i.e. other OPAs' options are used. Also, the frequency-shifted photons are collected in the backscattering geometry for both CSRS and spontaneous Raman measurements.

From the curves (a) and (c) in Fig. 8.6, one gets the ratios between the peaks at 1395, 1442, and 1572 cm^{-1} in CSRS and spontaneous Raman spectrum to be 484, 274, and 38, respectively. Obviously, they depend on how well the Raman transitions are excited by the pump-Stokes pair. The ratios are also affected by the energies of the excitation pulses, which were chosen close to the laser-induced damage threshold. The sample was continuously rotated to avoid heat-assisted damage of the sample.

All above suggests three-orders-of-magnitude enhancement in the photon flux as a figure-of-merit for coherent Raman spectroscopy of NaDPA powder, as an example of highly-scattering medium. Please to note though that the three-orders-of-magnitude increase of the acquisition time will not result in spontaneous Raman spectrum with similar signal-to-noise ratio. This is because the noise amplitude also increases with the acquisition time, T_{acq}. In particular, shot noise scales as $\sqrt{T_{acq}}$.

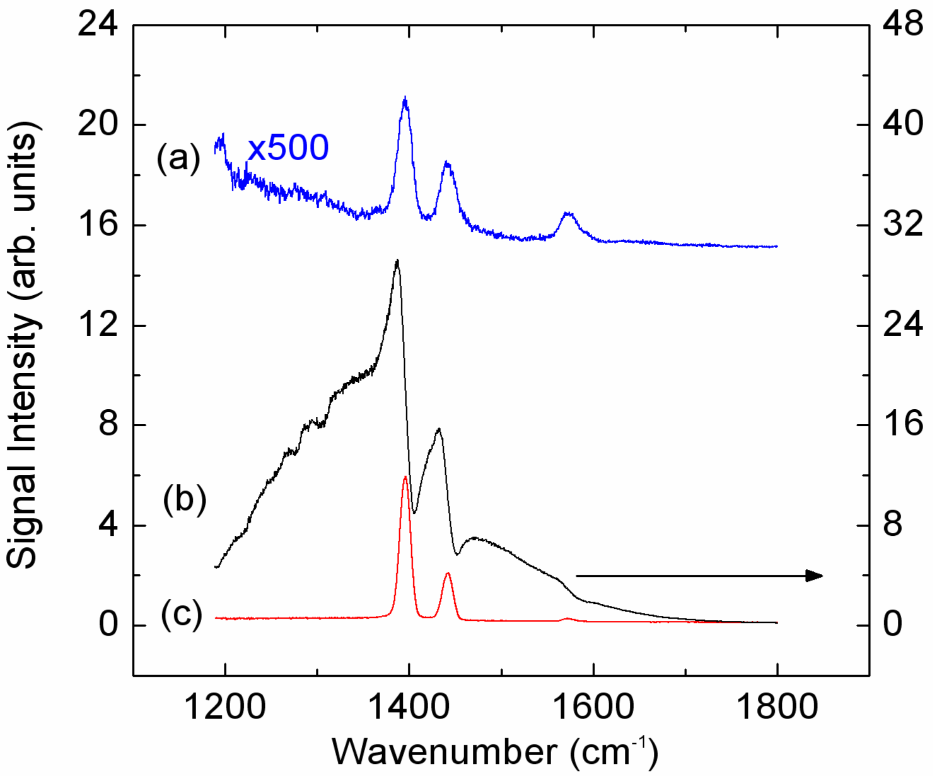

Fig. 8.6. Spontaneous versus coherent Raman scattering on NaDPA powder: (a) spontaneous Raman spectrum of NaDPA, scaled by a factor 500; (b) CSRS spectrum of NaDPA powder at zero probe delay; (c) CSRS spectrum at probe delay 1.3 ps. All spectra are normalized on the acquisition time as well as a calibration spectrum, recorded with the probe beam blocked. The last step is necessary to remove the modulation of the spectral intensity due to etaloning effect, common for back-illuminated CCDs. Pulse parameters are: pump – λ_1 = 1285 nm, 10 μJ/pulse; Stokes – λ_2 = 1565 nm, 10 μJ/pulse; probe – λ_3 = 805.5 nm, $\Delta\nu_3 \approx 14$ cm^{-1}, 1.7 μJ/pulse.

4. Conclusions

We have performed comparative spontaneous and coherent Raman measurements on pyridine and NaDPA powder. For the neat solution of pyridine, we have quantified the increase in the efficiency of Raman scattering process due to the impulsive pump-Stokes excitation of molecular vibrations and retrieved the coherence amplitude for the corresponding Raman transitions. The measurements show that while the coherence is far from maximal ($\rho_{bc} \sim 0.5\times10^{-3} << 0.5$), the number of CSRS photons still exceeds the number of spontaneous Raman photons by several orders of magnitude. In particular, we demonstrate their ratio to be 10^5 for the 200-μm interaction length and reasonably high energies of the preparation pulses (~1 μJ/pulse, ~50 fs; the estimated peak intensity $\sim 4\times10^{11}$ W/cm^2). Note that the coherence amplitude for the excited molecular vibrations in pyridine was calculated from the acquired experimental data, without any *a priori* knowledge about the molecular structure. The procedure separates out the preparation and probing of the coherence, making it easier to draw comparison between the theory and experiment.

Similar comparative measurements on NaDPA powder give three orders of magnitude enhancement in the efficiency of Raman scattering process when the ultrashort preparation pulses are used. Although for a rigorous analysis one has to take into account the difference in the oscillator strengths of the considered Raman transitions, we speculate that the observed diminished efficiency of CSRS, as compared to the data obtained on pyridine, is primarily due to the elastic scattering of photons, both incoming and generated, inside the sample. We estimate the effective length of the sample, where the laser pulses contribute to CSRS, to be only 10 μm, as opposed to 200-μm length in pyridine. We also speculate that because of the elastic scattering, the generated CSRS photons, reaching the detector, are partially incoherent.

CHAPTER IX
SUMMARY

We briefly summarize here the milestones of the undertaken study and point out the remaining challenges. We also give a somewhat broader perspective on the devised hybrid CARS technique, which holds exciting promise to find use for many practical applications other than bioagent detection, emphasized in this work.

1. Summary and Conclusions

With a goal of developing a laser detection technique based on coherent Raman scattering, we have performed a series of CARS (and CSRS) measurements on different types of samples. We started off with the proof-of-principle femtosecond CARS experiments on easy-to-handle organic liquids, such as methanol. Then, we moved on to the molecule of interest, DPA and its salts, and continued with DPA solutions and powders. Finally, we concentrated on detection of B. subtilis spores, a harmless analog of B. anthracis. The results of all those experiments can be summarized as follows.

The femtosecond CARS technique is proved useful for studying molecular dynamics and for extracting the intrinsic characteristics of molecular motion. When applied to methanol, this technique allows one to determine the coherence relaxation times and frequency difference between the excited Raman modes. It also makes possible to observe the dependence of coherence dephasing rates on the surrounding environment.

Time-resolved CARS from DPA in NaOH buffered solution is demonstrated. In these first measurements, the C-H stretching modes in 3000-3200 cm^{-1} are accessed. While this is not a fingerprint region in Raman spectra of DPA and its salts, the results indicate the feasibility of time-resolved CARS on such a complex organic compound. The strong NR FWM background due to the solvent contribution is removed by delaying the probe pulse relative the overlapped excitation pulses.

Femtosecond CARS measurements with UV-probe pulse are performed on NaOH or KOH buffered solutions of DPA as well as common chemicals (ethyl alcohol, acetone, cyclohexane, etc.). The Raman transitions of NaDPA in the fingerprint region (1300-1700 cm^{-1}) are addressed. The quantum beats between the excited Raman modes at 1383 cm^{-1}, 1435 cm^{-1}, as well as 1569 cm^{-1} are obtained. The frequency difference and relaxation constants are extracted from the recorded CARS and CSRS traces. We show that CARS and CSRS processes are equivalent in a sense that they provide similar information about the target molecule. We also note that the acquisition of the whole CARS (or CSRS) spectrum rather than scattered photons at a single pre-selected wavelength gains toward reproducibility of the experimental data and their comprehensiveness.

The specificity of time-resolved CARS technique is demonstrated by recording CARS traces for DPA solution and common interferents. We show that the detection algorithm can be based upon the FFT of the recorded time-resolved CARS data. In particular, the normalized beat frequency component can be used to discriminate DPA molecules against their interferents. An extension of this idea to the spectrograms might be indispensable for the task of molecule recognition.

The dependences of the coherent Raman signal on the concentration of NaDPA and the wavelength of the probe pulse, near-resonant to the electronic transition (~ 272 nm), are investigated. The carried out transmission and refractive index measurements on NaOH buffered solutions of DPA aid in the interpretation of the experimental data with UV probe. In particular, the observed non-parabolic dependence of the CARS (and CSRS) energy on the concentration of NaDPA solution is explained by the dominant role of changing phase-matching conditions in the presence of strong absorption. We also conclude that the foreseen advantages of one-photon electronic resonant probing of the excited molecular vibrations are diminished by the large bandwidth of the resonant transition. The still favorable trend of the scattering efficiency, enhanced towards UV, is overturned, in practice, by the laser-induced damage of the sample.

All-visible CARS on DPA and NaDPA powders is demonstrated. The quantum beats between two excited Raman modes (1577 and 1644 cm^{-1} for DPA; 1395 and 1442 cm^{-1} for NaDPA) are retrieved even in the presence of multiple scattering. The scattered signal is collected in the backward geometry, which is another step forward towards a feasible detection scheme.

We demonstrate mode-selective excitation of Raman transitions at 1395 and 1442 cm^{-1} in a femtosecond CARS experiment on NaDPA powder. To limit the bandwidth of the excitation, we utilize linearly chirped pump and Stokes pulses. The chirping is done by sending the femtosecond pulses through 4-cm thick SF-11 glass. Fine tuning (to match the chirp of the two pulses) is accomplished by the use of a pulse shaper for one of the two beams. The width of the tunable “Raman excitation window” is estimated to be 35 cm^{-1}, which is ten-fold smaller than the spectral width of the pump-Stokes convolution for transform-limited laser pulses.

Overall, we have successfully demonstrated the applicability of time-resolved technique for CARS spectroscopy of opaque solids. We, however, have failed to observe species-specific CARS signal from B. subtilis spores with this technique. The recorded CARS signal on spores is purely due to the NR FWM, with no sign of interference or other signatures of Raman-resonant response. No conclusive evidence of the resonant response has been found in the time-resolved CARS data.

The experiments indicate the inherent problem associated with time-resolved measurements. Namely, the use of the multimode interference pattern for species recognition requires the ability to record high-quality quantum beat profiles over a relatively large probe delay span and therefore, is challenging in the presence of scattering and fluctuations. For spores, the situations is further complicated by much shorter decoherence times of the Raman transitions, as compared to DPA and NaDPA powders. The sought CARS signal decays faster than the trailing tail of NR FWM due to the multiple scattering inside the sample.

Hybrid technique for coherent Raman spectroscopy is developed, implemented, and successfully applied to CARS on NaDPA powder and B. subtilis spores. Even in the proof-of-principle experiments, the good-quality spectrally-resolved CARS signal from B. subtilis spores is retrieved after only 2 minutes of acquisition. Further optimization of the hybrid CARS setup has led to a single-shot acquisition of CARS spectrum from as few as ~10^4 bacterial spores, bringing the technique to the upfront of the potential optical schemes for biohazard detection.

At last, the developed technique is used for a comparative analysis of spontaneous Raman and CSRS on a neat solution of pyridine and NaDPA powder. For the liquid sample, we observe a 10^5-fold increase in the efficiency of the Raman scattering process due to the broadband pump-Stokes excitation and estimate the magnitude of the established coherence to be 0.5×10^{-3} (the theoretical limit is 0.5). Similar measurements on NaDPA powder indicate that for the pulse energies used in our experiments, the number of CSRS photons is about 10^3 times higher than the number of photons produced through spontaneous Raman scattering.

With all the work reported here, there are a lot of issues that remain unresolved and prevent us from immediate implementation of the devised approach into a practical device. The most obvious one is the complexity and cost of the laser system, which make the setup bulky, fragile, and unaffordable. We now develop a single-oscillator-based system that would address these deficiencies at the expense of tighter focusing of the laser beams. A generic setup schematics of the developed system is given in Fig. 9.1. The pump-Stokes pulse pair is now replaced with a single ultrashort laser pulse (impulsive excitation), and narrowband probe pulses are produced by sending the fundamental beam through a thick second-harmonic crystal.

Another apparent issue that hasn’t been discussed is the sample preparation and handling (for local detection). In the mailroom scenario, where post mails are scanned for suspicious substances, it is not feasible to detect those by shooting the laser pulses through mail envelopes. The paper material severely distorts the pulse shape (see Fig. 9.2). A plausible alternative is the implementation of a vacuum system, analogous to one described in [9], that would collect particles onto a surface of a properly chosen air filter. The trapped fragments would be then put into the laser focus for analysis.

Finally, a robust detection algorithm (based on the acquired CARS spectra) still has to be developed and thoroughly tested; the so-called Receiver Operating Characteristic curve (ROC-curve), which characterizes the performance of the detection scheme, is to be obtained. Our first steps in this direction are described in [88]. It is still unclear if the technique is able to differentiate between different kinds of bacterial spores, since their Raman spectra are strikingly similar.

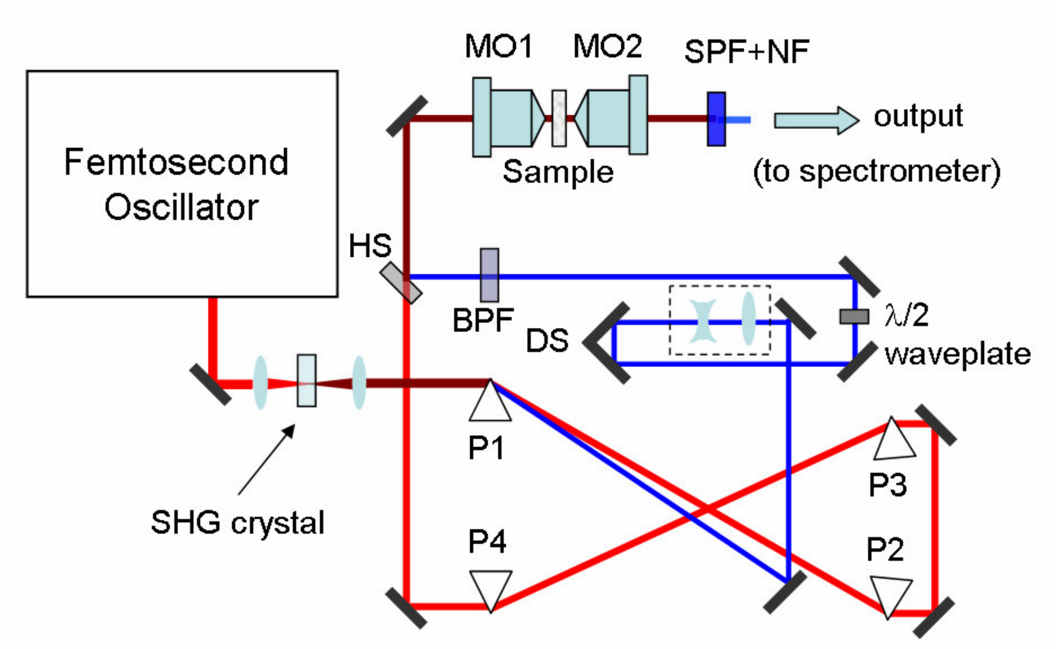

Fig. 9.1. Hybrid CARS microscope layout. SHG, second-harmonic generator; P1-4, prisms; HS, harmonic separator; DS, delay stage; BPF, bandpass filter; MO1,2, microscope objectives; SPF+NF, shortpass and notch filters.

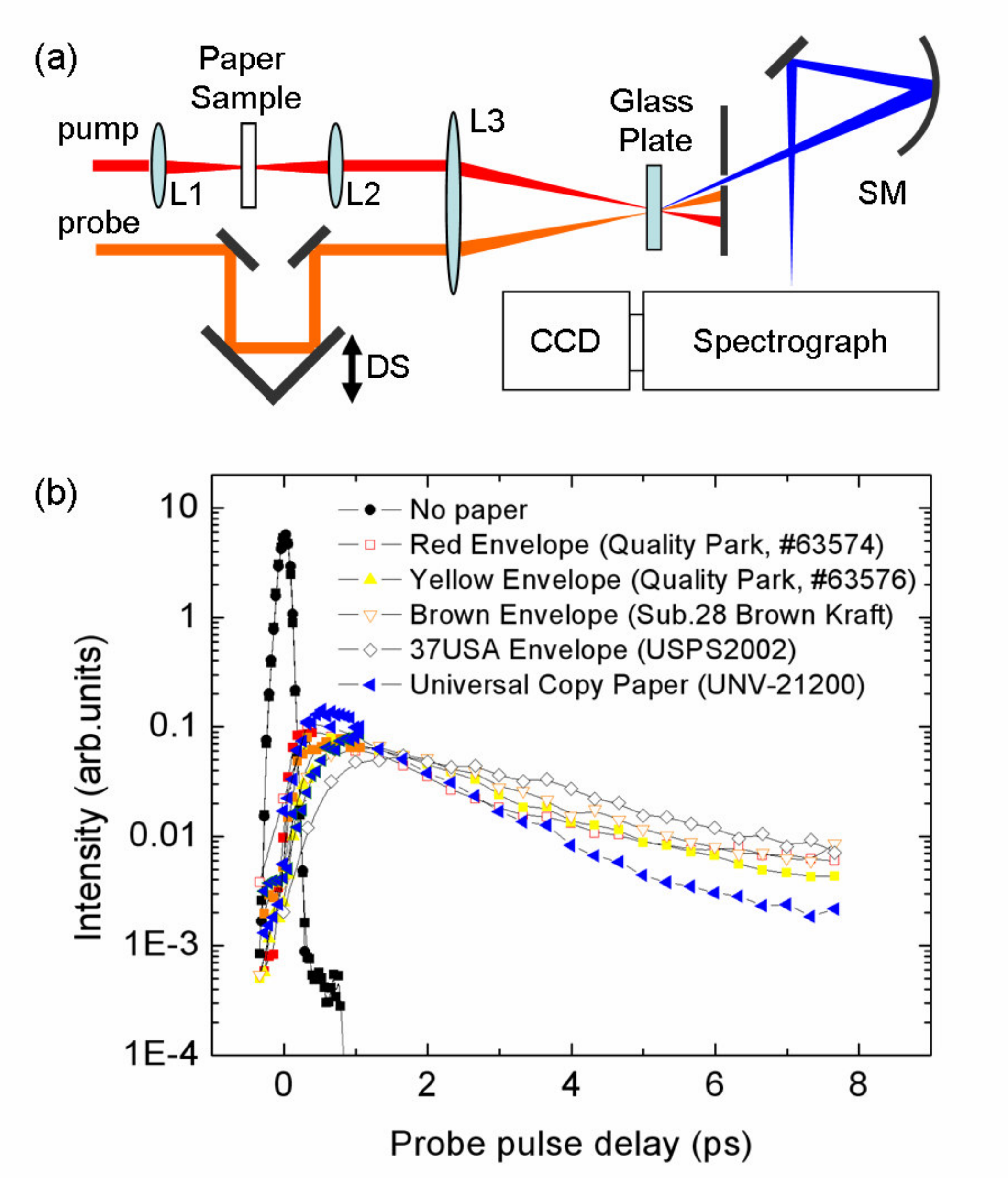

Fig. 9.2. Propagation of ultrashort laser pulses through paper. (a) Setup schematics. The pump pulse (λ_p = 716 nm) is focused on a piece of paper. The transmitted light is collected and cross-correlated with another ultrashort pulse (λ_{pr} = 578 nm). Four-wave-mixing signal ($\omega_{FWM} = 2\omega_{pr} - \omega_p$; $\lambda_{FWM} \approx 485$ nm) is recorded as a function of the probe pulse delay. L1-3, lenses; DS, delay stage; SM, spherical mirror; CCD, charge-coupled device. (b) Acquired cross-correlation profiles for different types of paper.

2. Outlook

The developed hybrid technique for coherent Raman spectroscopy has a number of attractive properties. Discrimination of the Raman-resonant signal against the NR background, multimode Raman excitation, and straightforward interpretation of the acquired data are to name a few. Besides biohazard detection, the scheme can be used for many other applications requiring chemical specificity and fast acquisition rates. Chemically-selective imaging or CARS microscopy [63, 71, 72, 89, 90] of biological tissues and photolithographic polymers, non-invasive measurements of glucose level in blood stream, real-time monitoring of natural gas composition are problems currently worked on in our laboratory.

CARS on gases, even on ambient air, comes into play when the BoxCARS arrangement of the three laser beams, used throughout this work, is replaced with a all-collinear geometry (see Fig. 9.3). This is again due to the phase matching condition, which is satisfied for media with negligibly low dispersion when the laser pulses co-propagate. An example of CARS spectrogram recorded with a gravimetrically prepared gas mixture, mimicking natural gas composition, is shown in Fig. 9.4. The lines of methane and CO_2 clearly stand out in the background-free spectrum (Fig. 9.4(b)). However, their magnitudes depend upon not only corresponding oscillator strengths of the excited Raman modes but parameters of the preparation pulses. We argue that normalization of the acquired spectra on NR FWM profiles, as is done in Fig. 9.5, might help to eliminate the uncertainty due to the excitation conditions. The difficulty is to achieve high reproducibility for the peak ratios (0.1-0.01%), required for practical applications.

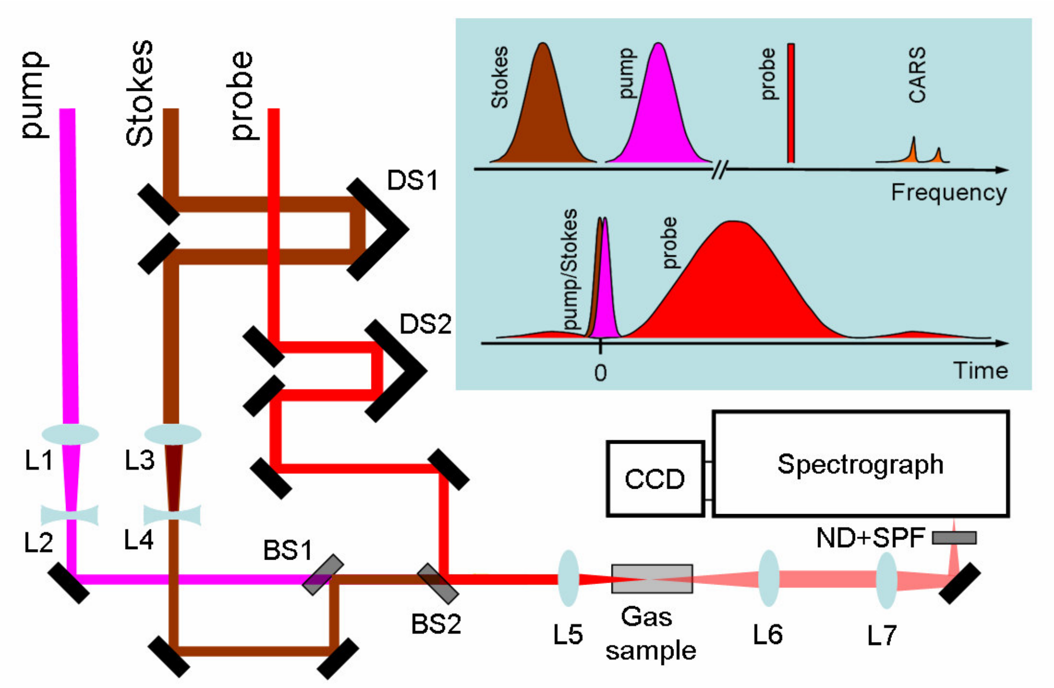

Fig. 9.3. All-collinear CARS setup for gas experiments. L1-7, lenses; DS1,2, delay stages; BS1,2, beam splitters; CCD, charge-coupled device; ND+SPF, a set of neutral-density and shortpass filters. Inset: schematics of the employed hybrid CARS technique.

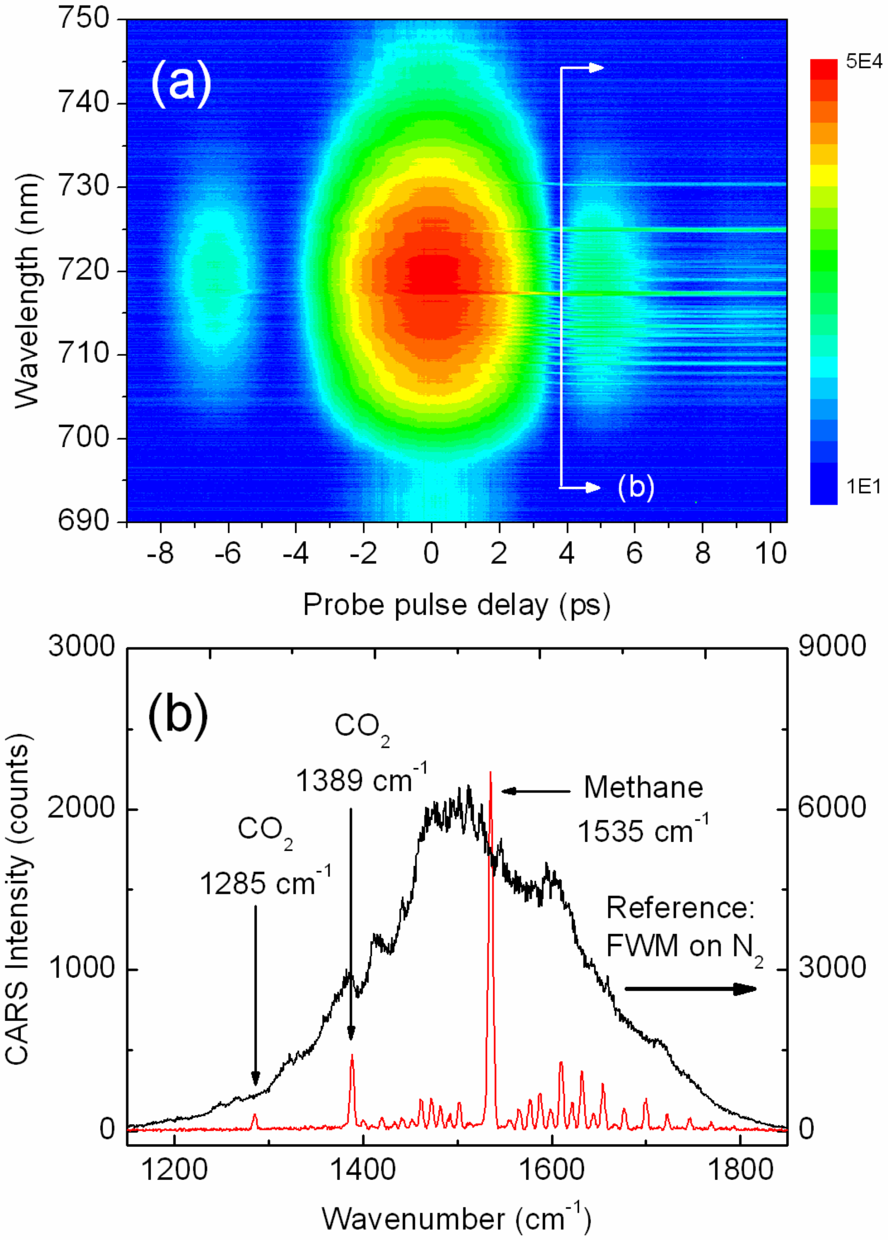

Fig. 9.4. Hybrid CARS on natural gas. (a) CARS spectrogram obtained on a gravimetrically prepared gas mixture, mimicking natural gas composition. (b) Cross-section of the recorded spectrogram. Pulse parameters are: pump - λ_1 = 1.27 μm, 3.0 μJ/pulse; Stokes - λ_2 = 1.59 μm, 2.0 μJ/pulse; probe - λ_3 = 806 nm, $\Delta\nu_3 \approx 7$ cm^{-1}, 0.37 μJ/pulse. The collinear beams are focused with a 20-cm focal length lens into about 10-cm long cell, filled with the gas mixture at the atmospheric pressure. The reference FWM spectrum is obtained on N_2 vapor. The integration time is 0.2 s.

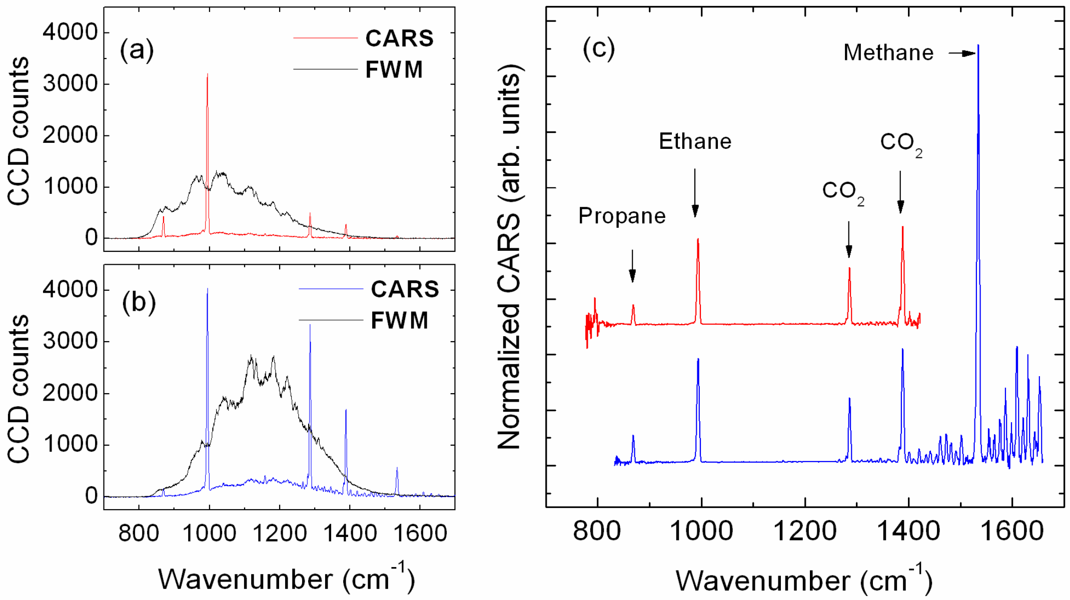

Fig. 9.5. CARS spectra normalization. (a,b) CARS spectra acquired on the gas mixture for two slightly different time delays between the pump and Stokes pulses. The excitation band shifts due to the chirp of the preparation pulses. The reference FWM spectra are obtained with the same samples but negative probe delay, when the first oscillation peak of the sinc^2-shaped probe pulse is overlapped with the other two laser pulses. The resonant contribution is negligible here; (c) CARS spectra from (a) and (b) normalized on the reference FWM profiles.

REFERENCES

1. A. Fasanella, S. Losito, R. Adone, F. Ciuchini, T. Trotta, S. A. Altamura, D. Chiocco, and G. Ippolito, "PCR assay to detect Bacillus anthracis spores in heat-treated specimens," Journal of Clinical Microbiology **41**, 896-899 (2003).

2. D. King, V. Luna, A. Cannons, J. Cattani, and P. Amuso, "Performance assessment of three commercial assays for direct detection of Bacillus anthracis spores," Journal of Clinical Microbiology **41**, 3454-3455 (2003).

3. J. F. Powell, "Isolation of dipicolinic acid (pyridine-2-6-dicarboxylic acid) from spores of Bacillus-megatherium," Biochemical Journal **54**, 210-211 (1953).

4. B. D. Church and H. Halvorson, "Dependence of the heat resistance of bacterial endospores on their dipicolinic acid content," Nature **183**, 124-125 (1959).

5. P. M. Pellegrino, N. F. Fell, and J. B. Gillespie, "Enhanced spore detection using dipicolinate extraction techniques," Analytica Chimica Acta **455**, 167-177 (2002).

6. P. Carmona, "Vibrational-spectra and structure of crystalline dipicolinic acid and calcium dipicolinate trihydrate," Spectrochimica Acta Part a-Molecular and Biomolecular Spectroscopy **36**, 705-712 (1980).

7. A. P. Esposito, C. E. Talley, T. Huser, C. W. Hollars, C. M. Schaldach, and S. M. Lane, "Analysis of single bacterial spores by micro-Raman spectroscopy," Applied Spectroscopy **57**, 868-871 (2003).

8. E. Ghiamati, R. Manoharan, W. H. Nelson, and J. F. Sperry, "UV resonance Raman-spectra of Bacillus spores," Applied Spectroscopy **46**, 357-364 (1992).

9. S. Farquharson, L. Grigely, V. Khitrov, W. Smith, J. F. Sperry, and G. Fenerty, "Detecting Bacillus cereus spores on a mail sorting system using Raman spectroscopy," Journal of Raman Spectroscopy **35**, 82-86 (2004).

10. C. L. Haynes, C. R. Yonzon, X. Y. Zhang, and R. P. Van Duyne, "Surface-enhanced Raman sensors: early history and the development of sensors for quantitative biowarfare agent and glucose detection," Journal of Raman Spectroscopy **36**, 471-484 (2005).

11. X. Y. Zhang, M. A. Young, O. Lyandres, and R. P. Van Duyne, "Rapid detection of an anthrax biomarker by surface-enhanced Raman spectroscopy," Journal of the American Chemical Society **127**, 4484-4489 (2005).

12. R. M. Jarvis and R. Goodacre, "Discrimination of bacteria using surface-enhanced Raman spectroscopy," Analytical Chemistry **76**, 40-47 (2004).

13. W. M. Tolles and R. D. Turner, "Comparative analysis of analytical capabilities of coherent anti-Stokes Raman-spectroscopy (CARS) relative to Raman-scattering and absorption spectroscopy," Applied Spectroscopy **31**, 96-103 (1977).

14. W. M. Tolles, J. W. Nibler, J. R. Mcdonald, and A. B. Harvey, "Review of theory and application of coherent anti-Stokes Raman-spectroscopy (CARS)," Applied Spectroscopy **31**, 253-271 (1977).

15. Y. R. Shen, *The principles of nonlinear optics* (John Wiley & Sons, Inc., 2003).

16. J. L. Oudar, R. W. Smith, and Y. R. Shen, "Polarization-sensitive coherent anti-Stokes Raman-spectroscopy," Applied Physics Letters **34**, 758-760 (1979).

17. Y. Yacoby, R. Fitzgibbon, and B. Lax, "Coherent cancellation of background in 4-wave mixing spectroscopy," Journal of Applied Physics **51**, 3072-3077 (1980).

18. E. O. Potma, C. L. Evans, and X. S. Xie, "Heterodyne coherent anti-Stokes Raman scattering (CARS) imaging," Optics Letters **31**, 241-243 (2006).

19. D. Oron, N. Dudovich, D. Yelin, and Y. Silberberg, "Quantum control of coherent anti-Stokes Raman processes," Physical Review A **65**, 043408 (2002).

20. D. Oron, N. Dudovich, D. Yelin, and Y. Silberberg, "Narrow-band coherent anti-stokes Raman signals from broad-band pulses," Physical Review Letters **88**, 063004 (2002).

21. S. H. Lim, A. G. Caster, and S. R. Leone, "Single-pulse phase-control interferometric coherent anti-Stokes Raman scattering spectroscopy," Physical Review A **72**, 041803 (2005).

22. T. W. Kee, H. X. Zhao, and M. T. Cicerone, "One-laser interferometric broadband coherent anti-Stokes Raman scattering," Optics Express **14**, 3631-3640 (2006).

23. R. Leonhardt, W. Holzapfel, W. Zinth, and W. Kaiser, "Terahertz quantum beats in molecular liquids," Chem Phys Lett **133**, 373-377 (1987).

24. M. Schmitt, G. Knopp, A. Materny, and W. Kiefer, "Femtosecond time-resolved coherent anti-Stokes Raman scattering for the simultaneous study of ultrafast ground and excited state dynamics: Iodine vapour," Chem Phys Lett **270**, 9-15 (1997).

25. M. O. Scully, G. W. Kattawar, R. P. Lucht, T. Opatrny, H. Pilloff, A. Rebane, A. V. Sokolov, and M. S. Zubairy, "FAST CARS: Engineering a laser spectroscopic technique for rapid identification of bacterial spores," P Natl Acad Sci USA **99**, 10994-11001 (2002).

26. D. Pestov, R. K. Murawski, G. O. Ariunbold, X. Wang, M. C. Zhi, A. V. Sokolov, V. A. Sautenkov, Y. V. Rostovtsev, A. Dogariu, Y. Huang, and M. O. Scully, "Optimizing the laser-pulse configuration for coherent Raman spectroscopy," Science **316**, 265-268 (2007).

27. B. D. Prince, A. Chakraborty, B. M. Prince, and H. U. Stauffer, "Development of simultaneous frequency- and time-resolved coherent anti-Stokes Raman scattering for ultrafast detection of molecular Raman spectra," J Chem Phys **125**, 044502 (2006).

28. A. A. Kolomenskii and H. A. Schuessler, "Raman spectra of dipicolinic acid in crystalline and liquid environments," Spectrochimica Acta Part A-Molecular and Biomolecular Spectroscopy **61**, 647-651 (2005).

29. D. Pestov, M. H. Zhi, Z. E. Sariyanni, N. G. Kalugin, A. Kolomenskii, R. Murawski, Y. V. Rostovtsev, V. A. Sautenkov, A. V. Sokolov, and M. O. Scully, "Femtosecond CARS of methanol-water mixtures," Journal of Raman Spectroscopy **37**, 392-396 (2006).

30. B. Schrader and W. Meier, *Raman/IR atlas of organic compounds* (Weinheim, 1977), Vol. 1.

31. L. Dougan, S. P. Bates, R. Hargreaves, J. P. Fox, J. Crain, J. L. Finney, V. Reat, and A. K. Soper, "Methanol-water solutions: A bi-percolating liquid mixture," J Chem Phys **121**, 6456-6462 (2004).

32. A. Materny, T. Chen, M. Schmitt, T. Siebert, A. Vierheilig, V. Engel, and W. Kiefer, "Wave packet dynamics in different electronic states investigated by femtosecond time-resolved four-wave-mixing spectroscopy," Applied Physics B-Lasers and Optics **71**, 299-317 (2000).

33. W. Kiefer, A. Materny, and M. Schmitt, "Femtosecond time-resolved spectroscopy of elementary molecular dynamics," Naturwissenschaften **89**, 250-258 (2002).

34. M. Fickenscher and A. Laubereau, "High-precision femtosecond CARS of simple liquids," Journal of Raman Spectroscopy **21**, 857-861 (1990).

35. M. Fickenscher, H. G. Purucker, and A. Laubereau, "Resonant vibrational dephasing investigated by high-precision femtosecond CARS," Chem Phys Lett **191**, 182-188 (1992).

36. H. Okamoto and K. Yoshihara, "Femtosecond time-resolved coherent Raman-scattering from beta-Carotene in solution - Ultrahigh frequency (11-Thz) beating phenomenon and subpicosecond vibrational-relaxation," Chem Phys Lett **177**, 568-572 (1991).

37. T. Joo and A. C. Albrecht, "Femtosecond time-resolved coherent anti-Stokes-Raman spectroscopy of liquid benzene - a Kubo relaxation function-analysis," J Chem Phys **99**, 3244-3251 (1993).

38. T. Lang, K. L. Kompa, and M. Motzkus, "Femtosecond CARS on H-2," Chem Phys Lett **310**, 65-72 (1999).

39. A. Fendt, S. F. Fischer, and W. Kaiser, "Vibrational lifetime and Fermi resonance in polyatomic-molecules," Chemical Physics **57**, 55-64 (1981).

40. L. K. Iwaki and D. D. Dlott, "Ultrafast vibrational energy redistribution within C-H and O-H stretching modes of liquid methanol," Chem Phys Lett **321**, 419-425 (2000).

41. Y. Huang, A. Dogariu, Y. Avitzour, R. K. Murawski, D. Pestov, M. C. Zhi, A. V. Sokolov, and M. O. Scully, "Discrimination of dipicolinic acid and its interferents by femtosecond coherent Raman spectroscopy," Journal of Applied Physics **100**, 124912 (2006).

42. M. C. Zhi, D. Pestov, X. Wang, R. K. Murawski, Y. V. Rostovtsev, Z. E. Sariyanni, V. A. Sautenkov, N. G. Kalugin, and A. V. Sokolov, "Concentration dependence of femtosecond coherent anti-Stokes Raman scattering in the presence of strong absorption," Journal of the Optical Society of America B-Optical Physics **24**, 1181-1186 (2007).

43. J. A. Shirley, R. J. Hall, and A. C. Eckbreth, "Folded boxcars for rotational Raman studies," Optics Letters **5**, 380-382 (1980).

44. National Institute of Standards and Technology (NIST), Standard Reference Database (http://webbook.nist.gov/chemistry/).

45. D. Pestov, M. C. Zhi, Z. E. Sariyanni, N. G. Kalugin, A. A. Kolomenskii, R. Murawski, G. G. Paulus, V. A. Sautenkov, H. Schuessler, A. V. Sokolov, G. R.

Welch, Y. V. Rostovtsev, T. Siebert, D. A. Akimov, S. Graefe, W. Kiefer, and M. O. Scully, "Visible and UV coherent Raman spectroscopy of dipicolinic acid," P Natl Acad Sci USA **102**, 14976-14981 (2005).

46. T. V. Inglesby, T. O'Toole, D. A. Henderson, J. G. Bartlett, M. S. Ascher, E. Eitzen, A. M. Friedlander, J. Gerberding, J. Hauer, J. Hughes, J. McDade, M. T. Osterholm, G. Parker, T. M. Perl, P. K. Russell, and K. Tonat, "Anthrax as a biological weapon, 2002 - Updated recommendations for management," Journal of the American Medical Association **287**, 2236-2252 (2002).

47. D. Meshulach and Y. Silberberg, "Coherent quantum control of multiphoton transitions by shaped ultrashort optical pulses," Physical Review A **60**, 1287-1292 (1999).

48. A. Assion, T. Baumert, M. Bergt, T. Brixner, B. Kiefer, V. Seyfried, M. Strehle, and G. Gerber, "Control of chemical reactions by feedback-optimized phase-shaped femtosecond laser pulses," Science **282**, 919-922 (1998).

49. V. V. Lozovoy, B. I. Grimberg, E. J. Brown, I. Pastirk, and M. Dantus, "Femtosecond spectrally dispersed three-pulse four-wave mixing: the role of sequence and chirp in controlling intramolecular dynamics," Journal of Raman Spectroscopy **31**, 41-49 (2000).

50. R. A. Bartels, T. C. Weinacht, S. R. Leone, H. C. Kapteyn, and M. M. Murnane, "Nonresonant control of multimode molecular wave packets at room temperature," Physical Review Letters **88**, 033001 (2002).

51. N. Dudovich, D. Oron, and Y. Silberberg, "Single-pulse coherently controlled nonlinear Raman spectroscopy and microscopy," Nature **418**, 512-514 (2002).

52. D. Oron, N. Dudovich, and Y. Silberberg, "Femtosecond phase-and-polarization control for background-free coherent anti-Stokes Raman spectroscopy," Physical Review Letters **90**, 213902 (2003).

53. A. M. Zheltikov and A. N. Naumov, "High-resolution four-photon spectroscopy with chirped pulses," Quantum Electronics **30**, 606-610 (2000).

54. A. S. Weling, B. B. Hu, N. M. Froberg, and D. H. Auston, "Generation of tunable narrow-band THz radiation from large-aperture photoconducting antennas," Applied Physics Letters **64**, 137-139 (1994).

55. E. Gershgoren, R. A. Bartels, J. T. Fourkas, R. Tobey, M. M. Murnane, and H. C. Kapteyn, "Simplified setup for high-resolution spectroscopy that uses ultrashort pulses," Optics Letters **28**, 361-363 (2003).

56. T. Hellerer, A. M. K. Enejder, and A. Zumbusch, "Spectral focusing: High spectral resolution spectroscopy with broad-bandwidth laser pulses," Applied Physics Letters **85**, 25-27 (2004).

57. G. W. Jones, D. L. Marks, C. Vinegoni, and S. A. Boppart, "High-spectral-resolution coherent anti-Stokes Raman scattering with interferometric ally detected broadband chirped pulses," Optics Letters **31**, 1543-1545 (2006).

58. D. Pestov, X. Wang, R. K. Murawski, G. O. Ariunbold, V. A. Sautenkov, and A. V. Sokolov, "Pulse shaping for mode-selective ultrafast coherent Raman spectroscopy of highly scattering solids," submitted to J. Opt. Soc. Am. B (2007).

59. A. E. Siegman, *Lasers* (University Science Books, 1986).

60. V. V. Lozovoy, I. Pastirk, and M. Dantus, "Multiphoton intrapulse interference. IV. Ultrashort laser pulse spectral phase characterization and compensation," Optics Letters **29**, 775-777 (2004).

61. B. W. Xu, J. M. Gunn, J. M. Dela Cruz, V. V. Lozovoy, and M. Dantus, "Quantitative investigation of the multiphoton intrapulse interference phase scan method for simultaneous phase measurement and compensation of femtosecond laser pulses," Journal of the Optical Society of America B-Optical Physics **23**, 750-759 (2006).

62. C. L. Evans, E. O. Potma, and X. S. Xie, "Coherent anti-Stokes Raman scattering spectral interferometry: determination of the real and imaginary components of nonlinear susceptibility $\chi(3)$ for vibrational microscopy," Optics Letters **29**, 2923-2925 (2004).

63. S. H. Lim, A. G. Caster, O. Nicolet, and S. R. Leone, "Chemical imaging by single pulse interferometric coherent anti-Stokes Raman scattering microscopy," J Phys Chem B **110**, 5196-5204 (2006).

64. D. Pestov, X. Wang, G. O. Ariunbold, R. K. Murawski, V. A. Sautenkov, A. Dogariu, A. V. Sokolov, and M. O. Scully, "Single-shot detection of bacterial endospores via coherent Raman spectroscopy," submitted to Proc. Natl. Acad. Sci. (2007).

65. N. Dudovich, D. Oron, and Y. Silberberg, "Single-pulse coherent anti-Stokes Raman spectroscopy in the fingerprint spectral region," J Chem Phys **118**, 9208-9215 (2003).

66. H. Kano and H. Hamaguchi, "Dispersion-compensated supercontinuum generation for ultrabroadband multiplex coherent anti-Stokes Raman scattering spectroscopy," Journal of Raman Spectroscopy **37**, 411-415 (2006).

67. S. Roy, T. R. Meyer, and J. R. Gord, "Time-resolved dynamics of resonant and nonresonant broadband picosecond coherent anti-Stokes Raman scattering signals," Applied Physics Letters **87**, 264103 (2005).

68. P. R. Regnier and J. P. E. Taran, "Possibility of measuring gas concentrations by stimulated anti-Stokes scattering," Applied Physics Letters **23**, 240-242 (1973).

69. P. Beaud, H. M. Frey, T. Lang, and M. Motzkus, "Flame thermometry by femtosecond CARS," Chem Phys Lett **344**, 407-412 (2001).

70. S. Roy, W. D. Kulatilaka, S. V. Naik, N. M. Laurendeau, R. P. Lucht, and J. R. Gord, "Effects of quenching on electronic-resonance-enhanced coherent anti-Stokes Raman scattering of nitric oxide," Applied Physics Letters **89**, 104105 (2006).

71. M. D. Duncan, J. Reintjes, and T. J. Manuccia, "Scanning coherent anti-Stokes Raman microscope," Optics Letters **7**, 350-352 (1982).

72. A. Zumbusch, G. R. Holtom, and X. S. Xie, "Three-dimensional vibrational imaging by coherent anti-Stokes Raman scattering," Physical Review Letters **82**, 4142-4145 (1999).

73. A. Voroshilov, C. Otto, and J. Greve, "On the coherent vibrational phase in polarization sensitive resonance CARS spectroscopy of copper tetraphenylporphyrin," J Chem Phys **106**, 2589-2598 (1997).

74. H. Kano and H. Hamaguchi, "Femtosecond coherent anti-Stokes Raman scattering spectroscopy using supercontinuum generated from a photonic crystal fiber," Applied Physics Letters **85**, 4298-4300 (2004).

75. G. I. Petrov and V. V. Yakovlev, "Enhancing red-shifted white-light continuum generation in optical fibers for applications in nonlinear Raman microscopy," Optics Express **13**, 1299-1306 (2005).

76. R. P. Lucht, S. Roy, T. R. Meyer, and J. R. Gord, "Femtosecond coherent anti-Stokes Raman scattering measurement of gas temperatures from frequency-spread dephasing of the Raman coherence," Applied Physics Letters **89**, 251112 (2006).

77. X. N. Wen, S. Chen, and D. D. Dlott, "Time-resolved 3-color coherent Raman-scattering applied to polycrystalline and opaque solids," Journal of the Optical Society of America B-Optical Physics **8**, 813-819 (1991).

78. M. Muller and J. M. Schins, "Imaging the thermodynamic state of lipid membranes with multiplex CARS microscopy," J Phys Chem B **106**, 3715-3723 (2002).

79. J. X. Cheng, A. Volkmer, and X. S. Xie, "Theoretical and experimental characterization of coherent anti-Stokes Raman scattering microscopy," Journal of the Optical Society of America B-Optical Physics **19**, 1363-1375 (2002).

80. H. A. Rinia, M. Bonn, and M. Muller, "Quantitative multiplex CARS spectroscopy in congested spectral regions," J Phys Chem B **110**, 4472-4479 (2006).

81. K. P. Knutsen, J. C. Johnson, A. E. Miller, P. B. Petersen, and R. J. Saykally, "High spectral resolution multiplex CARS spectroscopy using chirped pulses," Chem Phys Lett **387**, 436-441 (2004).

82. W. H. Nelson, R. Dasari, M. Feld, and J. F. Sperry, "Intensities of calcium dipicolinate and Bacillus subtilis spore Raman spectra excited with 244 nm light," Applied Spectroscopy **58**, 1408-1412 (2004).

83. G. I. Petrov, V. V. Yakovlev, A. V. Sokolov, and M. O. Scully, "Detection of Bacillus subtilis spores in water by means of broadband coherent anti-Stokes Raman spectroscopy," Optics Express **13**, 9537-9542 (2005).

84. J. W. Nibler and G. V. Knighten, *Coherent anti-Stokes Raman specroscopy*, Raman spectroscopy of gases and liquids (Springer-Verlag, 1979).

85. A. Volkmer, L. D. Book, and X. S. Xie, "Time-resolved coherent anti-Stokes Raman scattering microscopy: Imaging based on Raman free induction decay," Applied Physics Letters **80**, 1505-1507 (2002).

86. D. Pestov, G. O. Ariunbold, X. Wang, R. K. Murawski, V. A. Sautenkov, A. V. Sokolov, and M. O. Scully, "Coherent versus incoherent Raman scattering: molecular coherence excitation and measurement," Optics Letters **32**, 1725-1727 (2007).

87. G. I. Petrov, R. Arora, V. V. Yakovlev, X. Wang, A. V. Sokolov, and M. O. Scully, "Comparison of coherent and spontaneous Raman microspectroscopies for noninvasive detection of single bacterial endospores," P Natl Acad Sci USA **104**, 7776-7779 (2007).

88. A. Dogariu, Y. Huang, D. Pestov, R. K. Murawski, A. V. Sokolov, and M. O. Scully, "Real-time detection of bacterial spores," in *Conference on Lasers and Electro-Optics/Quantum Electronics and Laser Science Conference and*

Photonic Applications Systems Technologies, OSA Technical Digest Series (CD) (Optical Society of America, 2007), CPDA1.

89. C. L. Evans, E. O. Potma, M. Puoris'haag, D. Cote, C. P. Lin, and X. S. Xie, "Chemical imaging of tissue in vivo with video-rate coherent anti-Stokes Raman scattering microscopy," P Natl Acad Sci USA **102**, 16807-16812 (2005).

90. J. P. Ogilvie, E. Beaurepaire, A. Alexandrou, and M. Joffre, "Fourier-transform coherent anti-Stokes Raman scattering microscopy," Optics Letters **31**, 480-482 (2006).

APPENDIX A

ABSORPTION CROSS-SECTION FOR NaDPA IN SOLUTION

The absorption cross section dependence on the wavelength is derived from the transmission measurements on 25 and 50 mM solutions of NaDPA in water within the UV tuning range of the available OPA (Coherent, OperA-SFG/UV). Photodetectors (DET210, Thorlabs) are used to measure the laser pulse energy before and after the sample. The results are summarized in Fig. A-1. The resolution is determined by the spectral bandwidth of the laser pulse. Its typical spectrum is shown by the dashed line. The solid line in Fig. A-1 is a result of a spectrophotometric measurement on a sample of NaDPA solution with an unknown concentration. It is scaled along the vertical axis to match the data obtained in the experiments with known concentrations. The close agreement between the transmission experiments with femtosecond pulses and spectrophotometric measurements supports our assumption of linear absorption, i.e. that the Beer's law is valid. The absorption cross section α is determined by the formula

$$\alpha = -\frac{\ln(T)}{Nd}, \tag{A.1}$$

where T is the transmission, d is the interaction length, and N is the concentration of DPA in the solution.

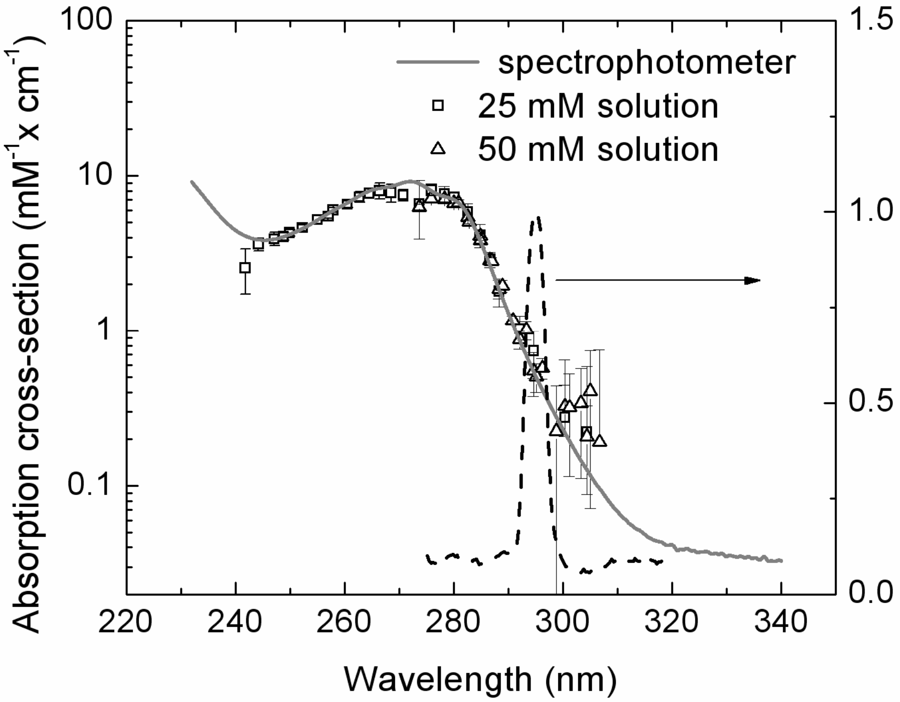

Fig. A-1. Absorption cross-section of NaDPA solution in the UV range and the spectrum of the probe pulse (dashed curve). The absorption cross-section dependence on the wavelength is derived from transmission measurements on 25 mM (square) and 50 mM (triangle) NaDPA solutions. The solid curve is a scaled result from spectrophotometric measurements. [42]

APPENDIX B
REFRACTIVE INDEX MEASUREMENT ON 50 mM AND 100 mM NaDPA SOLUTIONS

The index of refraction for NaDPA solution in the UV spectral range is deduced from comparative refraction measurements on pure water and the solution. Briefly, a laser beam is sent across a right corner of a quartz cuvette (with a square cross-section, 1 cm×1 cm), filled with water or NaDPA solution. The refracted beam is projected onto a screen about 3 meters away from the sample. Obviously, the output angle, and therefore the beam position on the screen, depends on the index of refraction of water or the solution to be measured. From the known refractive index of water (see X. Quan and E.S. Fry, *Appl. Opt.* **34**, 3477-3480 (1995)) and the recorded beam positions on the screen for water, 50 mM, and 100 mM NaDPA solutions, the indices of refraction for the two NaDPA concentrations are calculated. The results are summarized in Fig. B-1. Note that the relative error of our measurements is small, and is roughly represented by the size of the symbols (squares, triangles, and circles) for the data points. However there is the uncertainty for the used index of refraction of water. This uncertainty translates into the absolute errors for the deduced values of NaDPA refractive index.

We fit the data with an expansion similar to the empirical equation for the refractive index of water, given in the reference above. The fitting curves are shown in Fig. B-1 (dashed curve, 50 mM; dotted curve, 100 mM). The corresponding equation for the refractive index of 50 mM NaDPA solution is

$$n(\lambda) = 1.31279 + \frac{59.8991}{\lambda} - \frac{30562.7}{\lambda^2} + \frac{5.11903\times10^6}{\lambda^3}. \tag{B.1}$$

For the 100 mM solution, it is

$$n(\lambda) = 1.31279 + \frac{65.8283}{\lambda} - \frac{35024.0}{\lambda^2} + \frac{6.03199\times10^6}{\lambda^3}. \tag{B.2}$$

Here the wavelength λ is measured in nanometers.

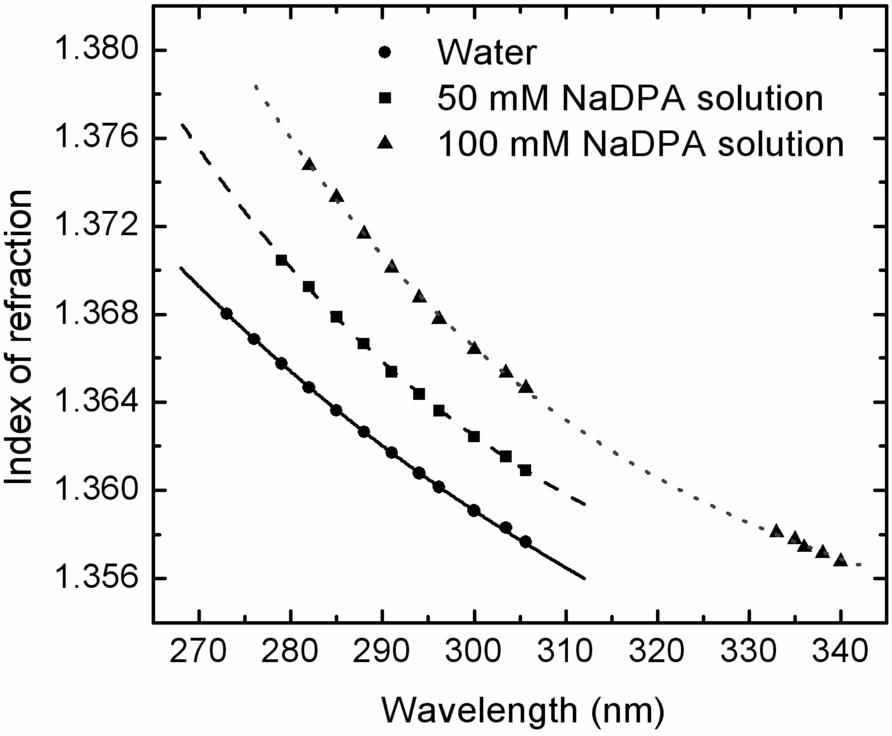

Fig. B-1. Index of refraction of 50 and 100 mM NaDPA solution in UV range. Dashed curve, a fitting curve for 50 mM NaDPA solution derived from Eq. B1; dotted curve, a fitting curve for 100 mM NaDPA solution derived from Eq. B2; solid curve, a fitting curve from the empirical equation for pure water (X. Quan and E.S. Fry, *Appl. Opt.* **34**, 3477-3480 (1995)). [42]

APPENDIX C
THREE-LEVEL MODEL FOR COHERENT RAMAN SCATTERING OF NEAR-RESONANT PROBE PULSE

The material presented here is reproduced with minor modifications from D. Pestov *et al.*, Proc. Natl. Acad. Sci. U.S.A. **102**, 14976-14981 (2005).

In a time-delayed CARS scheme, the pump and Stokes pulses are applied first and initiate a coherent vibrational motion of the medium described by the ρ_{bc} density matrix element. A probe pulse, applied after some time delay, scatters off that coherence to generate the CARS signal. Within a simplified three-level model (refer to the level diagram in Fig. 4.17), the equations of motion that describe the preparation of the ρ_{bc} coherence by the first two pulses are

$$\begin{aligned}
\dot{\rho}_{ab} &= -(i\omega_{ab} + \gamma_{ab})\rho_{ab} - i\Omega_1 e^{-i\omega_1 t}\rho_{bc}^{*} + i\Omega_2 e^{-i\omega_2 t} n_{ab}, \\
\dot{\rho}_{ac} &= -(i\omega_{ac} + \gamma_{ac})\rho_{ac} - i\Omega_2 e^{-i\omega_2 t}\rho_{bc} + i\Omega_1 e^{-i\omega_1 t} n_{ac}, \\
\dot{\rho}_{bc} &= -(i\omega_{bc} + \gamma_{bc})\rho_{bc} + i\Omega_1 e^{-i\omega_1 t}\rho_{ab}^{*} - i\Omega_2^{*} e^{i\omega_2 t}\rho_{ac},
\end{aligned} \tag{C.1}$$

where $n_{ab} = \rho_{aa} - \rho_{bb}$, $n_{ac} = \rho_{aa} - \rho_{cc}$ are the population inversions and

$$\Omega_1 = -\frac{\wp_{ac} E_1}{2\hbar},\ \Omega_2 = -\frac{\wp_{ab} E_2}{2\hbar} \tag{C.2}$$

are the Rabi frequencies of the pump and Stokes fields, respectively. By setting $\rho_{ac} = \tilde{\rho}_{ac} e^{-i\omega_1 t}$, $\rho_{ab} = \tilde{\rho}_{ab} e^{-i\omega_2 t}$, and $\rho_{bc} = \tilde{\rho}_{bc} e^{-i(\omega_1 - \omega_2)t}$, the equations of motion become

$$\begin{aligned}
\dot{\tilde{\rho}}_{ab} &= -\Gamma_{ab}\tilde{\rho}_{ab} - i\Omega_1\tilde{\rho}_{bc}^{*} + i\Omega_2 n_{ab}, \\
\dot{\tilde{\rho}}_{ac} &= -\Gamma_{ac}\tilde{\rho}_{ac} - i\Omega_2\tilde{\rho}_{bc} + i\Omega_1 n_{ac}, \\
\dot{\tilde{\rho}}_{bc} &= -\Gamma_{bc}\tilde{\rho}_{bc} + i\Omega_1\tilde{\rho}_{ab}^{*} - i\Omega_2^{*}\tilde{\rho}_{ac},
\end{aligned} \tag{C.3}$$

where $\Gamma_{ac} = i(\omega_{ac} - \omega_1) + \gamma_{ac}$, $\Gamma_{ab} = i(\omega_{ab} - \omega_2) + \gamma_{ab}$, and $\Gamma_{bc} = \gamma_{bc}$. From the equations above, we obtain in steady-state regime:

$$\tilde{\rho}_{bc} = \frac{\dfrac{n_{ab}}{\Gamma_{ab}^*} + \dfrac{n_{ac}}{\Gamma_{ac}}}{\Gamma_{bc} + \dfrac{|\Omega_1|^2}{\Gamma_{ab}^*} + \dfrac{|\Omega_2|^2}{\Gamma_{ac}}} \Omega_1 \Omega_2^*, \tag{C.4}$$

and for optical pulses strongly detuned from the electronic transition and shorter than the vibrational relaxation rate

$$|\rho_{bc}| = |\tilde{\rho}_{bc}| = |\Omega_1 \Omega_2^* / \Delta| \tau, \tag{C.5}$$

where τ is the duration of pump and Stokes pulses, and Δ is the detuning.

When the probe pulse is applied, after some time delay, it drives that coherence to generate polarization P in the lasing transition $|a> \leftrightarrow |c>$ (consider CARS generation only), corresponding to the density matrix element ρ_{ac}. Specifically, the polarization is $P = N\wp_{ac}\rho_{ac}$, where $\wp_{ac}$ is the dipole moment of the lasing transition and N is the particle density. The polarization generates the signal pulse as described by Maxwell's equations. With the phase matching condition fulfilled, the signal amplification is governed by

$$\frac{\partial E_{CARS}}{\partial z} = i \frac{\omega_{CARS} N \wp_{ac}}{2\varepsilon_0 c} \tilde{\rho}_{ac}. \tag{C.6}$$

The equations of motion for slowly-varying coherence amplitudes are

$$\begin{aligned} \dot{\tilde{\rho}}_{ab} &= -\hat{\Gamma}_{ab}\tilde{\rho}_{ab} - i\Omega_{CARS}\tilde{\rho}_{bc}^* + i\Omega_3 n_{ab}, \\ \dot{\tilde{\rho}}_{ac} &= -\hat{\Gamma}_{ac}\tilde{\rho}_{ac} - i\Omega_3\tilde{\rho}_{bc} + i\Omega_{CARS} n_{ac}, \\ \dot{\tilde{\rho}}_{bc} &= -\Gamma_{bc}\tilde{\rho}_{bc} + i\Omega_{CARS}\tilde{\rho}_{ab}^* - i\Omega_3^*\tilde{\rho}_{ac}, \end{aligned} \tag{C.7}$$

where now $\hat{\Gamma}_{ac} = i(\omega_{ac} - \omega_{CARS}) + \gamma_{ac}$, $\hat{\Gamma}_{ab} = i(\omega_{ab} - \omega_3) + \gamma_{ab}$, $\Gamma_{bc} = \gamma_{bc}$, and

$$\Omega_3 = -\frac{\wp_{ab} E_3}{2\hbar}, \; \Omega_{CARS} = -\frac{\wp_{ac} E_{CARS}}{2\hbar} \tag{C.8}$$

are the Rabi frequencies of the probe and CARS fields.

From the equation for $\tilde{\rho}_{ac}$ in the steady state and for $\Omega_{CARS}^0 \approx 0$ we get

$$\tilde{\rho}_{ac} \approx -i \frac{\Omega_3}{\hat{\Gamma}_{ac}} \tilde{\rho}_{bc} = i \frac{\wp_{ab} E_3}{2\hbar(i(\omega_{ac} - \omega_{CARS}) + \gamma_{ac})} \tilde{\rho}_{bc}. \tag{C.9}$$

Hence, Eq. C.6 becomes

$$\frac{\partial E_{CARS}}{\partial z} = -\frac{\omega_{CARS} N \wp_{ab} \wp_{ac}}{4\varepsilon_0 \hbar c} \frac{\tilde{\rho}_{bc}}{(i(\omega_{ac} - \omega_{CARS}) + \gamma_{ac})} E_3. \tag{C.10}$$

For simplicity let us write $\omega_{CARS} / c = 2\pi / \lambda_{CARS}$, $\omega_{ac} - \omega_{CARS} = \Delta_{CARS}$, and integrate the above equation over the interaction length L to get

$$\frac{E_{CARS}}{E_3} = -\frac{\pi N L \wp_{ab} \wp_{ac}}{2\hbar \varepsilon_0 \lambda_{CARS}} \frac{\tilde{\rho}_{bc}}{i\Delta_{CARS} + \gamma_{ac}}, \tag{C.11}$$

thus

$$\frac{I_{CARS}}{I_3} = \left| \frac{E_{CARS}}{E_3} \right|^2 = \left(\frac{\pi N L |\tilde{\rho}_{bc}|}{2\hbar \varepsilon_0 \lambda_{CARS}} \right)^2 \frac{|\wp_{ab}|^2 |\wp_{ac}|^2}{\Delta_{CARS}^2 + \gamma_{ac}^2}. \tag{C.12}$$

The average intensity of a laser pulse in the focus can be expressed as

$$I = \hbar\omega \frac{n}{\tau A} = \frac{2\pi \hbar c n}{\tau A \lambda}, \tag{C.13}$$

where A is the beam cross-section area in the focal point, τ is its time length, and n is the number of photons in a single laser pulse. Therefore, for the ratio of CARS and probe photon numbers one gets

$$\frac{n_{CARS}}{n_3} \approx \left(\frac{\pi N L |\tilde{\rho}_{bc}|}{2\hbar \varepsilon_0} \right)^2 \frac{|\wp_{ab}|^2 |\wp_{ac}|^2}{\lambda_3 \lambda_{CARS}} \frac{1}{\Delta_{CARS}^2 + \gamma_{ac}^2}. \tag{C.14}$$

In the same manner, an expression for CSRS and probe photon number ratio can be derived to give

$$\frac{n_{CSRS}}{n_3} \approx \left(\frac{\pi N L |\tilde{\rho}_{bc}|}{2\hbar \varepsilon_0} \right)^2 \frac{|\wp_{ab}|^2 |\wp_{ac}|^2}{\lambda_3 \lambda_{CSRS}} \frac{1}{\Delta_{CSRS}^2 + \gamma_{ab}^2}. \tag{C.15}$$

A subtle difference between CARS and CSRS processes comes in through the phenomenological decay rate constants, γ_{ac} and γ_{ab}, which account for the width of the electronic resonance and might in principle differ.

APPENDIX D

THE RATIO OF COHERENT TO SPONTANEOUS RAMAN SIGNALS

The material presented here is reproduced with minor modifications from G.I. Petrov *et al.*, Proc. Natl. Acad. Sci. U.S.A. **104**, 7776-7779 (2007).

To quantify the difference between CARS and spontaneous Raman scattering, we calculate the number of detected photons for coherent (directional) CARS and incoherent (spherical) spontaneous Raman processes. We write the interaction Hamiltonian as

$$\Lambda(t) = \sum_j G_{43}(|c><b|)_j\, \hat{a}_4^+ \hat{a}_3\, e^{i(\omega_4-\omega_3-\omega_{bc})t - i(\vec{k}_4-\vec{k}_3)\vec{r}_j} + adj. \qquad \text{(D.1)}$$

We proceed by using Eq. D.1 to write the equation of motion for the annihilation operator $\hat{a}_4$ and integrating to obtain

$$\hat{a}_4 = -\frac{i}{\hbar}\sum_j \frac{G_{43}\hat{a}_3}{i\Delta\omega_{43}}(|c><b|)_j\, e^{-i(\vec{k}_4-\vec{k}_3)\vec{r}_j}, \qquad \text{(D.2)}$$

where $\Delta\omega_{43} = \omega_4 - \omega_3 - \omega_{bc} + i\gamma_{bc}$, and G_{43} represents the molecular-photon coupling constant. The average of the CARS photon number operator is then given by

$$<\hat{n}_4>=<\psi|\hat{a}_4^+\hat{a}_4|\psi>, \qquad \text{(D.3)}$$

where the system state vector is

$$|\psi>=|\alpha_3, 0_4>\prod_j |\phi_j>, \qquad \text{(D.4)}$$

for the case in which the anti-Stokes field is originally in the vacuum state, the probe field is in the Glauber coherent state α_3 and the *j*-th molecule is in the state

$$|\phi_j>=C_j|c>+B_j|b>, \qquad \text{(D.5)}$$

i.e. in a coherent superposition of the ground, $|c>$, and excited vibrational state $|b>$. Finally, we note that the probability amplitude B_j will go as $e^{-i(\vec{k}_1-\vec{k}_2)\vec{r}_j}$ after preparation with the pump and Stokes fields, and introduce the notation $B_j = b_j e^{-i(\vec{k}_1-\vec{k}_2)\vec{r}_j}$, $C_j = c_j$. In view of the preceding, we find

$$
\begin{aligned}
<\hat{n}_4> &= \sum_{j,l} \bar{n}_3 \frac{(G_{43}/\hbar)^2}{|\Delta\omega_{43}|^2} e^{-i(\vec{k}_4-\vec{k}_3)\cdot(\vec{r}_j-\vec{r}_l)} \times <\phi_l|(|b><c|)_l(|c><b|)_j|\phi_j> = \\
&= \bar{n}_3 \frac{(G_{43}/\hbar)^2}{|\Delta\omega_{43}|^2} \left\{ \sum_l \rho_{bb}^l + \sum_{l\neq j} e^{i(\vec{k}_4+\vec{k}_2-\vec{k}_3-\vec{k}_1)\cdot(\vec{r}_l-\vec{r}_j)} \times \rho_{cb}^l \rho_{bc}^j \right\},
\end{aligned}
\tag{D.6}
$$

where $\rho_{bc}^j = b_j c_j^*$ and $\bar{n}_3 = \alpha_3^* \alpha_3$.

In the limit of a sufficiently large number of molecules in volume V

$$
\sum_{l\neq j} e^{i(\vec{k}_4+\vec{k}_2-\vec{k}_3-\vec{k}_1)\cdot(\vec{r}_l-\vec{r}_j)} = \frac{N(N-1)}{V} \delta(\vec{k}_4 - \vec{\kappa}), \tag{D.7}
$$

where $\vec{\kappa} \equiv \vec{k}_1 - \vec{k}_2 + \vec{k}_3$. Now, the three-dimensional Delta-function $\delta(\vec{k})$ can be written as

$$
\delta(\vec{k}_4 - \vec{\kappa}) = \delta(|\vec{k}_4| - |\vec{\kappa}|) \frac{\delta(\Omega_{\vec{k}4} - \Omega_{\vec{\kappa}})}{k_4^2}. \tag{D.8}
$$

Here $\Omega_{\vec{k}4}$ and $\Omega_{\vec{\kappa}}$ are the ''solid angle'' unit vectors pointing in $\vec{k}_4$ and $\vec{\kappa}$ directions, respectively. Assuming all molecules are in the same state so that $\rho_{bc}^j = \rho_{bc}$ etc., and that $\vec{k}_4$ corresponds to the phase-matched conditions, we have the ratio of the number of photons generated through coherent anti-Stokes (or Stokes) scattering to the number of spontaneously scattered (Stokes) Raman photons, equal to

$$
\frac{<n_4^{coh}>}{<n^{incoh}>} \cong \lambda_3^2 \frac{N}{V} \frac{|\rho_{bc}|^2}{\rho_{cc}} R. \tag{D.9}
$$

where we have used the fact that

$$
\delta(|\vec{k}_4| - |\vec{\kappa}|) \approx \int_{-R}^{R} e^{i(|\vec{k}_4|-|\vec{\kappa}|)r'} dr' \xrightarrow[k_4=\kappa]{} 2R \tag{D.10}
$$

in the phase-matched condition; R is the sample radius; the spontaneous Raman signal is integrated over all directions. The coherence ρ_{bc} is produced by the preparation laser pulses and quantifies the extent to which all molecules of the sample are made to oscillate in unison (in the coherent Raman scattering scheme). The numerical aperture of the collection optics (for the spherically emitted spontaneous Raman photons) will enter the denominator of Eq. D.9.

Eq. D.9 provides an intuitive means for comparing the efficiencies of coherent versus incoherent processes. Its physical interpretation is very clear: at maximal coherence ($\rho_{bc} = 1/2$) the ratio of those efficiencies roughly equals to the total number of molecules (counted through the sample thickness) per λ_3^2 area (where λ_3 is the wavelength of the probe field). This is because fields produced by coherent emitters add up in amplitude, such that the intensity grows as the number of coherent emitters squared, while the intensity of incoherent emission is simply proportional to the number of emitters.

VITA

Name: Dmitry Sergeyevich Pestov

Address: Physics Department, MS 4242,
Texas A&M University, College Station, TX 77843-4242

Email Address: dspestov@gmail.com

Education: Ph.D. in Physics, Texas A&M University, May 2008
M.S. in Physics (with honors), Nizhniy Novgorod State University, Russia, June 14, 2001
B.S. in Physics (with honors), Nizhniy Novgorod State University, Russia, June 25, 1999

Publications (2005-present):

- **D. Pestov,** G. O. Ariunbold, X. Wang, R. K. Murawski, V. A. Sautenkov, A. V. Sokolov, and M. O. Scully, *Optics Letters* **32** (2007), pp. 1725-1727. [selected for the August 2007 issue of ***Virt. J. Ultrafast Science***]
- M. Zhi, **D. Pestov**, X. Wang, R. K. Murawski, Y. V. Rostovtsev, Z.-E. Sariaynni, V. A. Sautenkov, N. G. Kalugin, and A. V. Sokolov, *J. Opt. Soc. Am. B* **24** (2007), pp. 1181-1186. [selected for May 1, 2007 issue of ***Virt. J. Biological Physics Research***]
- **D. Pestov**, R. K. Murawski, G. O. Ariunbold, X. Wang, M. Zhi, A. V. Sokolov, V. A. Sautenkov, Y. V. Rostovtsev, A. Dogariu, Y. Huang, and M. O. Scully, *SCIENCE* **316** (2007), pp. 265-268. [highlighted in ***Photonics Spectra***, p. 22 (June 2007)]
- Y. Huang, A. Dogariu, Y. Avitzour, R. K. Murawski, **D. Pestov**, M. Zhi, A.V. Sokolov, and M. O. Scully, *J. Applied Physics* **100** (2006), 124912.
- **D. Pestov**, M. Zhi, Z.-E. Sariyanni, N. G. Kalugin, A. Kolomenski, R. Murawski, Y. V. Rostovtsev, V. A. Sautenkov, A. V. Sokolov, and M. O. Scully, *J. Raman Spectroscopy* **37** (2006), pp. 392-396.
- **D. Pestov**, M. Zhi, Z.-E. Sariyanni, N. G. Kalugin, A. A. Kolomenskii, R. Murawski, G. G. Paulus, V. A. Sautenkov, H. Schuessler, A. V. Sokolov, G. R. Welch, Y. V. Rostovtsev, T. Siebert, D. A. Akimov, S. Graefe, W. Kiefer, and M. O. Scully, *Proc. Natl. Acad. Sci. U.S.A.* **102**, n. 42 (2005), pp. 14976-14981.

Professional Achievements/Honors/Affiliations:

- 20 presentations at professional conferences and seminars over the period 2005-2007
- Student Presentation Award (Fall TSAPS meeting, 2007)
- 2007 Robert Hyer Award of the Texas Section of the American Physical Society
- FiO Student Presentation Award (OSA's Frontiers in Optics, 2007)
- Incubic/Milton Chang Travel Award (OSA's Frontiers in Optics, 2007)
- TAMU Student Research Competition Awards
  2007 (1-st prize), 2006 (1-st prize), 2005 (2-nd prize)
- Affiliated with OSA, APS, Sigma Xi Research Society